Revealing Electronic Coupling in Semiconductor Quantum Dot Networks by Electrochemistry

Dissertation

der Mathematisch-Naturwissenschaftlichen Fakultät

der Eberhard Karls Universität Tübingen

zur Erlangung des Grades eines

Doktors der Naturwissenschaften

(Dr. rer. nat.)

vorgelegt von

Dipl.-Ing. (FH) Michelle Weber

aus Rüdesheim am Rhein

Tübingen

2018

Gedruckt mit Genehmigung der Mathematisch-Naturwissenschaftlichen Fakultät der Eberhard Karls Universität Tübingen.

Tag der mündlichen Qualifikation:	08.02.2019
Dekan:	Prof. Dr. Wolfgang Rosenstiel
1. Berichterstatter:	Dr. Marcus Scheele
2. Berichterstatter:	Prof. Dr. Thomas Chassé

1 Content

1 Content

2 Acronyms

Acronym	Description
(N)IR	(near) infra-red
AC	alternating current
BA	n-butylamine
CA	chronoamperometry
CASSCF	complete active space self-consistent field
CB	conduction band
CE	counter electrode
COIN	coupled organic inorganic nanostructures
CoPc	cobalt-4,4‘,4‘‘,4‘‘‘-tetraaminophthalocyanine
CuHFP	copper hexafluorophosphate
CuPc	copper-4,4‘,4‘‘,4‘‘‘-tetraaminophthalocyanine
CV	cyclovoltammetry
DC	direct current
DMF	N,N-dimethylformamide
DMSO	dimethylsulfoxide
DOS	density of states
DPV	differential pulse voltammetry
ECG	electrochemical gating
EMAS	(electrochemical) potential modulated absorption spectroscopy
FePc	iron-4,4‘,4‘‘,4‘‘‘-tetraaminophthalocyanine
FET	field effect transistor
FTIR	fourier transform infrared (spectroscopy)
FTO	fluorine doped tin oxide
GC	glassy carbon
H2Pc	4,4‘,4‘‘,4‘‘‘-tetraaminophthalocyanine
HDA	n-hexadecylamine
HOMO	highest occupied molecular orbital
IDE	interdigitated electrode
ITO	indium tin oxide
LED	light emitting diode
LIA	lock-in amplifier
LSPR	localized surface plasmon resonance
LUMO	lowest unoccupied molecular orbital
MeCN	acetonitrile
MeOH	methanol
MePc	metal-4,4‘,4‘‘,4‘‘‘-tetraaminophthalocyanine
MO	molecular orbital
MPTMS	(3-mercaptopropyl)-trimethoxysilane
NHE	normal hydrogen electrode
NiPc	nickel-4,4‘,4‘‘,4‘‘‘-tetraaminophthalocyanine
NMF	N-methylformamide
OA	oleic acid
OCP	open circuit potential
ODE	1-octadecene
ODPA	n-octadecylphosphonic acid
OLA	(Z)-octadec-9-enylamine
PSD	phase sensitive detector

2 Acronyms

QD	quantum dot
QTH	quartz tungsten halogen
RE	reference electrode
RMS	root mean square
SCE	saturated calomel electrode
SE	spectroelectrochemistry
SEM	scanning electron microscopy
SHE	standard hydrogen electrode
T3DSAc	5,5‘‘-dithiol-[2,2‘:5,2‘‘-terthiophene]-1,3-diyl-diethanethiolate
T3DSH	5,5‘‘-dithiol-[2,2‘:5,2‘‘-terthiophene]
TBAHFP	tetrabutylammonium hexafluorophosphate
TCE	tetrachloroethylene
THF	tetrahydrofurane
TOP	trioctylamine
TOPO	trioctylphosphine oxide
TOPSe	trioctylamine selenium
UPS	ultraviolet photoelectron spectroscopy
UV	ultraviolet
Vac	vacuum
VB	valence band
Vis	visible
WE	working electrode
XAS	x-ray absorption spectroscopy
XPS	x-ray photoelectron spectroscopy
ZnPc	zink-4,4‘,4‘‘,4‘‘‘-tetraaminophthalocyanine

3 Symbols

Symbol	Description	Unit
E_g	band gap energy of a QD	eV
$E_{g,el}$	electronic transport band gap energy	eV
$E_{g,opt}$	optical band gap energy	eV
E_c	confinement energy	eV
$\hbar$	reduced Planck constant	Js
π	pi	
m_e	electron mass	kg
m_h	hole mass	kg
r	radius of a QD	m
d	diameter of a QD	m
m_{eh}	reduced electron-hole mass	kg
$E_{g,0}$	band gap energy of the bulk semiconductor material	eV
E_{eh}	Coulomb correction term	eV
ε_r^∞	relative permittivity at high frequency	
ε_0	permittivity of the vacuum	
E_f	Fermi energy	eV
μ	1.) chemical potential, 2.) charge carrier mobility	1.) V 2.) m^2/Vs
k_B	Boltzmann constant	m^2kg/Ks^2
T	absolute temperature	K
e	elemental charge	C
Δx	special extension of the potential barrier	m
ΔE	height of the potential barrier	eV
Fc/Fc^+	ferrocene/ferrocenium couple	V
R_s	solution resistance	Ω
R_u	uncompensated resistance	Ω
U	voltage	V
E	electrochemical potential	V
i	current	A
i_p	peak current	A
A	area	m^2
c	concentration	mol/L
n	number of transferred electrons	
D	diffusion coefficient	m^2/s
υ	scanning speed	V/s
R	1.) gas constant, 2.) RMS value, LIA output for U_{sig}	1.) m^2kg/s^2molK 2.) V
Γ_0'	surface coverage of electroactive species	
$E_{1/2}$	half-wave potential	V
ΔQ	differential charge (injected into the QD film during an ECG experiment)	As
E_e	potential of the source or drain electrode during an ECG experiment	V
Q	charge	As
G	conductance	S
i_{sd}	source drain current	A
U_{sd}	source drain voltage	V

3 Symbols

σ	conductivity	A/Vm
w	width of the gap between source and drain electrode	m
l	total length of w	m
h	hight of the QD film on the electrode	m
N	charge carrier concentration	
V	volume	m^3
E_{1Sh}	energy of the $1S_h$ level (VB edge)	eV
E_{1Se}	energy of the $1S_e$ level (CB edge)	eV
E_{DC_ref}	unmodulated (electrochemical) potential that is set by a potentiostat in an EMAS experiment	V
U_{ref}	amplitude of the potential modulated reference signal in an EMAS experiment	V
Θ_{ref}	phase of the potential modulated reference signal in an EMAS experiment	°
ω_{ref}	frequency of the potential modulated reference signal in an EMAS experiment	Hz
E_{DC_sig}	DC output of an EMAS experiment. Contains information about the sensitivity of the instrument at a given wavelength.	V
U_{sig}	amplitude of the potential modulated detected signal in an EMAS experiment	V
Θ_{sig}	phase of the potential modulated detected signal in an EMAS experiment	°
ω_{sig}	frequency of the potential modulated detected signal in an EMAS experiment	Hz
V_{PP}	peak to peak amplitude of EMAS signal output	V
λ	wavelength	m
OD_{400}	optical density at 400 nm wavelength	
$V_{PP,start}$	peak to peak amplitude at the start of an EMAS experiment	V
$V_{PP,end}$	peak to peak amplitude at the end of an EMAS experiment	V
E_0	inflection point of the Fermi-Dirac fit for EMAS data, potential at which 50 % of the absorption is changed	V
E_0'	formal potential of the electrode	V
D_R	diffusion coefficient of the reduced species	m^2/s
D_O	diffusion coefficient of the oxidized species	m^2/s

4 Summary

4.1 Summary in English

A variety of coupled organic inorganic nanostructure (COIN) systems is investigated by electrochemistry. Specifically, two relatively new and niche electrochemical applications are implemented and their potential in probing the quantum dot (QD) frontier orbitals and electronic coupling can be shown.

Potential modulated absorption spectroscopy (EMAS) is an ideal method to probe the energetic level of the conduction band of semiconductor QDs. In this work, it is used to learn more about the formation of hybrid orbitals between CdSe QDs and metal phthalocyanines.

Electrochemical gating (ECG) is a very powerful technique when it comes to pinpointing the energetic level over which the majority of charge carrier transport happens in a COIN film. This is shown successfully on a variety of COIN systems like PbS QDs interlinked with terthiophene derivatives and CuS interlinked with amino-substituted Cu-phthalocyanine.

4.2 Zusammenfassung in Deutsch

Eine Auswahl an gekoppelten hybriden Nanostrukturen (COIN) wurde elektrochemisch untersucht. Dabei wurden zwei spezialisierte Methoden implementiert und ihr Potential für die Bestimmung der Grenzorbitale und der elektronischen Kopplung von Quantenpunkten aufgezeigt.

Potentialmodulierte Absorptionsspektroskopie (EMAS) ist eine ideale Methode, um die energetische Lage des Leitungsbandes von Halbleiter-Quantenpunkten aufzuklären. In dieser Arbeit wurde sie verwendet um mehr über die Bildung von Hybridorbitalen zwischen CdSe Quantenpunkten und Metall-Phthalocyaninen zu lernen.

Elektrochemisches Gating (ECG) ist eine sehr gute Methode um genau das Energielevel aufzeigen zu können, über das der Großteil des Ladungsträger-Transports in COINs stattfindet. Dies konnte erfolgreich an einer Auswahl an COIN-Systemen gezeigt werden, zum Beispiel an mit Terthiophen-Derivaten verlinkten PbS Quantenpunkten und an Amino-substituierten Kupfer-Phthalocyaninen.

5 Introduction and Motivation

Quantum dots (QDs) are first mentioned in the early 1980ies[1-3] and much progress has been made in the following 30 years to characterize them and refine their synthesis.

Synthetic approaches go away from epitaxial growth on surfaces and top down methods towards bottom up and hot injection methods[4, 5] that yield QDs with a narrow size distribution[6] and less surface trap states[7].

Considerable progress is also made to understand the electronic structure and excited electronic states of QDs compared to the bulk material of the same composition[8, 9]. The discovery that electronic structure can be considerably changed by varying the dimensions of a nanomaterial[2, 3] opens the interesting opportunity to engineer the electronic structure of a material without changing its chemical composition[10].

With the world's energy consumption rising and fossil energy sources dwindling, the need for renewable energy sources becomes more evident every year[10-12]. Besides wind and water energy, solar energy is one of the key solutions to harvest energy. This is done already today with silicon solar cells. These cells have the advantage of a relatively high efficiency of 21-25 %[13], but have a high production and installation cost[14, 15]. This could be changed with the use of new solar cells based on QDs[16].

Solar cells using QDs can absorb a broader range of sunlight due to their tunable absorption properties[16]. QDs can also be incorporated into transparent composite materials where they absorb a part of the sunlight, re-emit it in the near infrared range and channel it to solar cells on the edges of these so-called luminescent solar concentrators[17-20]. In the future, this technology might enable the use of every window for active energy generation. QDs are also used in photochemical water splitting[21] (which uses solar energy to produce hydrogen gas that may be used in fuel cells) and CO_2 reduction[22] (which uses the harmful greenhouse gas CO_2 from the atmosphere to produce more synthetically interesting input materials like methanol). QDs are also considered for use in light emitting diodes (LEDs) as they have similar advantages as organic molecules in regard of their processability in thin profile, lightweight, flexible and large area devices that consume less energy than conventional screens[23]. Furthermore, applications like field effect transistors (FETs), lasers, catalysis, drug delivery and printed electronics[24-27] are a focus of research in the QD community[10].

The list of applications for QDs is long and shall not be exhaustively discussed here. It should however be mentioned that most of these applications rely on some key properties that are unique to QDs, such as the size tunable band edge positions. One of the key challenges for most QD applications is the transfer of charge carriers from particle to particle and finally to the electrodes connected to the QD film. There are several different approaches on how to overcome this obstacle. Some groups sinter QDs together to enhance conductance of the QDs film[28]. Some exchange the usually insulating ligand shell with shorter ligands or inorganic salts[29].

In this work, QD networks are formed by exchanging the insulating native ligands with organic semiconductor molecules forming so called coupled organic inorganic nanostructures (COIN)[30]. The semiconductor molecules possess a binding group that chemically anchors them to adjacent QDs as well as a delocalized pi-system that makes them conductive. The goal for designing such composite materials is to align the QD band edges with the highest occupied molecular orbital (HOMO) and the lowest unoccupied molecular orbital (LUMO) of the organic semiconductor which can possibly lead to very high conductances. The objective of this work is to first investigate the positions of the quantum confined energy levels of both the inorganic QDs as well as the organic semiconductors, link those materials and investigate the position of the QD frontier orbitals and the conductance of the composite.

6 Objectives

To overcome the limitations of today's QD applications, the conductance of QD films needs to be enhanced. This work focuses on achieving this by interlinking films of semiconductor QDs with organic semiconductor molecules.

Unlike the approach of improving film conductance by shortening the linker molecules and thus moving the QDs closer together, the use of organic semiconductor linkers is expected to create a coupling of the QD's electronic states with the organic semiconductor's electronic states and thus to enable a band like transport.

In order to guide the engineering of those films, information about the electronic states in QDs and organic linkers must be gathered first. In case of those levels being of similar energy, it is likely that the materials show electronic coupling.

In the past, information about electronic states in organic semiconductors and semiconductor QDs has often been gathered by surface sensitive techniques like x-ray photoelectron spectroscopy (XPS) or ultraviolet photoelectron spectroscopy (UPS). However, the relevance of values obtained by these methods has been questioned because the measurement conditions in ultra-high vacuum are far away from those encountered by optoelectronic devices in real applications. They are also likely to destroy the shell of organic capping ligands that surround QDs which plays an important role for the QD properties (as highlighted in **Chapter 7.2**).

Electrochemistry can be conducted under ambient conditions and is well suited to uncover the potentials at which a material accommodates or releases electrons, thus giving away the energy of electronic states in the material. Another benefit of electrochemistry is its surface sensitivity. As one of the defining features of QDs is their large surface-to-volume ratio, electrochemistry can be used to not only probe the electronic states, but also surface trap states that play a major role in charge transport processes.

The electrochemical techniques employed in this work are cyclovoltammetry (CV) as the most common electrochemical technique, but also differential pulse voltammetry (DPV), which, being a differential method, allows for a better signal to noise ratio compared to CV. Electrochemistry is combined with spectroscopy in spectroelectrochemistry (SE) and potential modulated absorption spectroscopy (EMAS) experiments to strengthen the evidence of an electrochemical signal really being associated with an electronic state from the band edge. Electrochemical gating (ECG) is used to determine the influence of the electrochemical potential on the conductance of the QD film. This technique can also reveal the energy of the electronic level, over which the majority charge carrier transport occurs, backing up the hypothesis that interlinking semiconductor QDs with organic semiconductors creates extended, electronically coupled states.

7 Theoretical Background

7.1 Electronic States of Semiconductor QDs

In solid state physics, the Fermi energy is defined as the energy of the highest occupied orbital of a material in its ground state[31]. It can be imagined as the energetic level up to which the material is "filled" with electrons like a glass being filled up with water (although this is a very simplified model as we will see later).

Unlike water in a glass, electrons can only occupy certain energetic states in a material, the orbitals. In a solid material, the orbitals of the single molecules often overlap to form energy bands. These can be described by the density of states (DOS) that specifies how many available states can be occupied by electrons with a given energy[31]. If an energy band is partially filled, electrons can still move around in it and the material is conductive. This class of materials is called a metal (**Figure 1a**).

If the Fermi level is located in between two bands and leaves one band completely filled and the other completely empty, the material is called a semiconductor (**Figure 1b**). A semiconductor is called p-type when the Fermi level is closer to the valence band (VB) (**Figure 1c**) and n-type when it is closer to the conduction band (CB) (**Figure 1d**).

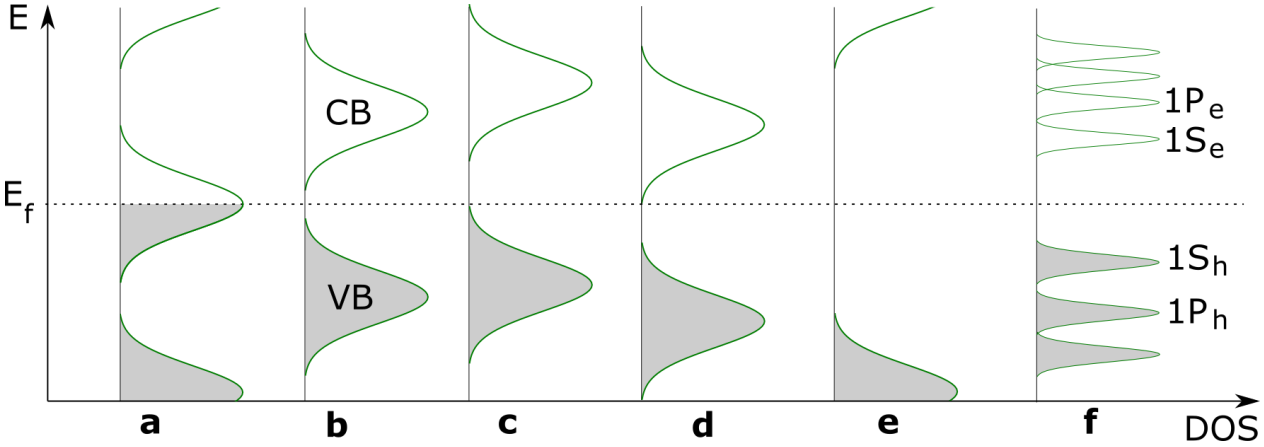

Figure 1: Schematic representation of the density of electronic states (DOS) in different types of materials. a) bulk metals, b) bulk intrinsic semiconductors, c) bulk p-type semiconductors, d) bulk n-type semiconductors, e) bulk isolators, f) nanoparticulate semiconductors.

The energy gap between the VB and CB is called the band gap (E_g). The difference between semiconductors and isolators (**Figure 1e**) is simply the magnitude of the band gap, however there is no clear definition on which magnitude of the band gap makes a material a semiconductor or an isolator.

Upon shrinking the size of the semiconductor particle, there is a point when its properties change from those of the above described bulk semiconductors to those of nanoparticulate semiconductors (**Figure 1f**). This point is reached when one or more of

the spatial dimensions of the particle becomes smaller than the exciton Bohr radius[9, 32-35] which is an intrinsic property of the material. Making particles smaller than the exciton Bohr radius and therefore confining the wave functions of the holes and electrons to a smaller space than they would usually occupy, introduces the confinement energy (E_c)[2].

$$E_c = \frac{\hbar^2 \pi^2}{2 m_e r^2} + \frac{\hbar^2 \pi^2}{2 m_h r^2} \quad (1)$$

The two summands in the equation are the ground state energy of the electron and hole with m_e and m_h as the masses of electron and hole and r as the radius of the QD. ħ is the reduced Planck constant.

From **Equation 1** it can be seen that the square of the QD radius (r) is inversely proportional to the confinement energy. The confinement energy increases as the particle size decreases, leading to larger band gaps for smaller QDs.

The electronic transport band gap of a semiconductor QD can therefore be described as:

$$E_{g,el} = E_{g,0} + E_c \quad (2)$$

With $E_{g,0}$ being the band gap of the bulk semiconductor material and $E_{g,el}$ the electronic transport bandgap of the nanoparticulate material[23, 36, 37].

The confinement energy does not only lead to a bigger band gap for smaller particles, but also to a quantization of the energy bands. **Equation 1** describes a classical particle in a box model and splits the energy of the VB and CB into a number of discrete energy levels. These discrete solutions of the quantum mechanical problem are often denoted by a natural number (0,1,2,…) and an uppercase letter (S,P,D,…)[38] (**Figure 1f**).

The lowest of the quantized CB levels is called the band edge electron level ($1S_e$, conduction band minimum or CB edge) and the highest of the VB levels is called the band edge hole level ($1S_h$, valence band maximum or VB edge)[23]. They can also be described as the QD frontier orbitals.

When an electron gets excited from a state in the VB to a state in the CB, a distinct amount of energy is needed. This energy can be translated to a photon of a certain wavelength. The primary method used to characterize the band gap is therefore UV-Vis or IR spectroscopy. However, the band gap observed this way is not exactly the band gap of the ground state QD.

The excitation of an electron to the CB creates an electron-hole pair, the so-called exciton[39]. As the electron and hole are influenced by the coulombic attracting force of

opposite charges, their energy difference becomes smaller. That is the reason behind the optical band gap ($E_{g,opt}$) of semiconductor QDs always being smaller than the electronic transport band gap ($E_{g,el}$).

This energy can be described by the Coulomb correction term[2, 23, 32, 36, 40]:

$$E_{eh} = \frac{1.8e}{4\pi\varepsilon_r^{\infty}\varepsilon_0 r} \tag{3}$$

With e being the electron charge, ε_r^{∞} being the relative permittivity at high frequency, ε_0 the permittivity of the vacuum and r the radius of the spherical QD. The optical band gap can therefore be described as the electronic transport band gap minus the Coulomb correction term[33, 39, 41-44]:

$$E_{g,opt} = E_{g,el} - E_{eh} \tag{4}$$

Apart from the states in the VB and CB, there can also be states within the band gap. They are often referred to as trap states because in transport processes, an electron making its way from the cathode to the anode may settle in one of the lower lying states and not contribute to conductance anymore[45] (**Figure 2c**). Energy, for example in the form of light, is necessary to lift it out of that trap state and put it back into the CB. The same may happen with holes on their way from the anode to the cathode along the VB.

Shallow trap states with energies close to either the CB or VB can be distinguished from deep trap states with energies further away from the bands. While shallow trap states play a role in impairing charge carrier transport through repeatedly trapping and releasing charge carriers, deep traps facilitate charge carrier recombination by bringing them closer to the oppositely charged band(**Figure 2d**). This decreases the luminescence quantum yield and hampers the solar cell performance[29].

Trap states result mostly from impurities in the crystal, imperfect crystal lattices or dangling bonds on the surface of the QD which usually result from a lack of surface passivation by ligand molecules[29, 46, 47]. Therefore, it can also be distinguished between trap states in the “bulk” of the QD that originate from imperfect crystal lattices or surface states that result from dangling bonds[2].

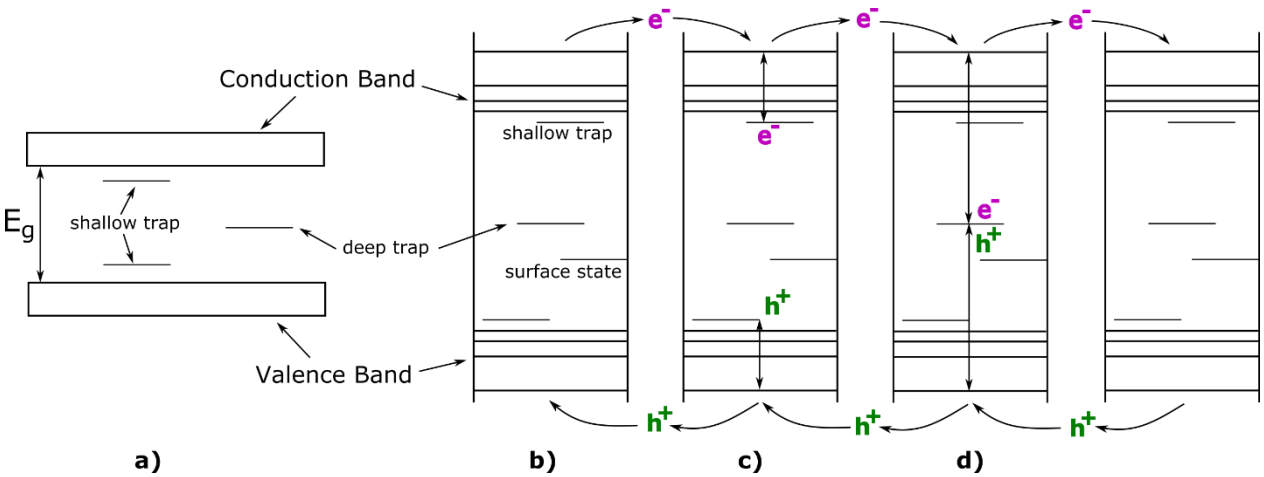

Figure 2: Different types of states within the band gap and their influence on charge carriers. a) Trap states in a bulk semiconductor, b) trap states in a nanoparticulate semiconductor, c) charge trapping in shallow trap states, d) charge recombination in deep trap states. (Modified from Ref[2])

7.2 The Influence of Ligands on QD Energy Levels

The ligand shell around QDs has many different functions. It prevents the QDs from agglomerating and precipitating during synthesis through steric or electrostatic stabilization of the colloid[23, 48]. It also helps control the reaction kinetics through favoring to bind to a specific crystal plane of the growing particle. This leads to a variety of shapes like disks, rods and stars[49, 50]. (In this work, only spherical nanoparticles and nanodiscs are used.)

However, ligands are not only useful during synthesis, but also help with the processing of QDs and extend their range of applications by using organic or inorganic ions[51, 52], polymers[53] or multivalent linker molecules as ligands[54-57]. Ligands can help eliminate trap states, as will be discussed later. By varying the dipole moment of the ligand, the quantum confined energy states of the QD can be shifted[58-60]. The passivation of the surface can also be used to protect the QDs against environmental influences. For example, treatment with tetrabutylammonium iodide[61] makes PbS QDs more stable against oxidation in air.

Varying the head group of the linker molecule leads to different binding strengths between the QD and its ligand shell. During synthesis, a ligand should bind to the QD only strong enough to prevent it from agglomerating and keeping it in solution. Using too strongly binding ligands may make subsequent ligand exchange difficult. For most applications, including the ones being discussed in this work, the native ligand shell should be replaced with strongly binding ligands. Through the use of multivalent linkers, large, mechanically stable QD networks can be formed.

The binding of the head group to the QD can also passivate trap states by forming hybrid orbitals with surface dangling bonds from the QD. This new bond may result in a new

bonding orbital below the VB edge and an antibonding orbital above the CB edge. This way, electrons from shallow trap states just above the VB edge move to the newly formed bonding orbital that is below the VB edge and shallow traps just below the CB edge become the newly formed antibonding orbital, which is above the CB edge and thus not as easily filled with electrons[29]. Care must be taken with some ligands, because they can also introduce new trap states[62, 63].

To achieve highly conducting films, not only the trapping of charges is an important issue to consider. Charge carriers must also get from one QD to the other as easily and fast as possible. This can be facilitated by a number of different approaches which will be discussed in the next chapter.

7.3 Electrical Conductance in Semiconductor QD Films

Before discussing electrical conductance, another clarification about the Fermi level needs to be added. Imagining it as the filling level like water in a glass (as described in the simplified analogy above) is only valid at absolute zero temperature. Above that, it is more suitably modelled by a Fermi-Dirac distribution instead of a discrete level. This distribution of charges leaves some states above the Fermi level filled and some below it empty.

The probability for a state with energy E_f being occupied is[31]:

$$f(E_f) = \frac{1}{e^{\frac{E_f - \mu}{k_B - T}} + 1} \tag{5}$$

With μ being the chemical potential, k_B the Boltzmann constant and T the absolute temperature.

When a material is a semiconductor with the Fermi level inside the band gap, the broadening of the Fermi level leads to the occupation of some states in the CB and/or some states in the VB to become unoccupied and conductance is possible (**Figure 3**).

This phenomenon is called intrinsic conductance and is the reason behind semiconductors becoming more conductive with increasing temperature[31].

Inserting atomic impurities with one valence electron more (or less) into a semiconductor matrix is called n- (or p-) type doping. As shown in **Figure 1c+d**, n-type doping moves the Fermi level closer to the CB, while p-type doping moves it closer to the VB. It is straightforward that in these materials, even a moderate broadening of the

Fermi level leads to a significant injection of charge carriers into the bands. Therefore, doped semiconductors are usually more conductive than undoped semiconductors.

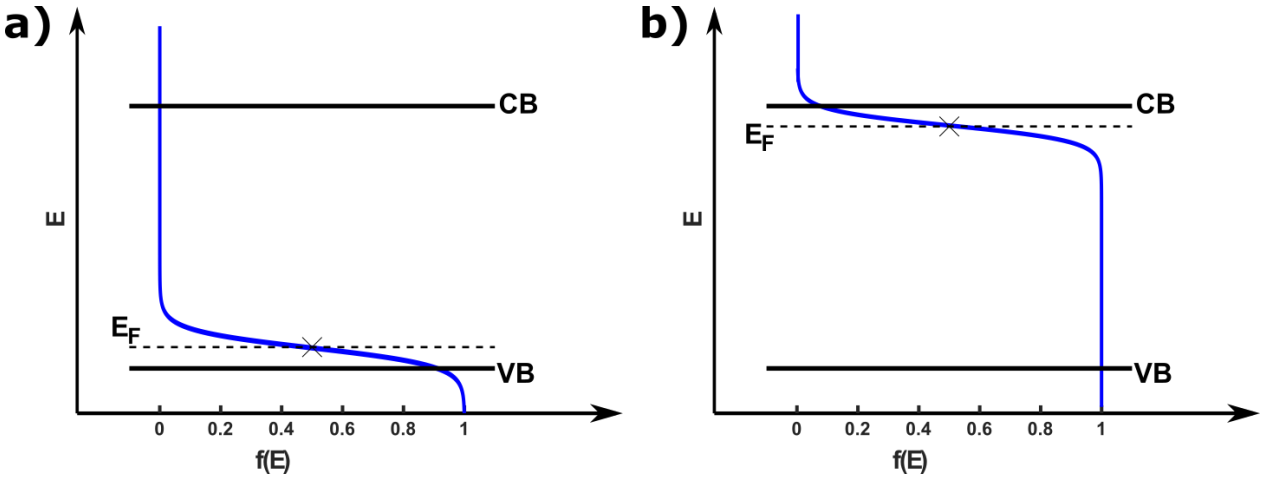

Figure 3: Model of the distribution of charges in a semiconductor material at room temperature. a) The Fermi level is close to the VB and b) close to the CB.

As opposed to bulk semiconductors, doping of semiconductor QDs can be tricky because the usually applied doping levels do not result in even one dopant per QD. For example, the typical ratio of doping silicon with boron impurities is 1:10^5[31]. A typical QD consists of a few thousand atoms[47]. That means under 10% of the QDs would actually have an impurity. It can also be synthetically challenging because the tiny crystals tend to undergo self-purification, excluding any foreign atoms from their crystal matrix[47].

Another challenge for the conductance in QD films is that a charge carrier can move relatively freely inside one QD but crossing to the next QD means to overcome a high potential barrier where the QD is separated from the next QD by a ligand shell. By changing the ligands, this barrier can be tuned.

Shorter ligands mean that the QDs move closer to one another, thereby reducing the spatial extension of the potential barrier[46, 64, 65] (Δx, **Figure 4b**).

Using ligands with different dielectric properties can reduce the height of the barrier[45] (ΔE, **Figure 4c**). Both strategies enable a better overlap of the exchange integrals of the charge carrier probability functions of adjacent QDs (green curves in **Figure 4**).

The probability function describes the probability of finding a charge carrier in a certain point in space. The more the probability functions of two adjacent charge carriers overlap, the greater is the probability of them being delocalized between the two QDs. This leads to a higher charge carrier mobility and conductance.

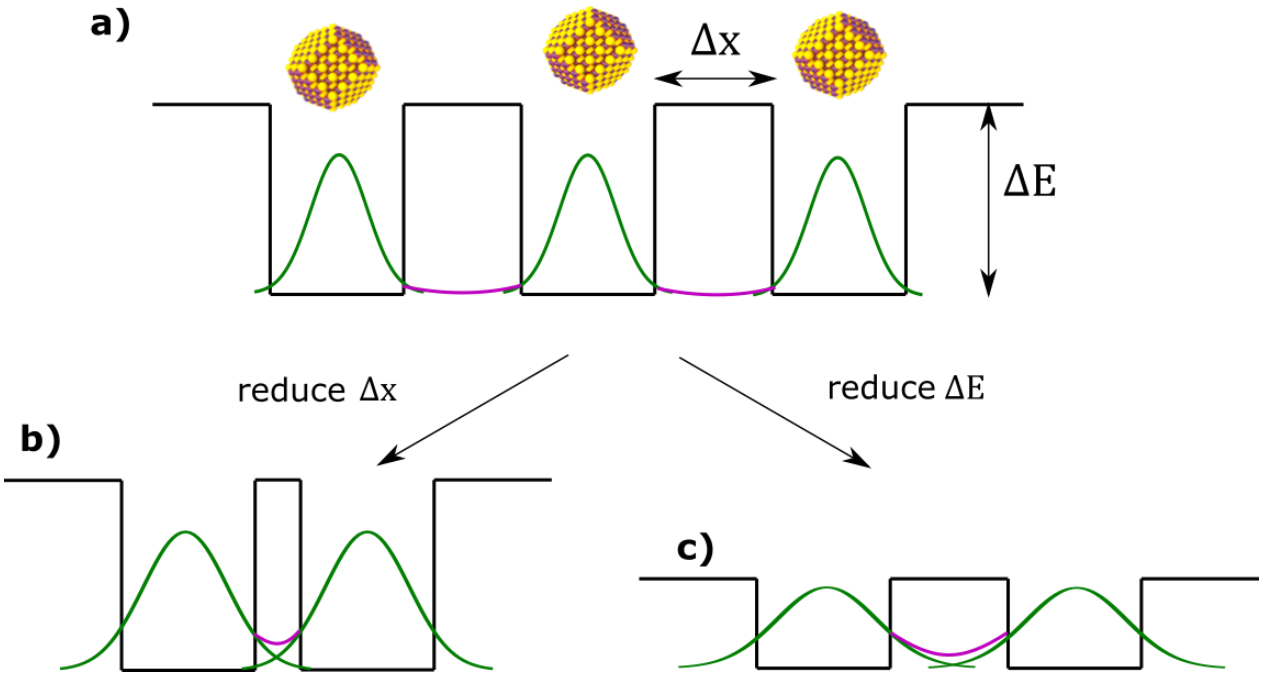

Figure 4: The influence of barrier width and height on charge carrier probability functions in QD networks.
a) Periodic lattice in a QD film with the charge carrier probability functions confined in the QDs and spaces with high potentials (e.g. insulating ligand shell) separating them. b) Effect of reducing the distance between QDs. c) Effect of reducing the energy barrier between QDs. (Modified from Ref[45])

Other factors for the conductive properties of a COIN film are the size distribution of the QDs and their distribution in the film. A narrow size distribution is favorable because the energies of the VB and CB edge are size dependent for QDs (see **Chapter 7.1**). Having an uneven size distribution causes electrons (holes) to get trapped in larger QDs because their CB (VB) energy is lower (higher).

Another possibility of enhancing film conductance is to bridge QDs with multidentate semiconducting organic molecules. These linkers usually have larger band gaps than the QDs, so in most cases either the HOMO aligns energetically with the VB edge or the LUMO with the CB edge[30]. As each linker is in contact with more than one QD and each QD is in contact with several linkers, the resonance between the HOMO (LUMO) of the linker and the VB (CB) edge of the QD leads to the formation of energy specific "minibands". Charge carriers are highly delocalized in these states which leads to very good conductance of the QD film[66]. This class of materials, where organic ligand molecules are not only used to increase the mechanical stability of the QD film, but actively take part in electronic transport processes is called COIN[30].

Another interesting property of COINs is that they allow to fabricate a hole conducting layer (**Figure 5**, left) and an electron conducting layer (**Figure 5**, right) from the same kind of QDs, but with different linker molecules. This is especially useful for the fabrication of solar cells or diodes. These require a spatial separation of hole and

electron transport layer to reduce undesired charge recombinations. Fabricating both layers from the same material can facilitate manufacturing of these devices.

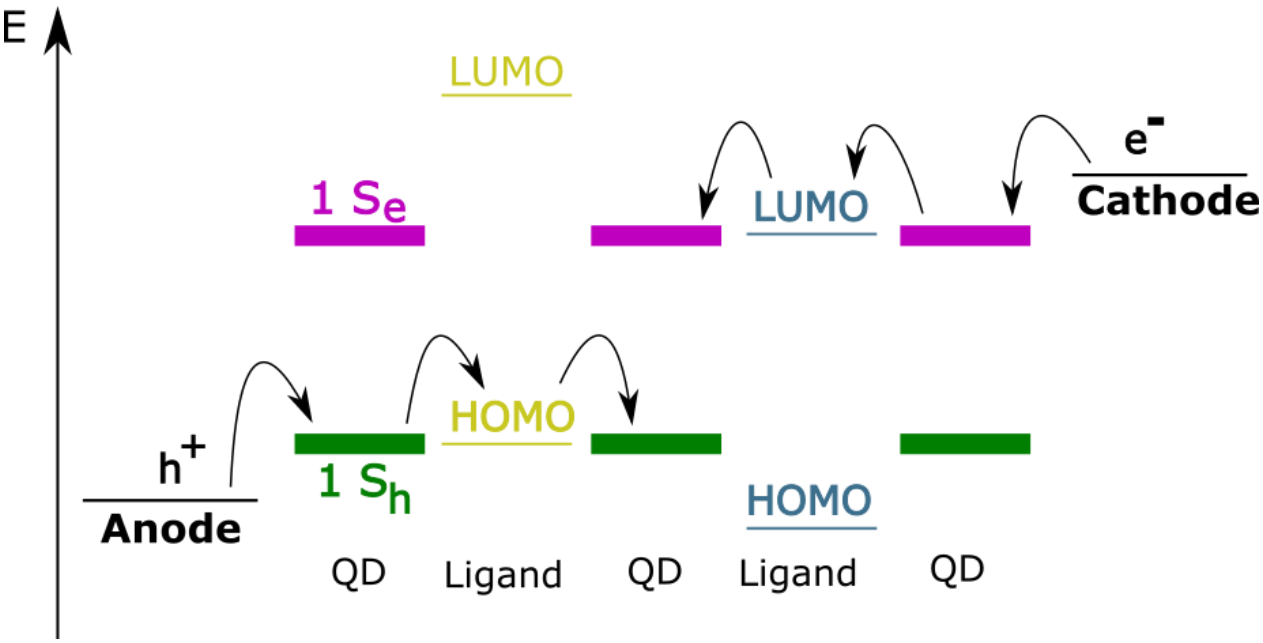

Figure 5: Sketch of the energy levels in a COIN with the same QD material, but different linker molecules. Alignment of the HOMO with the VB edge (left) leads to a hole conducting material. Alignment of the LUMO with the CB edge (right) leads to an electron conducting material.

To find good combinations of linkers and QDs, quantum chemical calculations can be used for an initial screening of suitable candidates. Physical measurements have to follow this step because it is not uncommon that theoretically the levels are very close to each other, but do not couple practically. This can be due to different orbital geometries in the QDs and linkers that do not interact.

The possibility to change the energy levels of QDs to a certain degree by synthesizing smaller or larger particles is also convenient when trying to design good COIN films. In case of a “fixed” energy level in the linker, the corresponding energy level of the QD is variable to a certain degree by varying its size and can be matched to the energy of a linker frontier orbital.

The fabrication of COINs often comes with some synthetical challenges. One way to exchange the ligands is to have both the linker and the QD in solution[29]. With multivalent linkers, this leads to a precipitation of the QDs. For some applications this might be favorable, but it does not yield a very uniform film.

Another strategy is to attach a film of QDs with their native ligands on a substrate and dip this into a concentrated linker solution. This method is prone to getting cracks in the film because the linkers are often shorter than the native ligands (which is also

favorable because it moves QDs closer together). A way to overcome this, is to apply a number of thin layers on top of each other rather than trying to form one thick layer[67].

To reach highly ordered monolayers of COIN films, the QDs are deposited on top of a non-solvent and the linkers are injected in that liquid. After the exchange reaction, the film is carefully lowered to the substrate[68]. This method requires finding a medium that the linkers are soluble in, but the QDs are not. It yields only very thin films which might not be suitable for optical studies. The film might get cracked when deposited on a substrate that is not very even (e.g. because electrical contacts of a few tens of nanometers height are placed on it).

In this work, the dipcoating method is used with 8-20 thin layers applied to a substrate. PbS, CdSe and $Cu_{1.1}S$ QDs are chosen to be investigated.

PbS QDs are a well-studied material for use in quantum dot sensitized solar cells[69, 70], so improving the conductivity of COIN films based on PbS could easily lead to improvements in these devices without changing much on their architecture.

CdSe QDs are extensively studied in the context of fluorescence, and find application in light emitting diodes[71]. Similar to solar cells, improving the transport of charges through the film reduces their residence time in the film and thus unwanted side reactions like radiationless decay or chemical reactions.

$Cu_{2-x}S$ is a particularly interesting material because of its low toxicity as compared to lead and cadmium. $Cu_{1.1}S$ QDs also show a localized surface plasmon resonance (LSPR) similar to the one observed for noble metal QDs[72-74]. The exact positions of the electronic states in $Cu_{2-x}S$ QDs have been discussed for some time. One of the problems finding a definitive answer is that $Cu_{2-x}S$ QDs come in a great variety of stoichiometries and crystal structures. The most common ones are the fully reduced form Cu_2S, the slightly oxidized forms $Cu_{1.94}S$, $Cu_{1.8}S$ and the fully oxidized form CuS[75, 76]. It is straightforward that the oxidation of the QDs removes electrons from the VB and therefore the band gap gets larger the more oxidized they get. The band gap of the fully reduced Cu_2S is reported with 1.2 eV, $Cu_{1.94}S$ with 1.23 eV[77], $Cu_{1.8}S$ with 1.5 eV and the fully oxidized form CuS with 2.0 eV[78].

In the following, it is assumed that the material used in this work is $Cu_{1.1}S$, which forms a stable metallic phase. Upon electrochemical oxidation and reduction, different phases are generated in situ.

7.4 Using Electrochemistry to Characterize QDs

Energy states of electrons can be measured by a number of different techniques. The most important of them are electrochemistry and photoelectron spectroscopy.

Traditionally, the location of the Fermi level in the neutral state as well as the CB and VB of semiconductors are investigated by methods like UPS, XPS (for the VB) and x-ray absorption spectroscopy (XAS, for the CB). These methods have a vast number of benefits like high precision, sensitivity and the potential to detect the oxidation number of atoms, but also some disadvantages that electrochemistry does not have.

Ultraviolet and X-ray radiation is high in energy and might spoil or destroy the ligand shell of the QDs[60, 79]. The QD film might also get electrically charged during the experiment, influencing the results. The methods are performed under ultra-high vacuum conditions (ca. 10^{-9} Torr [80]) which are quite different from the ambient conditions that future applications of QD films like solar cells and LEDs will experience. Thus, results measured with these techniques have to be compared to data obtained under ambient conditions (e.g. from electrochemical experiments) to make sure they are applicable.

Many of the future applications of QDs, like dye-sensitized solar cells, require the use of an electrolyte. Since the chemical environment has a major influence on the position of the band edges, it makes sense to measure their position when the QDs are surrounded by an electrolyte[81-84].

Electrochemistry is a very sensitive method, suitable to measure very small amounts of material. However, given the low solubility of QDs in the common solvents used for electrochemistry, it is not always easy to detect a signal. A way to improve the signal intensity is to attach the QDs to the electrode surface[85]. This is used in this work, also keeping in mind that not only QDs with their native ligands are investigated, but also networks of QDs which are fabricated on a solid surface.

When used on solid analytes, electrochemistry predominantly probes their surface, which is favorable in the case of QDs because of their large surface to volume ratio. For the same reason, electrochemistry is also likely to detect changes introduced by the application of different linkers to the QDs. Electrochemistry can detect electronic states of the QD material as well as trap states. It can be used to assess the quality of QDs because quite often less trap states mean better quality[9].

With its surface sensitivity, electrochemistry complements well the information obtained by spectroscopic techniques like Fourier transform infrared spectroscopy (FTIR) or absorption spectroscopy because these techniques probe the bulk of the material[86]. Properties of the QD materials can thereby be attributed either to their surface or the interior. Spectroscopy may help distinguish electronic states from surface traps which look very similar in electrochemical experiments but quite different in absorption spectroscopy[85, 87].

Care has to be taken when characterizing QD films electrochemically because the process of immobilizing them on the electrode surface might already alter their properties, e.g. when the electrode is functionalized with a silylation agent like (3-mercaptopropyl)-trimethoxysilane (MPTMS) that attaches the QDs to the electrode surface through mercaptopropyl units (see **Chapter 10.2.2**). If the intended ligand of the QDs is not thiol-based, that might already influence the electronic structure of the bottom-most layer of QDs.

It might also happen that the electron transfer from the electrode causes a chemical reaction that alters the chemical nature and the morphology of the QD film and quite often leads to a detachment of the film from the electrode[85]. The properties of QDs in a film might also be different from those of single or dissolved QDs because the dense packing leads to the particles influencing each other.

Care must also be taken when comparing electrochemical results obtained with different solvents, electrolytes or electrodes[60, 88]. Even though the reference electrode is calibrated against a common standard like the ferrocene/ferrocenium couple, differences due to solvation of the analyte molecule or the calibration standard can be observed[89].

Results obtained from electrodes modified with QD films follow different kinetics than results obtained from dissolved analytes in solution. The special considerations that have to be taken into account when working with QD films are discussed in more detail in **Chapter 8.1.2**.

8 Used Methods and Instrumentation

8.1 General Concepts of Electrochemistry

8.1.1 Functional Principle of a Potentiostat and Bipotentiostat

The most basic electrochemical cell is made of two electrodes immersed into an electrolyte solution. On each of these electrodes a half-reaction takes place that responds to the potential difference at the surface of the corresponding electrode[90, 91].

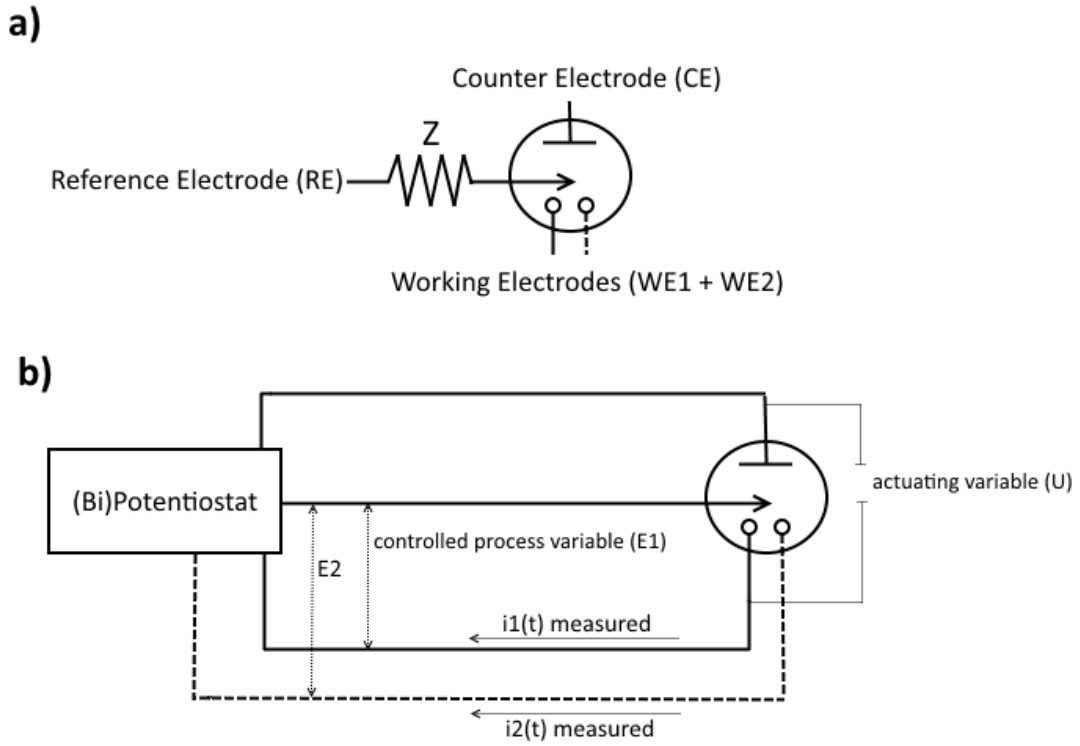

Figure 6: Functional principle of a (bi-) potentiostat and a basic electrochemical cell.
a) Close up of the electrochemical cell with the counter electrode, working electrode(s) and the reference electrode which is kept current-free by a large impedance resistor. b) Control and measurement cycles of a (bi-)potentiostat. (Modified from Ref[90])

As only one of the two half-reactions is of interest in most cases, a standardization of one electrode is necessary. The internationally accepted primary reference is the standard hydrogen electrode (SHE) or normal hydrogen electrode (NHE). Another common reference, the saturated calomel electrode (SCE) has a potential of 0.242 V vs. NHE. The also commonly used silver/silver chloride electrode has a potential of 0.197 V vs. NHE[90]. The NHE itself has a potential of -4.6 eV vs. the absolute vacuum scale (vs. Vac)[90, 92]. These values should however be treated with caution and serve as an estimate rather than a solid source of truth because they are still a matter of scientific debate.

All these reference electrodes (RE) require aqueous conditions. If a measurement is taken in non-aqueous solvents, one needs to use a pseudo reference like an Ag wire that is calibrated against a reference standard like the ferrocene/ferrocenium couple (Fc/Fc^+) from which the potential in respect to other known reference systems is evaluated. The absolute position of Fc/Fc^+ on the absolute vacuum scale (vs. Vac) is dependent on the solvent and still subject of scientific debate[89, 93]. The absolute energy values of the redox potentials in this work are calculated by assuming Fc/Fc^+ to be located at 4.8 eV below vacuum level, according to the work of Pommerehne et. al.[92]. As all of the experiments here are carried out in non-aqueous solvents, all the REs are in fact pseudo REs, but will be referred to as RE for the sake of shortness.

Ideally, the RE has a fixed potential and does not take part in current flow. No charge carriers are ideally exchanged between the RE and the solution. In reality this is approximated by connecting the RE to a high impedance resistor (**Figure 6a**)[90]. This way, the potential of one of the two electrodes of the system is fixed and all remaining potential changes can be attributed to the other electrode, the so-called working electrode (WE).

The WE is usually made of a highly conductive material that does not interfere in the electrochemical reaction like platinum or glassy carbon (GC)[90]. In this work, also fluorine doped tin oxide (FTO) is used where a transparent WE is necessary.

A setup with two WEs is called a bipotentiostat. It requires some elaborate circuitry[90] that ensures that the potential of one WE does not influence the potential of the other.

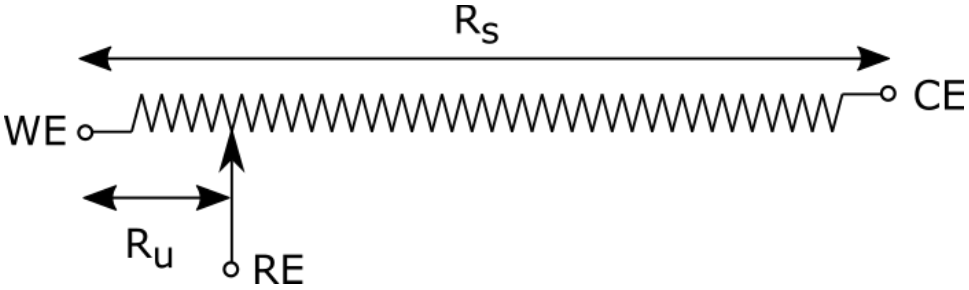

Figure 7: Schematic representation of resistances in an electrochemical cell:
Solution resistance between the working and counter electrode (R_s) and uncompensated resistance between the working and reference electrode (R_u). (Modified from Ref[90])

When the WE exchanges charge carriers with the electrolyte, they have to enter back into the electric circuit somewhere, but cannot do so with the RE (because no current can flow through the RE, see above). Therefore, a third electrode has to be introduced. This so-called counter electrode (CE) can be made of a convenient material as long as it is conductive and does not interact with the components of the experiment.

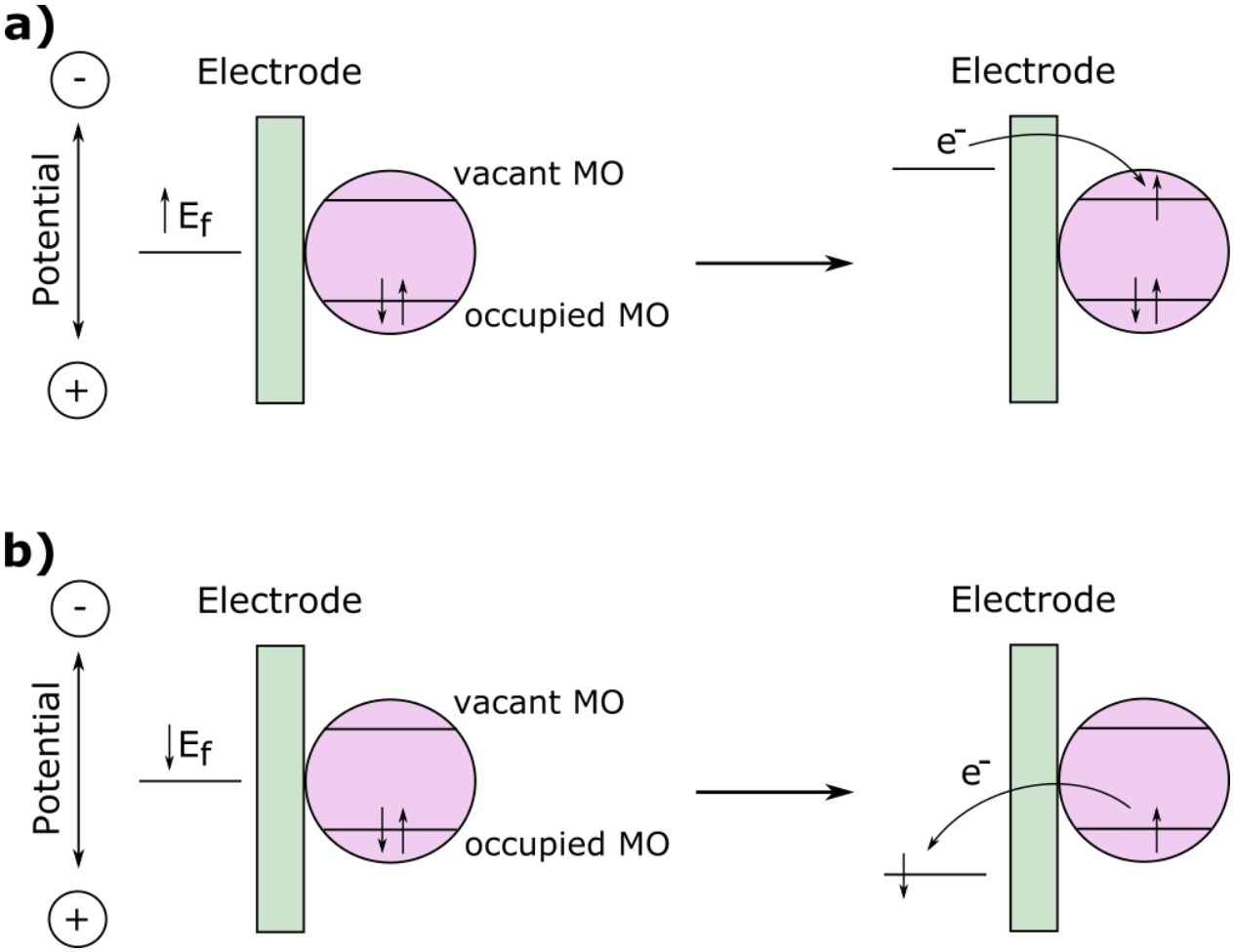

Figure 8: Sketch of the reduction and oxidation processes between the WE surface and an adsorbed analyte.
a) Electrochemical reduction: a negative potential is applied to the WE and an electron is injected into a vacant molecular orbital (MO) of the analyte. b) Electrochemical oxidation: a positive potential is applied to the WE and an electron is withdrawn from an occupied molecular orbital of the analyte.

To achieve the desired potential difference between RE and WE (controlled process variable, E, **Figure 6b**), the terminal voltage between WE and CE (actuating variable, U, **Figure 6b**) is varied until E reaches the desired value[90]. This can lead to much higher potentials for U than for E. The difference between U and E is called the overpotential (μ). The measured value for the potential E before applying any terminal voltage U is called the open circuit potential (OCP)[90].

The three electrodes are immersed into a liquid. An electrolyte salt gives a certain conductance to that liquid, but especially with the organic solvents employed in this work, the solution still retains a considerable resistance. This solution resistance (R_s) causes the potential between the WE and CE as well as the potential between WE and RE to drop (**Figure 7**). This can lead to a measurement error. In modern instrumentation, the uncompensated resistance (R_u) can therefore be automatically compensated with the instrument software. In all experiments in this work, a 80 % compensation at the OCP is executed with the compensation program of the CH Instruments software[94].

When the WE is polarized negatively with respect to the RE, the energy of electrons (which is equivalent to the Fermi energy, E_f) inside the WE is raised (**Figure 8a**). If this energy is higher than the energy levels of vacant MOs in the analyte, an electron is transferred and a reduction current flows. The analyte (A) becomes negatively charged (A^-). Vice versa, when the energy of electrons in the WE is lowered below the energy of occupied sites in the analyte (**Figure 8b**), an oxidation current flows. Here, the analyte (A) becomes positively charged (A^+)[90].

The energy that is needed to induce a reduction or oxidation current, corresponds to the standard potential E° of the redox couple A/A^- or A/A^+, respectively[90].

8.1.2 Electrochemistry on QD Films

In the most common electrochemical experiment, the analyte is dissolved in the electrolyte solution and all three electrodes are immersed in the electrolyte. Upon linearly increasing or decreasing the potential of the WE (as done so in CV measurements), a combination of electron transfer and diffusion processes occur. These processes are described extensively in the literature and will not be repeated here[90, 91].

In this case (case one, **Figure 9**), the resultant current (i) plotted vs. the set potential (E) shows a maximum for the oxidation current and the minimum for the reduction current occurring at slightly different potentials[91]. The standard potential of the reaction is the arithmetic mean of the current minimum and maximum. The current follows the Randles-Sevcik equation with i being proportional to the square root of the scanning speed ν (with units of [V/s]).

$$i_p = (2.69 \cdot 10^5) A c \sqrt{n^3 D \nu} \qquad (6)$$

In this equation, i_p stands for the peak current, A for the electrode area, c for the bulk concentration of the electroactive species, n for the number of transferred electrons and D for the diffusion coefficient of the electroactive species in the electrolyte[90].

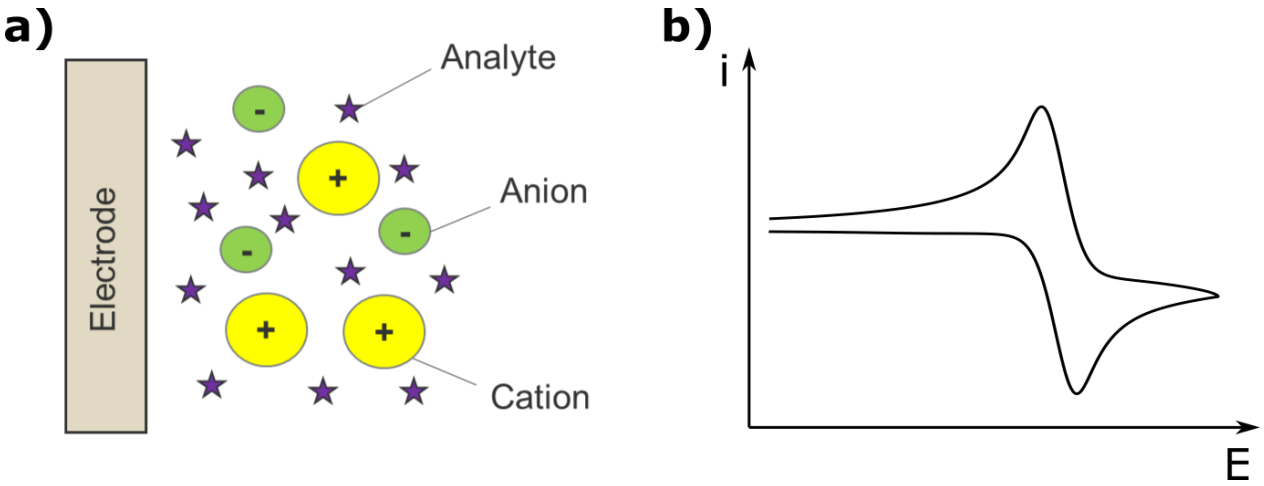

Figure 9: Case one: The analyte is dissolved in the electrolyte solution.
a) Electrochemistry with the analyte dissolved in the electrolyte. b) Characteristic cyclovoltammogram.

Another quite common case in electrochemistry (case two, **Figure 10**) is that of a chemically modified electrode. Here, the current is proportional to the scanning speed. The peak maxima occur at the same potential because no diffusion of analyte to and from the electrode has to be accounted for.

$$i_p = \frac{n^2F^2}{4RT}\nu A\Gamma_0' \tag{7}$$

In this equation, F is the Faraday constant, R the ideal gas constant, T the absolute temperature and Γ_0' the surface coverage of electroactive species[90].

However, for electrodes that carry QD films, both concepts quickly show their limitations. There should be no diffusion processes as in case one, but the peak maxima are observed to occur at different potentials unlike in case two[88].

In the work of Scholz et al.[95], initially published in 2005, the electrochemistry of small grains attached to the surface of electrodes is discussed (case three). A general theme in this book is the "three-phase junction" where I) the electrode, II) the electrolyte and III) the granular analyte meet. Electron injection from phase I (the electrode) to phase III (the analyte) is only possible when a positively charged cation from phase II (the electrolyte) also enters phase III. The kinetics of this scenario also require a diffusion constant as in case one, however here it is the diffusion of the electrolyte cation in the solid granular analyte instead of the diffusion of the dissolved analyte in the electrolyte solution.

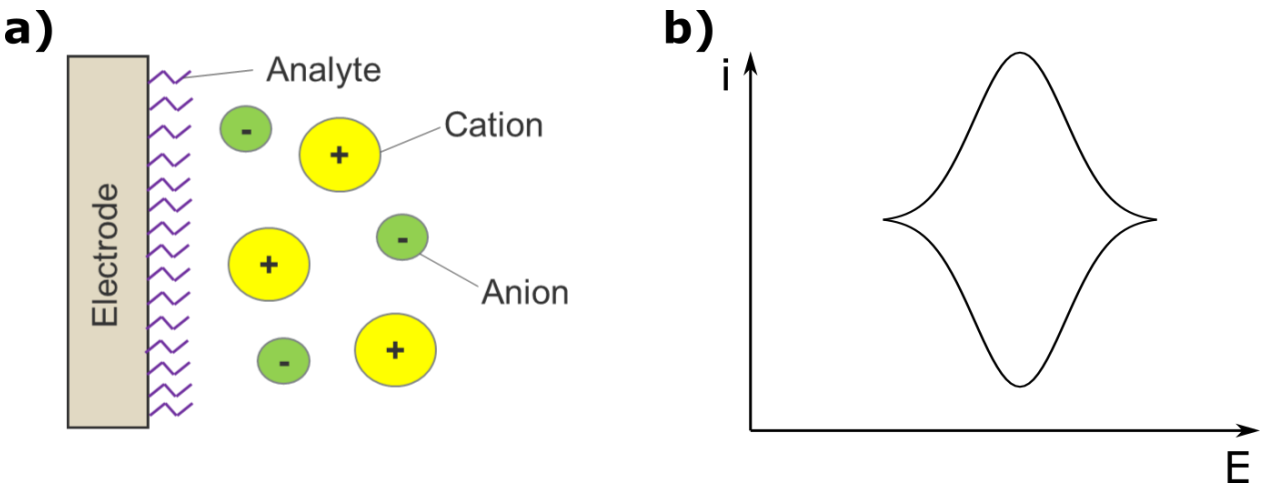

Figure 10: Case two: The analyte is attached to the surface of the electrode.
a) Electrochemistry on the chemically modified electrode. b) Characteristic cyclovoltammogram.

The models presented in this work, however do not really fit the observed shape of the CVs obtained for QD films[96]. This can be due to the author taking only reactions at the three phase junction into account and modeling any diffusion processes across the material as immediate. To the best of my knowledge, the kinetics of the propagation of cations in a matrix of particles have not been modeled for a CV experiment so far.

It is also not clear whether the cations actually enter the lattice of the single QD or compensate the QD's charges by being in their proximity. In both cases however, a diffusion process of some kind (either through the film or the QD) has to take place.

Van der Stam et al.[88] described three different scenarios of charge compensation in a QD film: a) the reversible intercalation of (very small) cations in the voids of the QD film, b) the capacitive charging of the QD film by rather large cations in the proximity of the film and c) the permanent intercalation of cations into the QDs. As c) is described as irreversible, it is not desired in electrochemical experiments. Capacitive charging (b) may cause problems for thicker films where only parts of the film might get charged. That leaves a) as the desired case.

Ideally, after full equilibration, an electron is injected into each QD and a cation diffuses into the film to compensate the charge by being in close proximity to the QD. The Fermi level of the QD itself is raised (**Figure 11a**).

To increase the likelihood of positive countercharges entering the QD film during the reduction experiment, the cation of the electrolyte salt needs to be sufficiently small to enter the voids between the QDs. Lithium salts have shown to be a better choice than tetrabutylammonium salts for this purpose[97], but not only the size of the counter ion plays a role. The nature of the ligands that surround the QD determine the size of the voids in the film and therefore the likelihood of cations entering the film. Here, generally, the longer and the more flexible the ligands are, the better the electrochemical measurement works[97] (**Figure 11b**). This might create a challenge, as in this work the

aim is to bring QDs closer together and to use (stiff) aromatic ligands to improve film conductance.

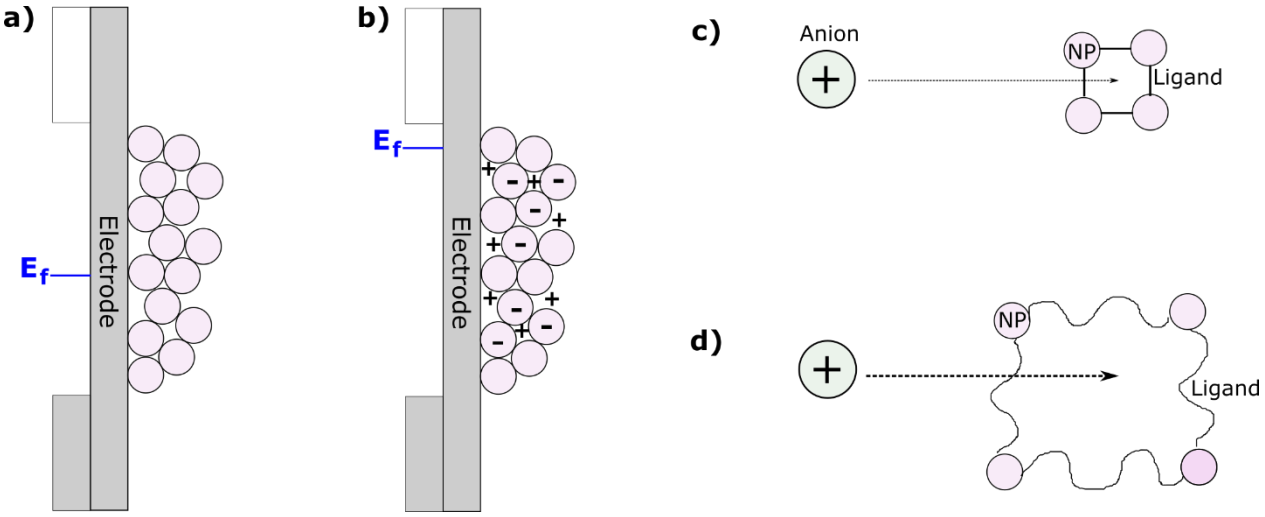

Figure 11: Schematic representation of charge injection into the voids of a QD film.
a) Neutral QD film on an electrode. b) QD film on an electrode after applying a reductive potential, the Fermi level is raised and positive countercharges diffuse into the voids of the film. c) Cations are less likely to enter the voids in a QD film with short stiff ligands than they are to d) enter the voids of a film with long flexible ligands.

8.2 Differential Pulse Voltammetry

A DPV experiment is carried out in a three electrode setup. The WE is kept at a constant potential first (Init. E), to which a potential pulse is applied. After the pulse, it reaches a third potential (Init. E + Incr. E) which is between the initial and the pulse potential (**Figure 12**).

The current is sampled before and at the end of the pulse. The two samples are each averaged and then subtracted from one another to yield the differential current. This current is plotted against the potential which can be described as:

$$E = Init.E + \sum_{k=1}^{k} k \cdot Incr.E \tag{8}$$

With k being the number of incremental potential steps measured.

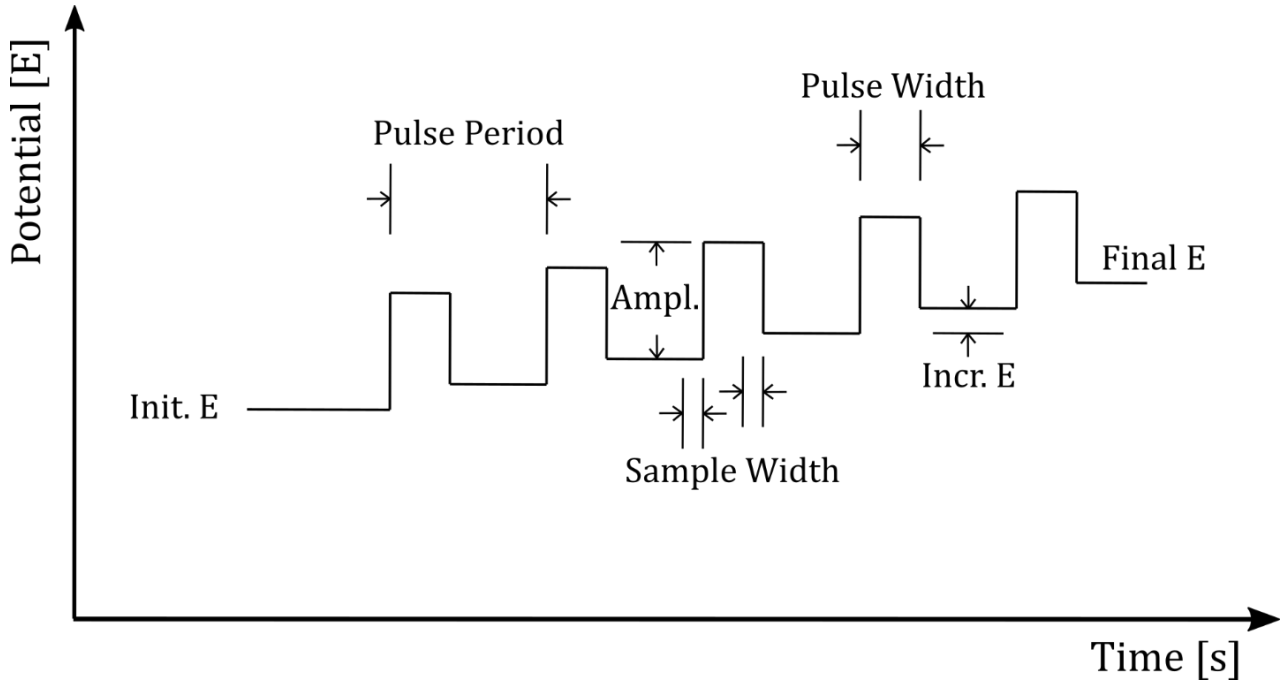

Figure 12: Schematic representation of a DPV experiment.

The half-wave potential is determined by the following equation:

$$E_{1/2} = E(i_p) - \frac{Amplitude}{2} \tag{9}$$

With $E(i_p)$ being the potential at the maximum of the current at a given peak.

The following parameters are found to lead to a good signal-to-noise ratio and are therefore used for DPV experiments throughout this work:

- incremental potential (Incr. E) = 4 mV
- amplitude = 50 mV
- pulse width = 50 ms
- sampling width = 16.7 ms
- pulse period = 500 ms.

8.3 Electrochemical Gating

The working principle of ECG is similar to that of an FET[98, 99] where p- or n- doped semiconductor materials change their conductive properties when the gate electrode is positively or negatively polarized.

As mentioned in **Chapter 7.3**, it is difficult to apply chemical doping to semiconductor QDs through the introduction of foreign atoms, so their doping level has to be controlled by electrochemically injecting electrons or holes into the material. This adds another difference to FETs: There, an isolation layer is placed between the gate electrode and the semiconductor. This way, no direct flow of charge carriers from the gate to the analyte material is possible and the main effect on the semiconductor is capacitive charging of the semiconductor film through the gate's electric charge[100].

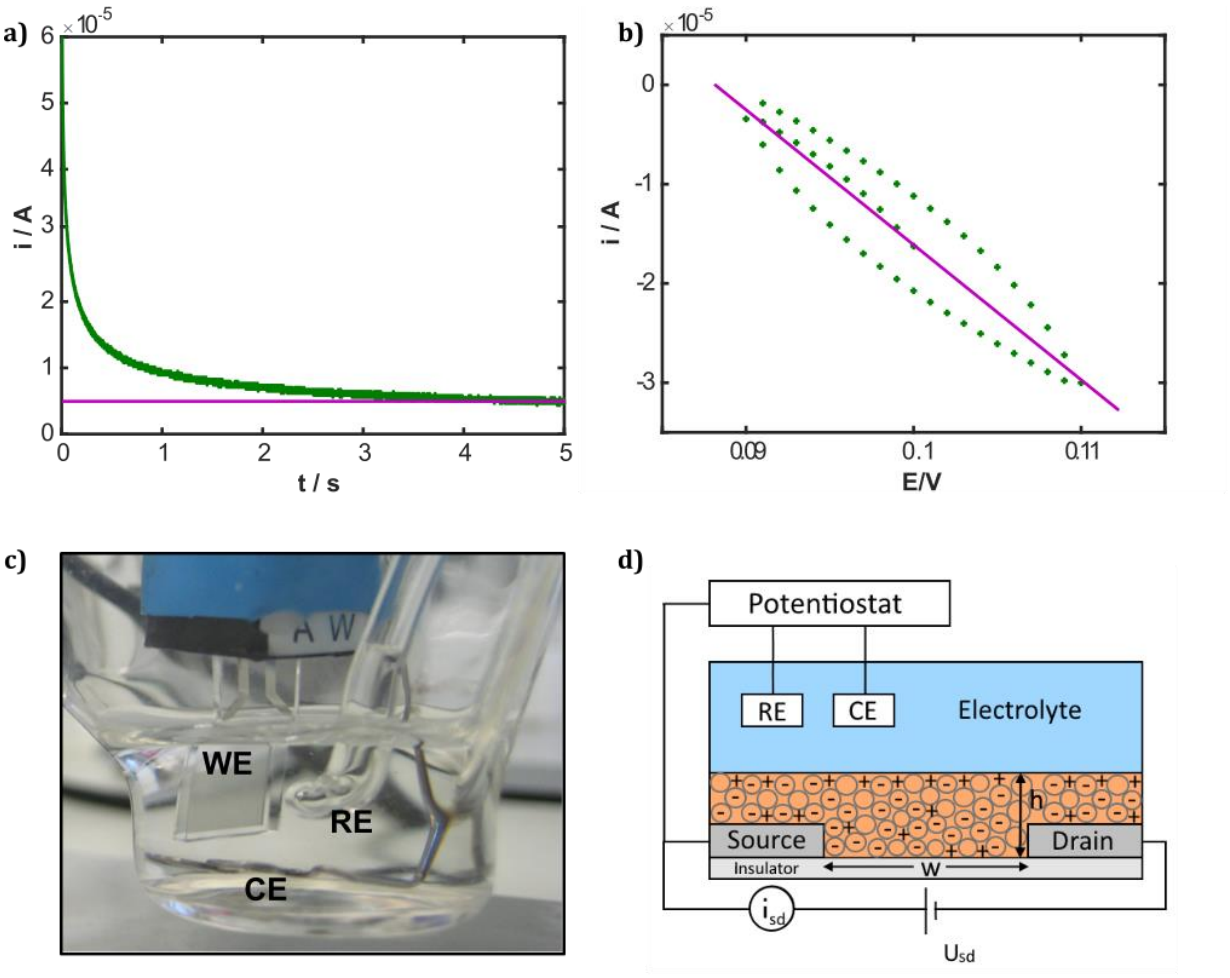

Figure 13: Measurement principle and experimental setup of ECG.
a) Measurement of differential charge by CA (green curve: measured data, purple line: fitted line for background correction). b) Measurement of steady-state conductance by CV (green dots: measured data, purple line: linear fit of the data). c) Photograph of the experimental setup. d) Sketch of the electrode setup of an ECG experiment (Modified from Ref[99]).

In an ECG experiment, electrons are actually injected into the semiconductor film by the gate. Just like chemical doping moves the Fermi level closer to the CB (n-type) or the VB edge (p-type), electrochemical doping does the same. With a small number of electrons (holes) in the CB (VB), these charge carriers can move freely, thus leading to a conducting material.

If the LUMO (HOMO) of an organic semiconducting linker molecule aligns with the CB (VB), the charge carriers can leave the QD and be injected into the linker molecule and from there into the next QD leading to the long range conductance of a COIN film (see **Chapter 7.3**). It is therefore very interesting for the characterization of COIN films to know exactly over which energy level the film conductance occurs. This can to the best of my knowledge only be measured with ECG.

In an ECG experiment, chronoamperometry (CA) is combined with steady-state conductance measurements. This way, the Fermi level of the QD network can be increased by changing the WE to cathodic potentials. This leads to an injection of electrons from the WE into the QD film. These negative charges are compensated by positively charged ions from the solution that permeate into the film (see **Chapter 8.1.2**)[98, 99, 101].

The differential charge ($\Delta Q(E_e)$) injected to the QD film per potential step is measured by applying a small potential step (20 mV in this work) to both WEs simultaneously ($E_e(WE1) = E_e(WE2)$) and recording the current that flows between each of the WEs and the CE ($i = i1 + i2$). The area under the curve, corrected for faradaic background currents is used as a measure of the differential charge. In this work, background correction is achieved by fitting a line parallel to the x-Axis that runs through the last 200 datapoints of the curve (**Figure 13a**, see MatLAB script in **Appendix 14.1.3**).

As the injected charge per potential step is accumulated in the COIN film, the values of the measurement above are integrated according to the following equation[98]:

$$Q(E_e) = \frac{1}{20mV} \int_{E_{e,start}}^{E_{e,end}} \Delta Q(E_e) dE_e \tag{10}$$

The so-called “steady-state” conductance (because it is measured after a sufficient waiting time after the potential step to allow the charge in the film to reach a steady-state[102]) is measured by scanning the potential of the source electrode (WE1) around the potential of the drain electrode (WE2) by a small potential range (typically +- 10 mV)[98, 99, 101] (**Figure 13b**). The steady-state conductance is derived from the measured data by applying a linear fit (see MatLAB script in **Appendix 14.1.3**) and using the slope of this line according to the following equation:

$$G = \frac{\Delta i_{sd}}{\Delta U_{sd}} \left[\frac{A}{V} = S\right] \tag{11}$$

The conductivity can be derived from the steady-state conductance by multiplying it with a geometrical factor[102]:

$$\sigma = \frac{w}{l \cdot h} \cdot G \left[\frac{A}{Vm}\right] \tag{12}$$

Here, w is the width of the gap between the electrodes ($5 \cdot 10^{-4}$ cm), l is the total length of the gap. For an IDE with 250 dents per side, that makes 500 dents in total, leading to 499 gaps between dents. As one dent is 0.676 cm long, the total gap for this kind of IDE is 499·0.676 cm = 337.324 cm. h is the height of the QD film (approximately 10^{-5} cm for a film consisting of 10 layers of PbS QDs as determined by SEM). The values cited here correspond to the electrodes used in this work.

The charge carrier mobility is defined as[102]:

$$\mu = \frac{d\sigma}{dN} \left[\frac{A}{mV}\right] \tag{13}$$

The charge carrier concentration (N) is determined by dividing the injected charge by the volume of the film. The volume is calculated by multiplication of the active area of the electrode by the thickness of the film.

$$N = \frac{Q}{V} \left[\frac{C}{m^3}\right] \tag{14}$$

By inserting **Equations 12** and **14** into **13**, the following equation for the charge carrier mobility is obtained:

$$\mu = \frac{d\left(\frac{w}{l \cdot h} \cdot \frac{\Delta i_{sd}}{\Delta U_{sd}} \left[\frac{A}{mV}\right]\right)}{d\left(\frac{Q}{V} \left[\frac{C}{m^3}\right]\right)} \tag{15a}$$

$$\mu = \frac{w}{l \cdot h} \frac{d(G)}{d\left(\frac{Q}{V}\right)} \left[\frac{Am^3}{mVC}\right] \tag{15b}$$

$$\mu = \frac{w}{l \cdot h} \frac{d(G)}{d\left(\frac{Q}{V}\right)} \left[\frac{m^2}{Vs}\right] \tag{15c}$$

When measuring the conductance of a porous semiconducting material immersed into a conducting electrolyte solution, some thought has to be given to the question which pathway of conductance is actually measured in the experiment: the one through the QD film (**Figure 14a**) or the one through the electrolyte solution. This problem is excellently explained in a paper from Meulenkamp[103].

The two pathways of charge carrier flow can be described as i_{Film} (the intended flow of electrical current from the source electrode to the drain electrode through the QD film) and i_{Elec} (the unintended flow of electrical current from the source electrode to the drain electrode through the electrolyte solution) (**Figure 14b**). As the experiment is carried out with direct current (DC), a set of resistances can be introduced:

- The resistance of the source and drain electrode (R_{Pt})
- The resistance of the QD film (R_{Film})
- The resistance of the electrolyte (R_{Elec})
- The charge transfer resistance between the QD film and the electrolyte (R_{CT})

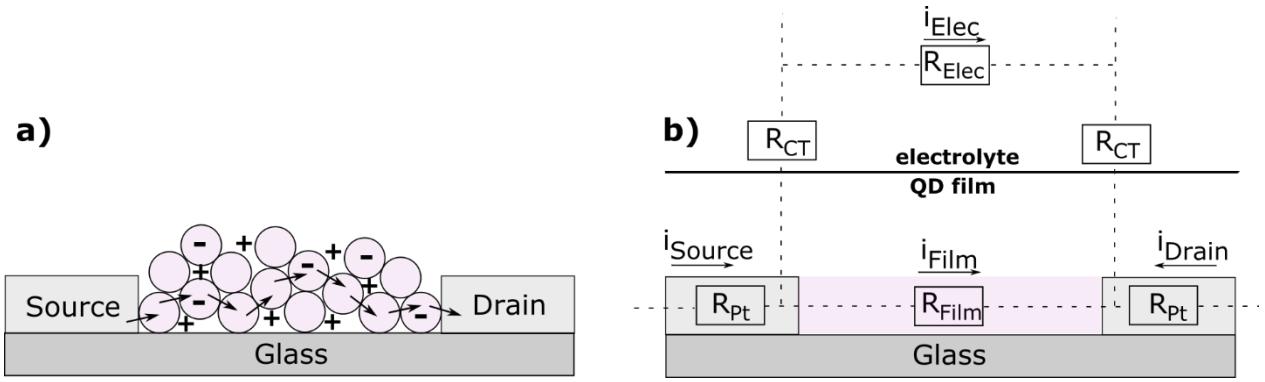

Figure 14: Sketch of the charge carrier flow from source to drain electrode in an ECG experiment. a) A negative charge leaves the source electrode, propagates through the QD film and enters the drain electrode. b) Schematic representation of currents and resistances in an ECG setup. (Modified from Ref[103])

The current measured through the WEs is described as i_{Source} and i_{Drain} and consists of currents through the electrode, the film and the electrolyte.

$$i_{Source} = i_{Pt} + i_{Film} + i_{Elec} \tag{16}$$

$$i_{Drain} = i_{Pt} - i_{Film} - i_{Elec} \tag{17}$$

To successfully conduct an ECG experiment, two requirements must be fulfilled:

1) The electrode resistance must be sufficiently smaller than the film resistance ($R_{Film} >> 2* R_{Pt}$). By the time Meulenkamp wrote the paper, indium tin oxide (ITO) was often used as an electrode material and might still be used when optical transparence of the experimental setup is required. The disadvantage of ITO is its high resistance compared to the Pt electrodes used throughout this work. So this requirement is expected to be fulfilled with the setup used here because the Pt electrodes are expected to be several orders of magnitude more conductive than the QD film.
2) The film resistance must be substantially smaller than the resistance over the unintended pathway through the electrolyte ($R_{Film} << 2\cdot R_{CT} + R_{Elec}$).
   This can be measured by running an ECG experiment without a QD film on the electrode. With the setup used in this work, usually resistances in a range of 10^6 - 10^7 Ω are measured without a QD film and resistances in a range of 10^2 - 10^3 Ω are measured when a QD film is filling the gap between the source and drain electrode. With the film resistance being a factor of 10^4 smaller than the resistance of the unintended pathway, this requirement is also fulfilled for the setup used in this work.

8.4 Spectroelectrochemistry

The principle behind SE of semiconductors is that the optical transition from the VB to the CB can only occur when there are electrons in the VB and vacancies in the CB (**Figure 15a,** upper left and lower right corner). This state is achieved when the Fermi level is located somewhere in the band gap. As the Fermi level of the WE can be controlled by the potentiostat, it is possible to shift it to energies higher than the CB edge or lower than the VB edge. In the first case, transitions from the VB edge to the CB edge are weaker because the vacancies in the CB are already occupied by electrons (**Figure 15a**, lower left corner). In the second case the optical transition is weaker because there are less electrons in the VB that could be excited (**Figure 15a**, upper right corner).

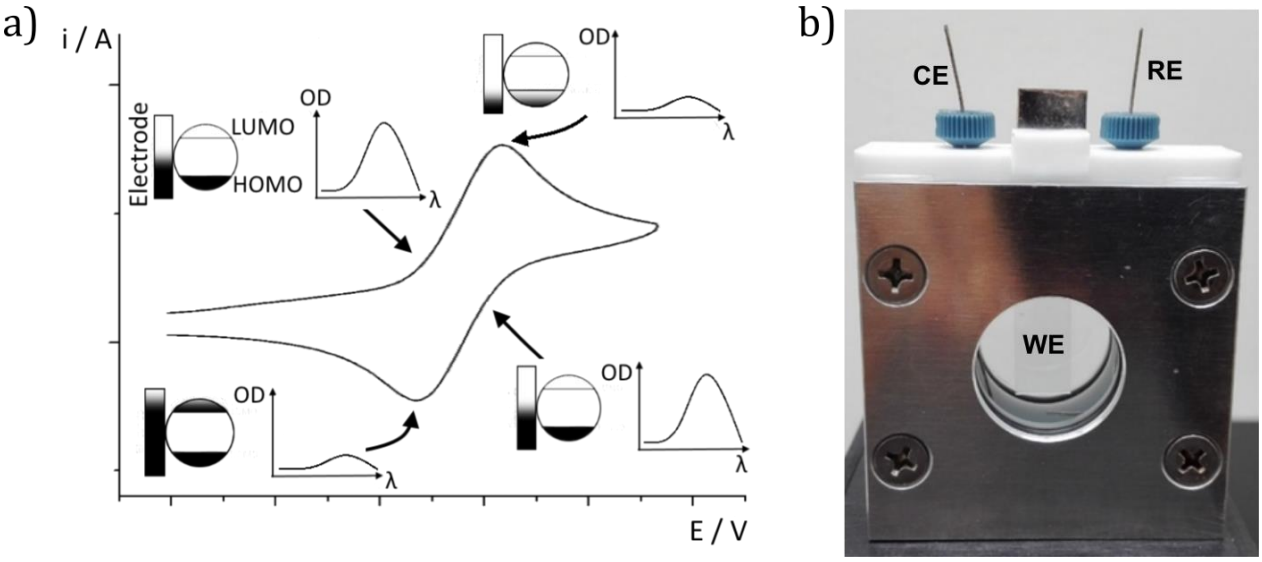

Figure 15: Measurement principle and experimental setup of SE.
a) Working principle of SE. Optical transitions get weaker when electrons are pulled out of the VB or injected into the CB. b) Transparent cell for SE and EMAS: Teflon housing, aluminum front and back plates, transparent windows, silver RE, platinum CE and FTO WE.

For the experiments in this work, a home built transparent electrochemical cell (**Figure 15b**) is fitted into a Cary 5000 Spectrophotometer. An Ag wire is used as pseudo RE and a Pt wire as CE. An FTO (DN-HG12, 20 ohm/cm^2, Dyenamo) platelet is connected to a Pt sheet with silver glue and used as the WE. The reference channel of the spectrometer is left unfilled and a baseline of the cell with FTO WE and electrolyte is recorded. The WE is then polarized with a constant potential and a spectrum is taken. This spectrum is subsequently divided by the baseline to subtract the background.

8.5 Potential Modulated Absorption Spectroscopy

8.5.1 The Setup

The EMAS setup was first described by Riley et. al in 2000[104-106] and has since found application in research groups around the world[107-110].

The speciality of this particular setup is that it uses a quartz tungsten halogen (QTH) lamp (Apex2, Newport) instead of a Xenon Arc lamp, providing a smoother excitation spectrum and the possibility to investigate QD systems with absorptions in the near infra-red (NIR) region. It also lacks a frequency generator that is used by some groups to generate the modulated signal. Here, this signal is instead generated by the internal oscillator of the lock-in amplifier (LIA) which eliminates a number of cables and connections that have been identified as sources for noise pickup and measurement error.

A monochromator (Cornerstone 130 1/8 m extended range Monochromator, 4 nm resolution, 300 – 2200 nm spectral band width, Ebert-Fastie design) is used to select a wavelength and a set of lenses is used to focus the light on the sample. The sample is applied to FTO glass (DN-HG12, 20 ohm/cm^2, Dyenamo) according to the procedures described in **Chapter 10.2.2**.

The light is collected with a biased photodetector (DET36A, Thorlabs) and the output signal is split and fed into the LIA (MFLI, Zurich Instruments). The opto-mechanical components (lenses, rail, lens holders etc.) are purchased from Thorlabs. The electrochemical cell is home built in cooperation with the university's mechanical workshop and is the same cell as used for SE experiments (see **Chapter 8.4**). The DC potential (E_{DC_ref}) is set by a potentiostat (CHI, model 760E) that is directly connected to the electrochemical cell.

The electrochemical cell, opto-mechanical components and detector are placed in a Faraday cage to minimize noise pickup (**Figure 16**).

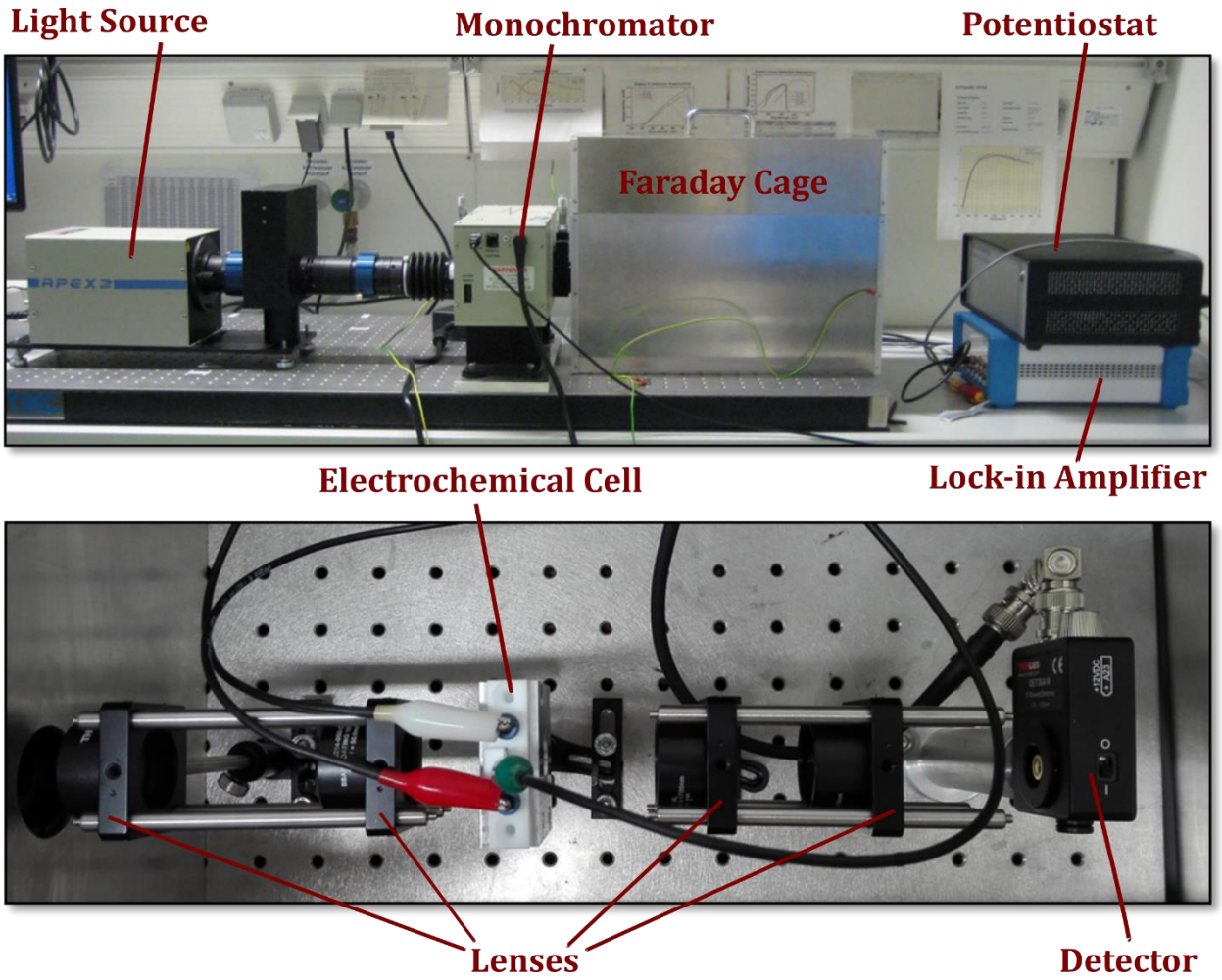

Figure 16: Photographs of the EMAS setup showing its various components.
above: View of the full EMAS setup. **below:** Detailed view of optical and electrochemical components inside the Faraday cage.

8.5.2 The EMAS Measurement Principle

As a first approximation, the EMAS measurement can be described similarly to an SE experiment (see **chapter 8.4**). While the Fermi level is located in the band gap, optical transitions from occupied states in the VB to unoccupied states in the CB can happen.

If the Fermi level is either increased above the states in the CB or decreased below the states in the VB, the optical absorption is quenched. By scanning the WE towards negative potentials, the CB edge is encountered at the potential where the absorption is quenched.

As it is usually easier to detect the CB edge ($1S_e$), the VB edge ($1S_h$) is calculated by adding the energy of the optical band gap ($E_{g,opt}$) and the coulomb correction term[2].

$$E_{1Sh} = E_{1Se} + E_{g,opt} + \frac{1.8e}{4\pi\varepsilon_r^{\infty}\varepsilon_0 r} \tag{18}$$

The reason why EMAS instead of SE is used to investigate QDs, lies in the very minute change in optical density that is induced by the variation of the electrochemical potential.

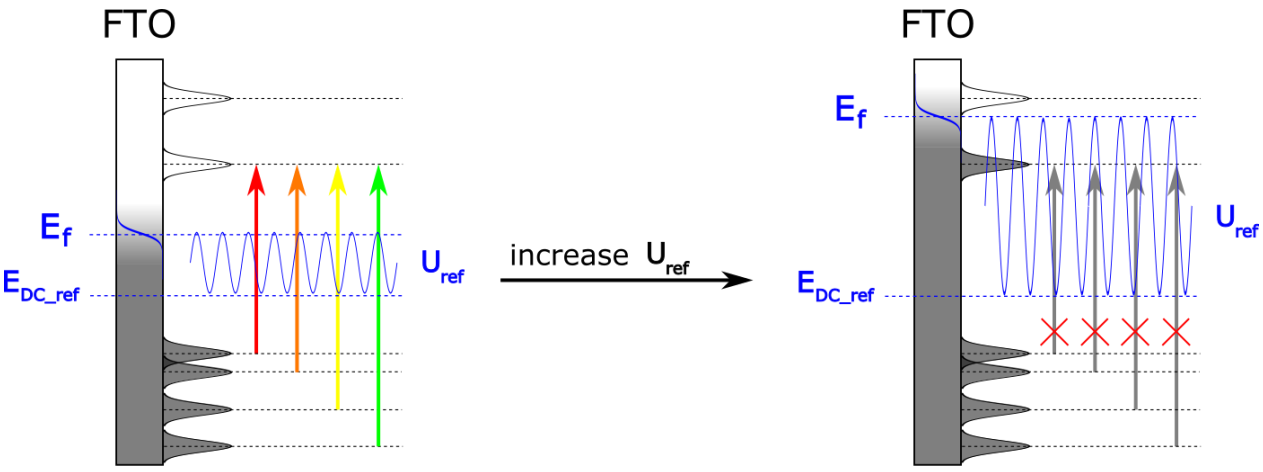

Figure 17: Principle of the optical bleaching dependent on the amplitude of U_{ref} that is used in EMAS. Optical transitions from states in the VB to states in the CB are possible as long as the Fermi level is located in the band gap (left). When the Fermi level is raised above the $S1_e$ state, optical transitions get quenched (right). An AC potential with a distinct amplitude and frequency is modulated on top of a constant potential inside the band gap. (Modified from Ref[109])

Additionally, a QD film has to be very thin in order to be polarized uniformly in the given amount of time (see **Chapter 8.1.2**). Therefore, the overall QD signal is already weak and the change in absorption is even weaker. Using techniques like SE that work with a steady, unmodulated potential input, yield a very poor signal to noise ratio for the systems investigated here.

In an EMAS measurement, an unmodulated, steady potential (E_{DC_ref}) that lies inside the band gap is applied to the WE. Then, a sinusoidal signal is modulated on top of E_{DC_ref}. This sinus signal has an amplitude U_{ref}, a frequency ω_{ref} and a phase θ_{ref}. The Fermi level of the electrode (E_f) is now the sum of E_{DC_ref} and U_{ref} (**Figure 17**, left).

If this modulated Fermi level is above the CB edge, some optical transitions are bleached, if it is below the CB edge, they are visible. So it can be observed that the optical properties of the sample change with frequency ω_{ref} (**Figure 17**, right). The LIA is able to filter out only signals that are modulated with this specific frequency. This way, the signal to noise ratio is hugely improved.

The detected peak to peak amplitude V_{PP} is calculated from the root mean square (RMS) value of the signal amplitude (see **Chapter 8.5.4**). This amplitude is a measure for how much the absorption changes relative to a given polarization.

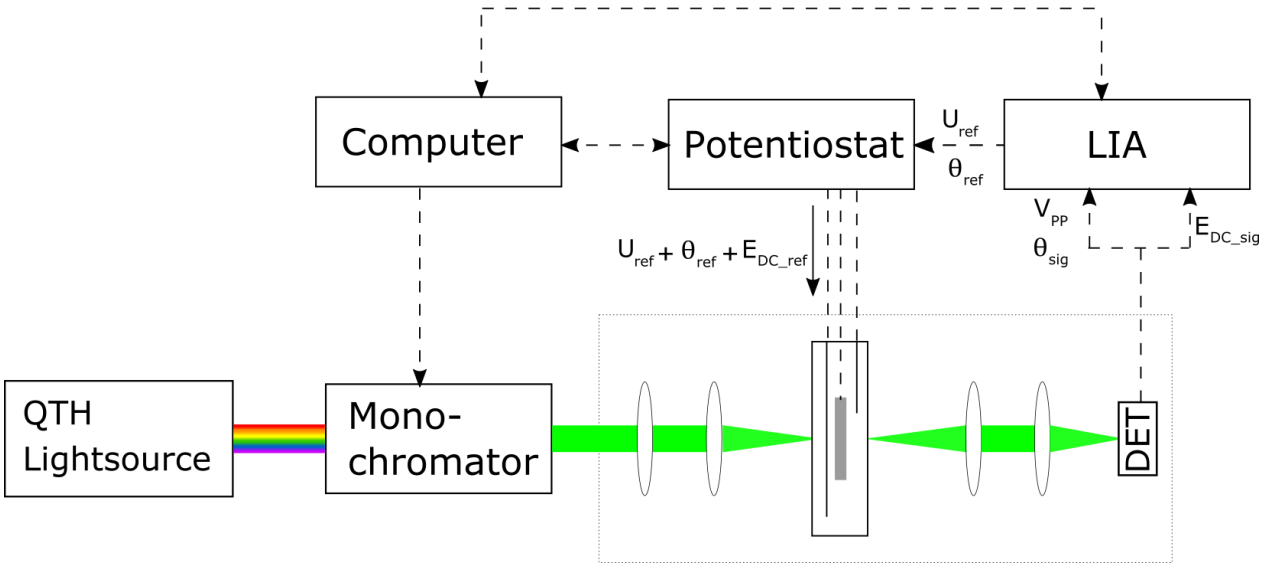

Figure 18: Sketch of the EMAS setup and the signal pathways.

8.5.3 Lock-in Amplification

LIAs are used to measure very small (nV range) alternating current (AC) signals and distinguish them from a noise background that may be many thousand times larger. This is achieved by a technique called phase-sensitive detection, which picks a signal of a specific frequency, locks the frequency and detects the phase and the amplitude of that signal while rejecting all other signals.

Typically, an experiment is performed by exciting a system with a specific frequency which is also fed to the LIA as the reference frequency. The LIA takes this reference frequency and couples it to its internal reference oscillator through a phase-locked loop.

This ensures that not only the frequency of the signal and the reference are the same, but also the phase[100].

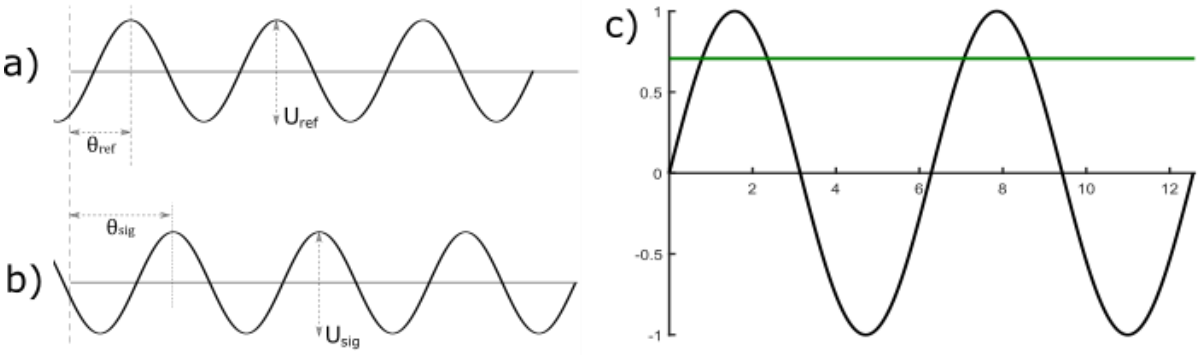

Figure 19: Signals processed by the LIA:
a) Internally generated reference signal of the LIA, b) incoming measurement signal and c) sine wave (black) with its RMS value (green). The RMS value is calculated according to **Equation 24**.

This way the LIA is getting the following information:

- The reference frequency (ω_{ref})
- The reference phase (θ_{ref})
- The magnitude of the reference signal (U_{ref})
- The signal frequency (ω_{sig})
- The signal phase (θ_{sig})
- The magnitude of the measured signal (U_{sig})

The phase sensitive detector (PSD) of the LIA now takes the reference as well as the measured signal sine function and calculates its product according to[111]:

$$U_{psd1} = U_{sig}U_{ref}\, sin\big(\omega_{sig}t + \theta_{sig}\big)\, sin\big(\omega_{ref}t + \theta_{ref}\big) \tag{19a}$$

$$U_{psd1} = \frac{1}{2}U_{sig}U_{ref}\, cos\big(\big[\omega_{sig} - \omega_{ref}\big]t + \theta_{sig} - \theta_{ref}\big) - \frac{1}{2}U_{sig}U_{ref}\, cos\big(\big[\omega_{sig} + \omega_{ref}\big]t + \theta_{sig} + \theta_{ref}\big) \tag{19b}$$

It can be seen that the signal of the PSD (U_{psd}) consists of two AC signals, one at the difference frequency ($\omega_{sig} - \omega_{ref}$), one at the sum frequency ($\omega_{sig} + \omega_{ref}$) of the two ingoing signal sources. When this signal is passed through a low pass filter, all AC components are filtered out. The only signal left is the part for which the frequency of

the measured signal equals the reference frequency ($\omega_{sig} = \omega_{ref}$). **Equation 19b** then simplifies to:

$$U_{psd1} = \frac{1}{2} U_{sig} U_{ref} \cos(\theta_{sig} - \theta_{ref}) \tag{19c}$$

As the magnitude of the reference signal (U_{ref}) and the phase of the reference signal (θ_{ref}) are constant, U_{psd} only depends on the magnitude (U_{sig}) and the phase shift (θ_{sig}) of the measured signal. This is problematic because at a phase shift 90°, the phase sensitive detector will not find any signal (cos(90°) = 0) when there is in fact a signal. This is why LIAs have two PSDs where the first measures the signal as described above and the second multiplies this signal with the oscillator shifted by 90°.

$$U_{psd2} = \frac{1}{2} U_{sig} U_{ref} \sin(\theta_{sig} - \theta_{ref}) \tag{20}$$

It can be said that the signal of the first PSD is proportional to $U_{sig} \cos(\theta)$, while the signal of the second PSD is proportional to $U_{sig} \sin(\theta)$.

$$X = U_{sig} \cos(\theta) \tag{21}$$

$$Y = U_{sig} \sin(\theta) \tag{22}$$

$$R = \sqrt{X^2 + Y^2} \tag{23}$$

R is the output signal of the LIA. It is not the amplitude of the measurement signal, but the RMS value. The RMS is defined as the root of the area between the graph and the x-axis of a wave for one full period (**Figure 19c**).

8.5.4 Data Analysis - From Raw Data to Results

To use the raw data from the LIA to analyze an EMAS experiment, a few transformations need to be made. The LIA returns an RMS value instead of an amplitude, which needs to be converted by using the definition of an RMS value for a sine wave:

$$R = \frac{A}{\sqrt{2}} \tag{24}$$

With A being the amplitude of the measured signal.

In the EMAS experiment the sine wave is modulated on top of a constant potential, so the value of interest is the peak-to-peak amplitude (V_{pp}) which is twice the amplitude[100].

$$V_{pp} = R \cdot 2 \cdot \sqrt{2} \tag{25}$$

The plot of an EMAS measurement is therefore the signal amplitude (V_{pp}) plotted against the wavelength. One curve is plotted for each amplitude of the input signal (U_{ref}).

To make changes at one specific optical transition easier to read, the signal may also be plotted as a voltabsorptogram. Hereby, the dataset of one wavelength is plotted with V_{pp} on the y-axis and the amplitude of the input signal (U_{ref}) plus the potentiostat reference signal (E_{DC_ref}) referenced against the ferrocene/ferrocenium couple on the x-axis.

As indicated in **Chapter 8.5.2**, three sets of data are obtained simultaneously for each EMAS experiment: E_{DC_sig}, V_{PP} and θ_{sig}.

E_{DC_sig} can be understood as the intensity of the light source multiplied by the sensitivity of the detector and the efficiency of the monochromator grating for a certain wavelength minus the unmodulated absorption of the sample. In this work, it is solely used to confirm that the equipment works as intended and that there are no errors in the analysis script (see MatLAB script in **Appendix 14.1.4**).

V_{PP} only gives the magnitude of the detected signal, it does not tell anything about whether that change is an induced absorption or a bleach. To clarify that, θ_{sig} is recorded.

For a bleach, the absorption is expected to go down upon increasing the electrochemical potential of the WE. This can be described as a signal sine curve with a signal phase θ_{sig} shifted by 180 ° with regard to the reference phase θ_{ref} (see **Figure 19**). An optical signal that grows upon increasing the electrochemical potential is in phase ($\theta_{ref} = \theta_{sig}$) with the reference signal and therefore formally shifted by 0°.

These values however assume ideal behavior of the experimental setup. In reality, the applied signal needs time to induce the process that causes the optical signal to change. The phase shift is influenced by the reaction time of the electrochemical processes in the cell as well as in the sample. Also, the detector needs a finite time to detect and pass on the signal.

To reflect this non-ideal behavior of the setup in the analysis of the data, a range around 180° and 0° phase shift is used for data evaluation rather than absolute values. Therefore, all signals below a ±90° shift are declared as “0°” (induced absorption) and all above as “180°” (bleach).

The data is recorded in discrete steps by setting a potential and a wavelength. After waiting for two seconds to avoid the pickup of any unwanted electromagnetic noise resulting from the operation of the monochromator, the signal is recorded for two seconds and another second is waited before going to the next wavelength. The mean of these two seconds of collected data are used for further analysis. The plots (see **Figure 36**) also show error bars of 1 standard error of the mean.

9 Materials

9.1 Synthesis of Linker Molecules

9.1.1 Synthesis of the Terthiophene linkers

This synthesis is performed by Kai Wurst.

5,5‘‘-dithiol-[2,2‘:5,2‘‘-terthiophene]-1,3-diyldiethanethioate (T3DSAc) is synthesized according to a procedure described in the literature[112, 113]. A detailed description of the synthesis can also be found in[114]. 5,5‘‘-dithiol-[2,2‘:5,2‘‘-terthiophene] (T3DSH) is obtained by an ester hydrolysis with sodium hydroxide[114].

9.1.2 Synthesis of the Phthalocyanine linkers

This synthesis is performed by Markus Katzenmeyer.

Copper-4,4‘,4‘‘,4‘‘‘-tetranitrophthalocyanine (CuPc) and zink-4,4‘,4‘‘,4‘‘‘-tetranitrophthalocyanine (ZnPc) are synthesized according to the procedure described by Jung et. al[115]. Metal free 4,4‘,4‘‘,4‘‘‘-tetranitrophthalocyanine (H_2Pc) is synthesized according to a procedure described by Alzeer et al.[116]. Here, the ZnPc is cooked in pyridine-HCl for 17 h at 120 °C.

The other metal phthalocyanines cobalt-4,4‘,4‘‘,4‘‘‘-tetranitrophthalocyanine (CoPc), nickel-4,4‘,4‘‘,4‘‘‘-tetranitrophthalocyanine (NiPc) and iron-4,4‘,4‘‘,4‘‘‘-tetranitrophthalocyanine (FePc) are purchased from ABCR GmbH.

9.2 Synthesis of QDs

9.2.1 Equiment Used for QD Synthesis

All QD synthesis procedures described in this chapter are carried out in the apparatus depicted in **Figure 20**. A temperature sensor is inserted into a glass tip that reaches down to the reaction mixture while also ensuring that the apparatus is closed airtight and can be evacuated. The precursor solution is injected through a septum. The reflux cooler is connected to a Schlenk line, enabling the operator to alternate the atmosphere in the flask between a vacuum and nitrogen[4].

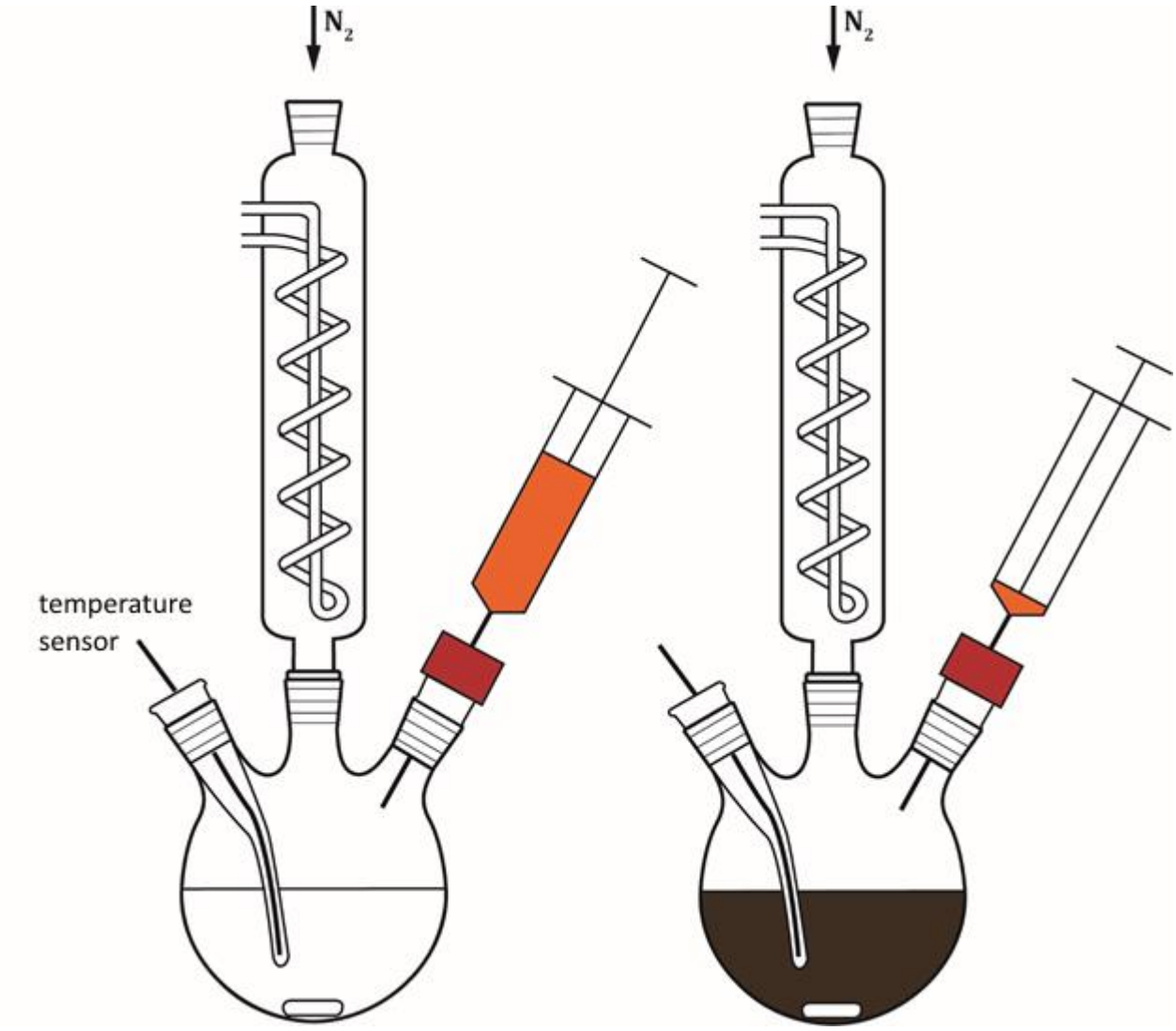

Figure 20: Apparatus used for NP synthesis.
left: State of the apparatus before the injection of the precursor. **right:** After injection of the precursor, the reaction mixture often changes color. (Modified from Ref[45])

For the purification of the QDs, a number of precipitation and centrifugation steps need to be executed. These are performed in a Sigma 2-6 centrifuge.

The QDs are characterized by ultraviolet-visible-near infrared (UV-Vis-NIR) spectroscopy in an Varian Cary 5000 spectrophotometer and scanning electron microscopy (SEM). SEM images are recorded with a Hitachi SU8030 microscope by Elke Nadler.

9.2.2 Synthesis and Characterization of $Cu_{1.1}S$ Nanoplatelets

This synthesis is performed by me.

9.2.2.1 Synthesis

$Cu_{1.1}S$ nanoplatelets are synthesized after a procedure initially reported by Xie et al.[117] that is upscaled by Wolf et al.[118].

40 mL (*Z*)-octadec-9-enylamine (OLA, Acros Organics, 80 – 90 %), 40 mL 1-octadecene (ODE, Acros Organics, 90 %) and 256.5 mg sulfur are filled into a 100 mL three neck flask and connected to an apparatus as depicted in **Figure 20**. The mixture is degassed for 30 min under vacuum at 120°C. The flask is then filled with nitrogen and the temperature raised to 130 °C for 5 min. Afterwards, the mixture is cooled down to room temperature and 400 mg CuCl are added. The flask is again evacuated for 60 min at room temperature. After filling it with nitrogen, the temperature is raised at a ramp of 8 °C per minute to 200 °C and then kept there for 30 min.

The QDs are purified by adding 40 mL of ethanol and centrifuging for 20 min at 4000 rpm. After discarding the supernatant, the precipitate is redissolved in 40 mL toluene. The resulting dark brown particle solution is centrifuged at 100 rpm for 5 min to remove larger side products. The supernatant is again precipitated with 40 mL ethanol, centrifuged for 5 min at 4000 rpm and the precipitate redissolved in 30 mL hexane.

9.2.2.2 Characterization

A UV-Vis-NIR spectrum is recorded of the dissolved particles in tetrachloroethylene (TCE, Sigma Aldrich, anhydrous, > 99 %). The particles show no excitonic peak, however this is in line with spectra found in the literature[118-120]. The large LSPR peak at around 1400 nm indicates that the QDs are metallic as is expected for particles with a $Cu_{1.1}S$ stoichiometry[118].

SEM is performed to quantitatively assess the size distribution and appearance of the QDs. The particles show a narrow size distribution (15.5±1.7 nm for n = 500) with particles trending towards a hexagonal long range order in a dropcasted film. The film is prepared by the procedure described in **Chapter 10.1.2**.

The size distribution as shown in the inset in the SEM image may be broadened due to the disk-like shape of the QDs. Having different orientations of QDs in the micrograph makes it harder to measure them always on their longest axis.

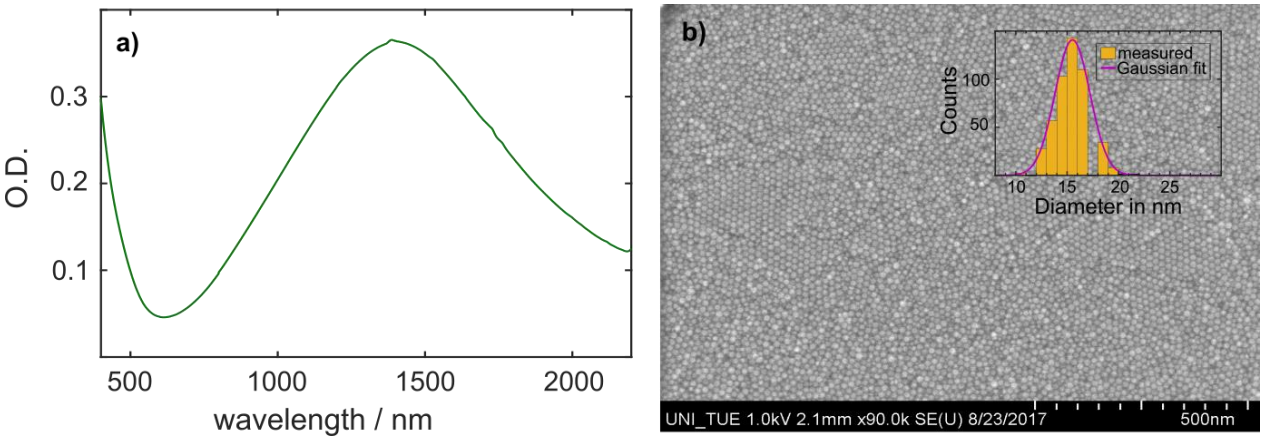

Figure 21: Characterization of the $Cu_{1.1}S$ nanoplatelets by UV-NIR spectroscopy and SEM.
a) Vis-NIR spectrum of as synthesized $Cu_{1.1}S$ nanoplatelets dissolved in TCE. b) SEM image of $Cu_{1.1}S$ nanoplatelets on a silicon substrate, prepared after the above described dropcasting procedure. The inset shows the size distribution of the QDs as analyzed from the SEM micrograph with the ImageJ software.

9.2.3 Synthesis and Characterization of PbS QDs with $PbCl_2$ as Precursor

This synthesis is performed by me.

9.2.3.1 Synthesis

PbS QDs are synthesized by a procedure modified from the work of Weidman et.al. [6].

0.040 g of sulfur and 7.5 mL of OLA are filled into a 20 mL glass vial and placed on a magnetic stirrer at room temperature in a nitrogen filled glovebox overnight.

7.5 g of $PbCl_2$ and 22.5 mL of OLA are filled into a 100 mL three neck flask and connected to an apparatus as depicted in **Figure 20**. The system is evacuated for ~ 30 minutes until the bubble formation in the liquid stops. Then the mixture is heated to 120 °C under nitrogen. Care must be taken in this step that the $PbCl_2$ powder stays well suspended in the OLA. 6.75 mL of sulfur solution is swiftly injected. The temperature subsequently drops to ~ 100 °C, but rises to 120°C within 1-2 min. An overshoot of temperature is prevented by tuning down the thermostat shortly before reaching 120 °C.

After the reaction time (typically 30 min), the mixture is rapidly cooled down by replacing the heating mantle with a water bath and injecting 60 mL of hexane. The reaction mixture is transferred to a nitrogen-filled glovebox and precipitated with

~ 80 mL ethanol. The suspension is centrifuged with 4000 rpm for 5 minutes and the supernatant is discarded. This first precipitation step is time critical since the supernatant contains unreacted sulfur precursor that can widen the size distribution of the QDs if it is left in the reaction mixture for too long.

The precipitate is redispersed in ~ 80 mL hexane. There is still unreacted $PbCl_2$ in that mixture that needs to be separated from the QD solution. That is done by centrifuging it again at 4000 rpm for 5 minutes and discarding the white precipitate.

The QDs are again precipitated by ~ 80 mL of ethanol and after discarding the supernatant, 4 mL of degassed oleic acid (OA, Aldrich, 90 % technical grade) are added and the mixture is stirred with a spatula. After leaving the mixture stand for minimum 1 h, it is cleaned three times by a.) adding ~ 80 mL hexane, b.) adding ~ 80 mL of ethanol, c.) centrifuging at 4000 rpm for 5 minutes and discarding the supernatant after centrifugation.

9.2.3.2 Characterization

The characterization is performed after a method developed by Moreels et. al[121].

A spectrum is taken from a diluted QD solution in TCE. From this spectrum, the wavelength of the first excitonic peak (λ = 1580 nm) and the optical density at 400 nm (OD_{400}) is recorded. SEM is performed to quantitatively assess the size distribution and appearance of the QDs. Both, the well-defined peak in the NIR spectrum as well as the QD sizes measured in the SEM image, suggest a good size distribution. The long range order of QDs in a dropcasted film is also an indication for a narrow size distribution.

From λ, the energy of a photon of this wavelength can be calculated using the Planck-Einstein relation[38].

$$E_{g,opt} = h \cdot \frac{c}{\lambda} \tag{26}$$

with h being the Planck constant and c being the speed of light.

The diameter of the QDs is calculated by changing the empirical formula from Ref[121] to the diameter:

$$d = -5.615 \pm \sqrt{5.615^2 + \frac{1}{\left(E_{g,opt} - 0.41\right) \cdot 0.0252}} \tag{27}$$

For the batch of QDs described above, this leads to a diameter of 6.1 nm when calculating the diameter from the energy of the first excitonic transition. A size of 5.5±0.6 nm is found when measuring the particles from the SEM micrograph. The discrepancy can come from the not ideally round shape of the QDs or measurement inaccuracy because it is difficult to estimate where the QD ends and where the ligand shell starts in the SEM image. It is also possible that the SEM image is recorded on an area of the sample that consists of predominantly QDs at the smaller end of the size range while optical spectroscopy probes a larger number of QDs.

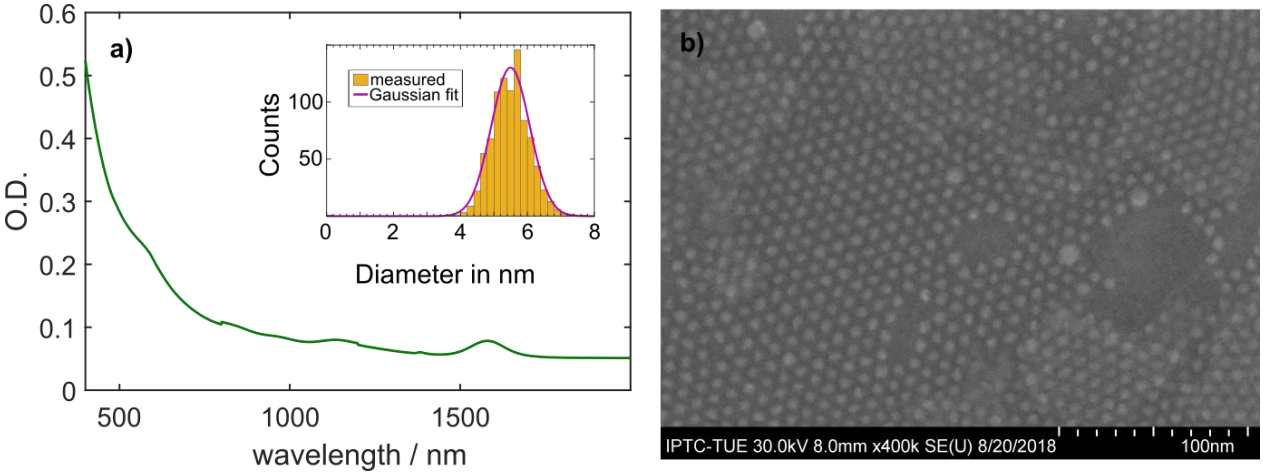

Figure 22: Characterization of the PbS QDs by UV-NIR spectroscopy and SEM.
a) A typical spectrum of PbS QDs in TCE. The peak at 1580 nm is the first excitonic transition. The inset shows the size distribution of the QDs as analyzed from the SEM micrograph with the ImageJ software. b) A typical SEM micrograph of the PbS QDs.

9.2.4 Synthesis and Characterization of PbS QDs with PbO as Precursor

This synthesis is performed by me.

9.2.4.1 Synthesis

This synthesis is carried out according to the work of Ibáñez et. al[122, 123].

A sulfur precursor is prepared by mixing 0.64 g elemental sulfur with 20 mL degassed OLA and left stirring at room temperature overnight in a nitrogen-filled glovebox to fully dissolve the sulfur. 464 mg of PbO are dissolved in 5 mL OA and 10 mL of ODE. The mixture is degassed first at room temperature and then at 100 °C until the bubbling stops. The temperature is subsequently raised to 210 °C and 2 mL of the sulfur precursor is swiftly injected. After 5 minutes, the reaction mixture is quickly cooled down to room temperature. The PbS QDs are cleaned three times by a.) adding hexane,

b.) adding ethanol, c.) centrifuging at 4000 rpm for 5 minutes and discarding the supernatant after centrifugation.

9.2.4.2 Characterization

A spectrum is taken from a diluted QD solution in TCE. Additionally, SEM is measured to assess the size distribution and appearance of the QDs.

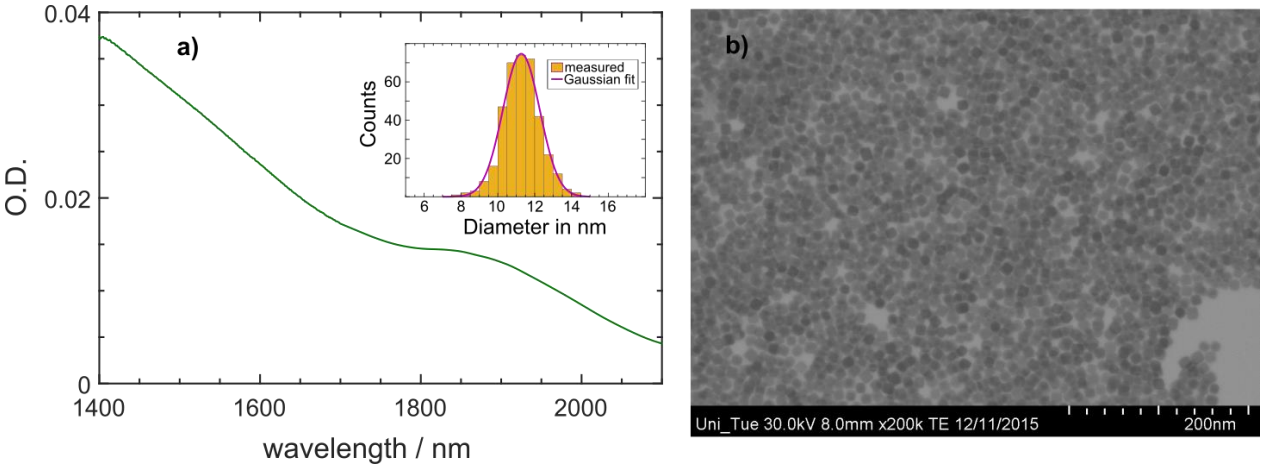

Figure 23: Characterization of the PbS QDs by UV-NIR spectroscopy and SEM.
a) A typical spectrum of PbS QDs in TCE. The peak at 1870 nm is the first excitonic transition. The inset shows the size distribution of the QDs as analyzed from the SEM micrograph with the ImageJ software. b) SEM image of the PbS QDs.

When using **Equation 27** to calculate the diameter of these QDs, a value of 8.1 nm is obtained from the peak at 1870 nm in the NIR spectrum. Analysis of SEM image however shows a diameter of about 11.3±1 nm. It can therefore be assumed that the empirical method to calculate QD diameter as described above[121] does not apply to PbS QDs in this size range. The method also assumes a spherical particle, whereas the PbS particles synthesized with this procedure show more of a cubic shape.

9.2.5 Synthesis and Characterization of CdSe QDs with Butylamine Ligands

This synthesis is performed by Björn Märker.

9.2.5.1 Synthesis

CdSe QDs are synthesized after a procedure from Panda et al.[124].

Briefly: 176.7 mg CdO, 2.2 mL OA, 8 g trioctylphospine oxide (TOPO, Acros Organics, 99 %), 8 g n-hexadecylamine (HDA, Acros Organics, 90 %) and 45.8 mL ODE are loaded

into a 100 mL three-neck flask and kept under vacuum for 2 h. The mixture is then heated up to 300 °C under inert gas. After the solution becomes clear, the mixture is cooled down to 275 °C for 0.5 h before injection. A solution of 1.6 mL 1 M trioctylphosphine-selenium (TOPSe), 6.4 mL trioctylphosphine (TOP, Acros Organics, 90 %) and 8 mL ODE is swiftly injected and the solution is kept at 280 °C for 25 minutes before being abruptly cooled down to room temperature in a water bath.

The QDs are precipitated with ethanol and redispersed in hexane. They are subsequently washed twice with acetone and twice with ethanol and redispersed with hexane.

1ml CdSe solution (~10mg/mL in hexane) and 30-40 mg of ammonium iodide in N-methylformamide (NMF) are stirred for 1 h, to let the phases mix. The mixture is allowed to settle and the bottom layer (QDs in NMF) is retained while the top layer is discarded. The particles are extracted three times with 1 mL hexane each then precipitated with 2 mL toluene and redispersed in 500 µL NMF. They are again precipitated with 200 µL degassed n-butylamine (BA, Sigma-Aldrich, 99.5 %) and redispersed in chloroform.

In case the particles started to precipitate after storage or dilution of the solution, 5 µL of BA are added to keep them suspended.

9.2.5.2 Characterization

A spectrum of a diluted QD solution in hexane is taken. Additionally, SEM is measured to assess the size distribution and appearance of the QDs.

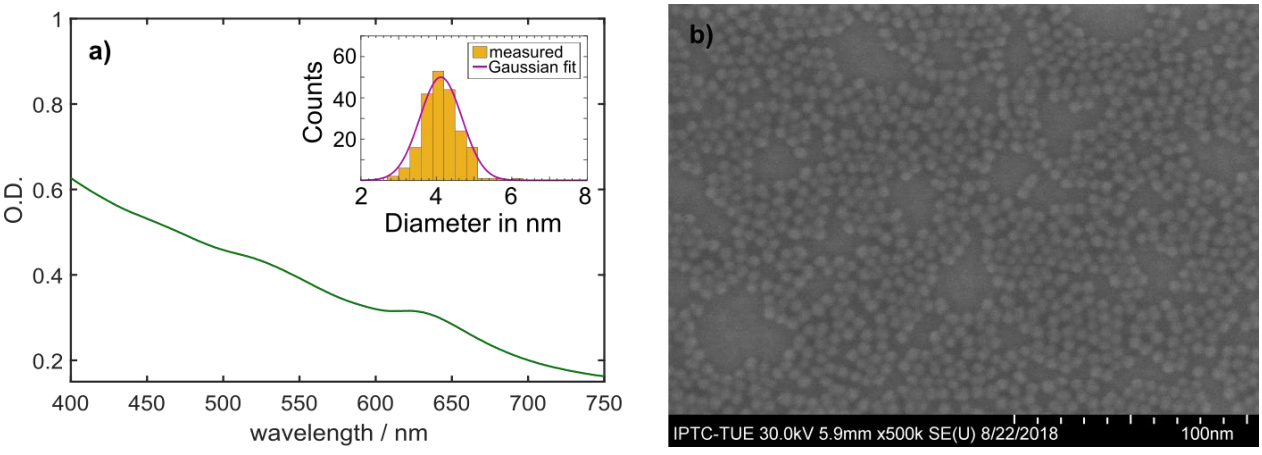

Figure 24: Characterization of the BA capped CdSe QDs by UV-NIR spectroscopy and SEM.
a) Spectrum of CdSe QDs in hexane. The peak at 618 nm is the first excitonic transition. The inset shows the size distribution of the QDs as analyzed from the SEM micrograph with the ImageJ software. b) An SEM micrograph of the CdSe QDs with BA as ligand.

The size of the QDs is determined via measuring the particles from the SEM micrograph with ImageJ software. A value of 4.1 ± 0.6 nm is found with this method.

Another way to assess the size of CdSe QDs is via the position of the first excitonic maximum in the absorption spectrum. The empirical formula found by Yu et al.[125] is valid for a size range of 1.5 – 8 nm CdSe QDs.

$$d = (1.6122 \cdot 10^{-9})\lambda^4 - (2.6575 \cdot 10^{-6})\lambda^3 + (1.6242 \cdot 10^{-3})\lambda^2 - (0.4277)\lambda + 41.57 \quad (28)$$

d is the diameter of the QDs, λ is the wavelength at the first excitonic maximum.

For the CdSe QDs described here, this formula yields a diameter of 5.5 nm. The quite large difference of diameters may be due to the two measurements being conducted some time apart. The spectroscopic measurements are conducted right after particle synthesis while the SEM images are recorded several months later and after the solution was used for the dipcoating procedures to fabricate the samples used in this work. It might be that the smaller particles from the solution are favored for the film formation so that the solution becomes richer in larger particles.

9.2.6 Synthesis and Characterization of CdSe QDs with TOP Ligands

This synthesis is performed by Björn Märker.

9.2.6.1 Synthesis

Wurtzite structure CdSe QDs with TOP ligands are synthesized after a procedure from Chen et al.[126].

0.5 mL TOP and 60 mg Se are left in a nitrogen filled glovebox in an open glass vial over night at 120 °C to dissolve the Se.

60 mg CdO, 280 mg n-octadecylphosphonic acid (ODPA, ABCR GmbH, 97 %), 3 g TOPO and 1 mL TOP are filled into a 50 mL 3-neck-flask. The mixture is then degassed at 150 °C for 1 h. Under nitrogen, the mixture is heated to 320 °C until a clear solution is formed. After adding 1 mL TOP, the temperature is raised to 380 °C, where 0.5 mL of the TOPSe solution is added and a color change can be observed. The heating mantle is removed after 5 min and the reaction mixture is allowed to cool down to room temperature.

10 mL of ethanol are added and the particle solution is centrifuged at 4000 rpm for 10 min. The precipitate is redispersed in 2 mL toluene. The particles are again

precipitated with acetone and redispersed in 2 mL hexane. This step is repeated once more with ethanol and again with acetone as precipitating agent. Then the particles are dried under vacuum and redispersed in 3 mL hexane.

9.2.6.2 Characterization

A spectrum is taken from a diluted QD solution in hexane. Additionally, SEM measurements are performed to assess the size distribution and appearance of the QDs.

The size of the QDs is determined via measuring the particles from the SEM micrograph with ImageJ software. A value of 4.0 ± 0.6 nm is found with this method.

When using the empirical formula found by Yu et al.[125] (**Equation 28**), a value of 4.1 nm is calculated which is in good agreement with the measured value.

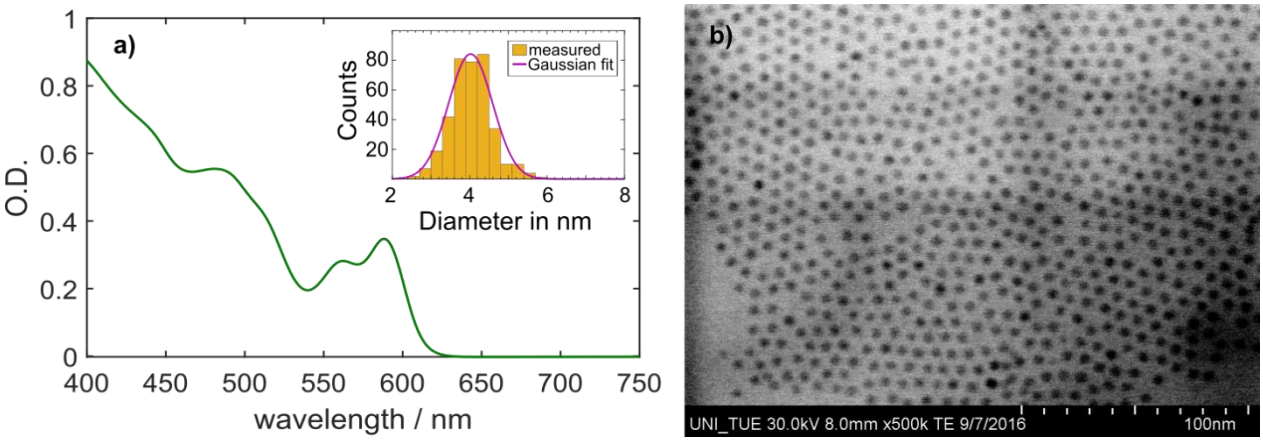

Figure 25: Characterization of the TOP capped CdSe QDs by UV-NIR spectroscopy and SEM. a) Spectrum of CdSe QDs in hexane. The peak at 588 nm is the first excitonic transition. The inset shows the size distribution of the QDs as analyzed from the SEM micrograph with the ImageJ software. b) An SEM micrograph of the CdSe QDs with TOP as ligand.

9.2.7 Synthesis and Characterization of CdSe QDs with OA Ligands

This synthesis is performed by Björn Märker.

9.2.7.1 Synthesis

The synthesis of zinkblende structure CdSe QDs with OA ligands follows a modified procedure from several sources[127-129].

22.5 mg CdO, 80 mg myristic acid and 5 mL degassed ODE are filled in a 50 mL three-neck flask and heated up to 100 °C for 10 minutes. When the mixture gets clear, it is heated up to 240 °C and kept there for 5 minutes. The mixture is then allowed to cool

down to 60 °C. Afterwards, 12 mL ODE, 1 mL degassed methanol and 4 mg Cd-acetate is added to the reaction mixture and degassed for 1 h at 90 °C.

19 mg SeO_2 is added to the mixture, which is then degassed for 15 minutes at 60 °C. After filling the flask with nitrogen again, it is heated up to 250 °C at a rate of 10 °C/min. 2 mL ODE and 1 mL OA is injected here while maintaining the temperature. It is kept at this temperature for 60 minutes. The mixture is allowed to cool to 100 °C where 20 mL of toluene are added and then allowed to cool to room temperature.

40 mL acetone is added and the precipitate is removed by centrifuging for 10 min at 4000 rpm. 100 mL methanol is then added and the supernatent is discarded. The particles are redispersed in 20 mL toluene and precipitated again with 20 mL methanol. The precipitate is redispersed in 14 mL dicloromethane from where it is precipitated with 14 mL ethanol. This is repeated for three more times. Then 7 mL acetone is added to the precipitate and shortly sonicated before centrifuging (12000 rpm, 5 min) and removing the supernatant. This step is repeated four times, then the precipitate is dried under vacuum and redispersed in 3-4 mL hexane.

9.2.7.2 Characterization

A spectrum is taken from a diluted QD solution in hexane. Additionally, SEM is measured to assess the size distribution and appearance of the QDs.

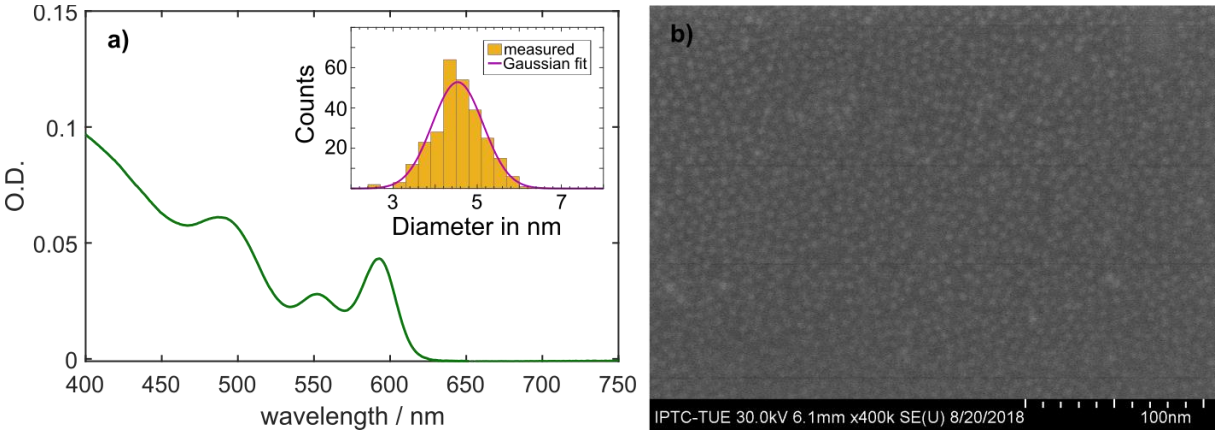

Figure 26: Characterization of the OA capped CdSe QDs by UV-NIR spectroscopy and SEM.
a) Spectrum of CdSe QDs in hexane. The peak at 593 nm is the first excitonic transition. The inset shows the size distribution of the QDs as analyzed from the SEM micrograph with the ImageJ software. b) An SEM micrograph of the CdSe QDs with OA as ligand.

The size of the QDs is determined via measuring the particles from the SEM micrograph with ImageJ software. A value of 4.5 ± 0.6 nm is found with this method.

When using the empirical formula found by Yu et al.[125] (**Equation 28**), a value of 4.3 nm is calculated which is in good agreement with the measured value.

10Experimental Part

Unless otherwise stated, all experiments in this section are performed by me.

10.1Tuning Conductivity and Plasmon Resonance of $Cu_{1.1}S$ Nanoplatelets

10.1.1 Introduction

Since Zhao et al. discovered in 2009[130] that the optical absorption feature in the NIR on copper sulfide QDs can be interpreted as a LSPR, research interest in this class of materials rapidly increased[131-133]. A comprehensive review on this type of semiconductor QDs is published by Kriegel et al in 2017[76]. LSPRs are usually observed only for noble metal QDs like gold[134-138] and are quite uncommon for semiconductor QDs.

It is caused by vacancies in the structure that create free carriers in the material. In fully reduced $Cu_{2-x}S$ QDs (x = 0.00), the CB is almost fully unoccupied and the VB almost fully occupied (full occupation would be only reached at 0 K). This leaves few free charge carriers to interact with incident light which would otherwise lead to the oscillation of those charge carriers. Therefore, the LSPR is orders of magnitude lower than in metal QDs. Also, the number of free charge carriers contributing to conductance is very low, making Cu_2S less conductive than $Cu_{1.1}S$, which shows metallic behavior. Upon oxidation, electrons are extracted from the VB creating free holes that contribute to both, forming an LSPR and making the material conductive[76]. This phenomenon is initially investigated by oxidizing and reducing the particles chemically[72, 119, 130, 139].

It can be assumed that films of $Cu_{1.1}S$ QDs show a similar behavior when being reduced and oxidized electrochemically.

In the work described in the following chapter, two kinds of $Cu_{1.1}S$ films are prepared. One with the native OLA ligands and one by interlinking the QDs with CuPc. The extended pi-system of this linker as well as HOMO and LUMO levels in proximity to the QD VB and CB edges[140] have the ability to facilitate charge carrier transfer from one QD to the other through electronic coupling. The influence of this linker molecule on the conductive properties of $Cu_{1.1}S$ films has to the best of my knowledge not been studied before.

Houtepen and Lesnyak[88, 141] did some work on the electrochemical characterization of $Cu_{1.1}S$ films, but did not investigate potentials more reductive than -1.2 V, maybe to avoid the indium in their ITO substrates from reducing and forming a mirror, making optical experiments impossible[142-144]. I find however that the more reductive potentials reveal a number of interesting properties in $Cu_{1.1}S$ QD films.

10.1.2 Experimental

Before applying a QD film, the interdigitated electrode (IDE) is rinsed with acetone and allowed to dry in air. No ultrasonic bath can be used here because it would damage the electrode.

To fabricate the COIN films used in this study, a clean IDE is transferred into a nitrogen filled glovebox where it is dipped for 30 seconds into a solution of $Cu_{1.1}S$ QDs in hexane. After letting the solvent evaporate, it is dipped into a saturated solution of CuPc in dimethylsulfoxide (DMSO, Acros Organics, Extra Dry, 99.7+ %) for 30 seconds. It is then dipped into pure DMSO for 60 seconds to wash off any access linkers. As DMSO has a high boiling point (180 °C, CAS 67-68-5), the substrate is placed on a hotplate (100 °C) to evaporate excess DMSO. This procedure is repeated 20 times.

The samples with $Cu_{1.1}S$ and their native ligands are prepared by dropcasting a solution of $Cu_{1.1}S$ QDs in hexane onto a clean IDE (ca. 10 µL), letting the solvent evaporate and placing the substrate in DMSO overnight to get rid of excess ligands. The GC electrode for DPV measurements is prepared by dropcasting a solution of $Cu_{1.1}S$ QDs in hexane onto the electrode (ca. 10 µL) and letting the solvent evaporate. These procedures are carried out inside a nitrogen filled glovebox.

Both DPV and CV measurements are carried out inside a nitrogen-purged glovebox using a platinum CE and a silver wire pseudo RE which is calibrated against the ferrocene/ferrocenium couple. All electrochemical experiments in this study are carried out with tetrabutylammonium hexafluorophosphate (TBAHFP) (0.1 M) in acetone. An IDE WE is used for CV, ECG and kinetic steady-state conductance experiments because it is difficult to apply an interlinked film to a GC electrode. DPV experiments are only carried out with dropcasted QD films with their native ligands on a GC electrode while CV measurements are performed on both films.

For the chemical reduction, a solution of copper(I) hexafluorophosphate (CuHFP, 2.5 M in methanol), is added to the acetone/TBAHFP electrolyte solution in the electrochemical cell. Chemical oxidation is achieved by leaving the sample under air.

Optical measurements are performed on a Varian Cary 5000 spectrophotometer. To this end, a baseline with the uncoated IDE is recorded and the sample is measured before and after the redox reaction. To avoid contact with air, the sample is placed inside a quartz cuvette, which is sealed inside the glovebox (**Figure 29b**).

10.1.3 Results

In this study, $Cu_{1.1}S$ QDs are used both with their native ligand OLA and the multidentate semiconductor linker CuPc.

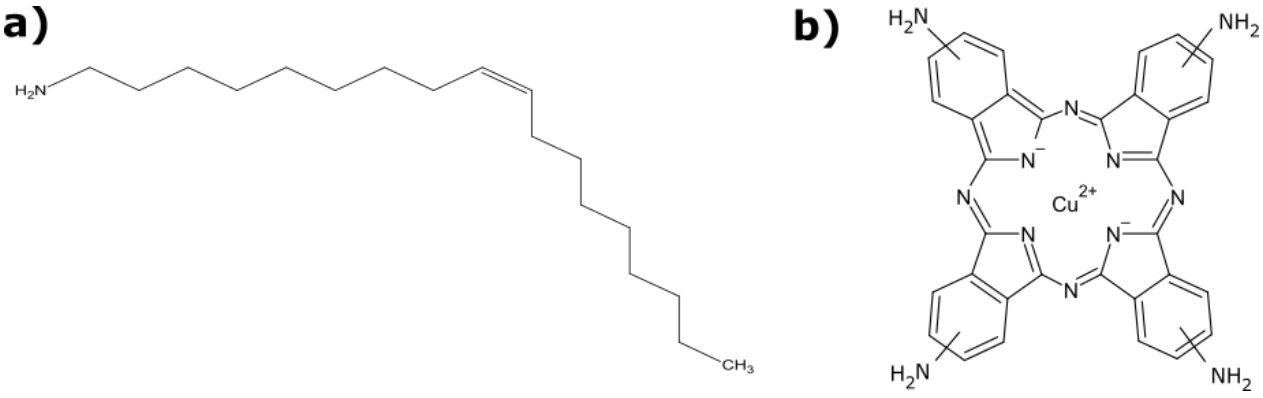

Figure 27: Structural formula of the ligands used in this study: a) OLA and b) CuPc.

No differences in the CV scans between the films with native ligands and those interlinked with CuPc can be observed.

In DPV experiments, there is a strong oxidation peak at 0.31 V vs. Fc/Fc^+ (**Figure 28a**). In CV experiments, a peak at -0.11 V vs. Fc/Fc^+ with a considerable peak spacing of 330 mV can be observed (**Figure 28b**).

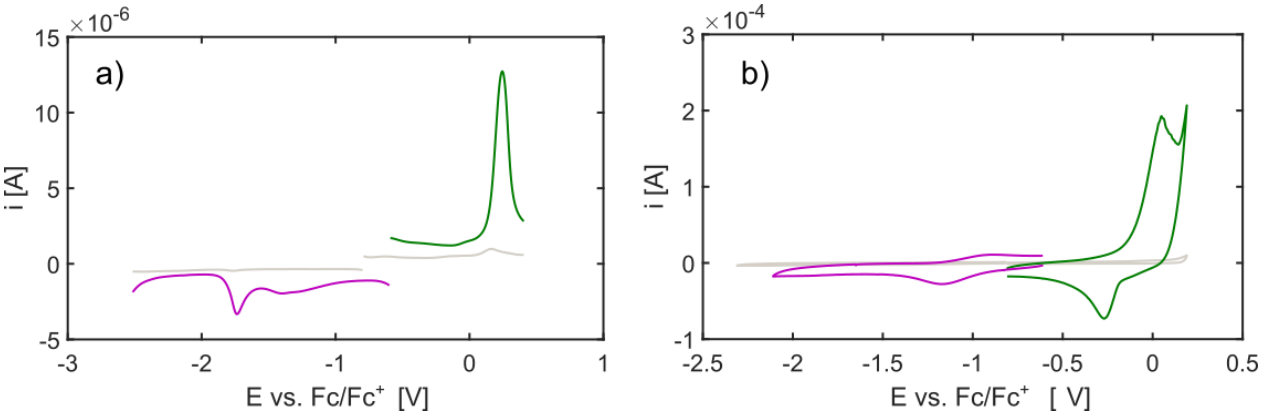

Figure 28: Electrochemical characterization of the $Cu_{1.1}S$ QDs by DPV and CV.
a) DPV measurement of $Cu_{1.1}S$ QDs immobilized on a GC electrode. b) CV measurements of $Cu_{1.1}S$ QDs immobilized on an IDE. Grey lines are background scans.

There is a sharp reduction peak at -1.75 V vs. Fc/Fc^+ in the DPV scans (**Figure 28b**) which cannot be observed in CV measurements. DPV measurements also show a broad peak at around -1.4 V vs. Fc/Fc^+ whereas in CV a peak at -1.0 V vs. Fc/Fc^+ can be observed (**Figure 28a**).

The intensity of the LSPR and the film conductance are measured upon chemical and electrochemical reduction and oxidation of the QD film.

10.1.3.1 Chemical Reduction and Oxidation

No conclusive optical data can be obtained from the films with native ligands. The film interlinked with CuPc can be reversibly reduced and oxidized as shown in **Figure 29a**. A spectrum of the as synthesized film is recorded (dark blue curve) and CuHFP solution is added to the 2.5 mL of electrolyte solution in the electrochemical cell.

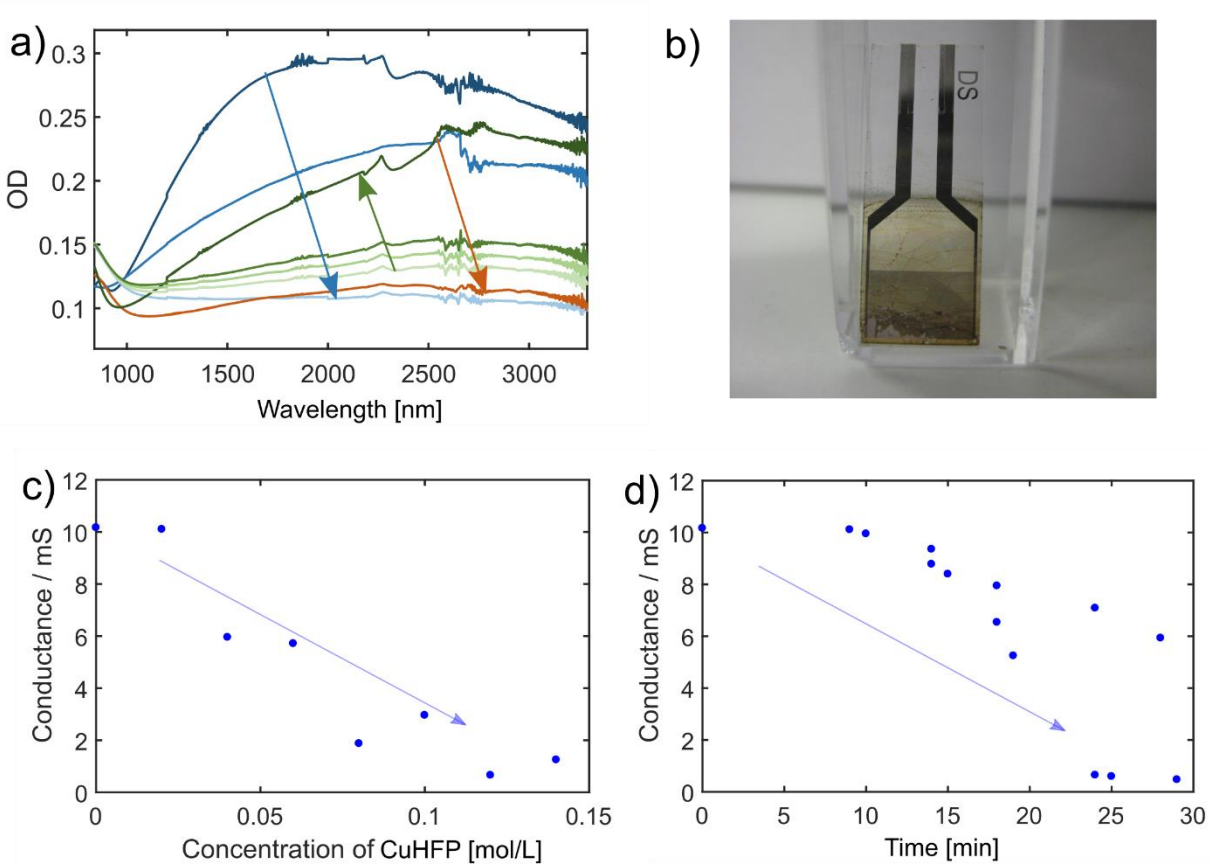

Figure 29: Chemical reduction and oxidation of COIN films based on $Cu_{1.1}S$ nanoplatelets and CuPc. a) Spectra recorded for the $Cu_{1.1}S$ film interlinked with CuPc at various oxidation stages. The blue graphs with the blue arrow show the decrease of the LSPR during the first reduction cycle. The green graphs with the green arrow show the increase of the LSPR upon storing the sample under air and the brown graph with the brown arrow shows the decrease of the LSPR during the second reduction cycle. b) COIN film on IDE placed inside an airtight quartz cuvette. c) Film conductance upon adding increasing amounts of CuHFP solution to the electrolyte. d) Development of film conductance over time in a solution CuHFP (20 µM) in Acetone/TBAHFP as the electrolyte.

Another spectrum is recorded after adding 60 µL (medium blue curve) and 120 µL (light blue curves, **Figure 29a**) of reduction agent. It can be observed that the LSPR vanishes completely. The steady-state conductance is monitored during this procedure by

keeping one of the two WEs at the OCP and cycling the potential of the other WE around the OCP by ± 10 mV. The slope of the current vs. the potential (average of ten cycles) is calculated as a measure of the steady-state conductance and is plotted against the concentration of reduction agent in the electrolyte solution in **Figure 29c**. It can be observed that the conductance decreases with increasing concentration of CuHFP.

In **Figure 29d**, 20 µL of CuHFP are added to the electrolyte solution and the conductance measurement is repeated after a number of waiting times. It can be seen that the effect of the reduction agent is not immediate but takes some time to fully reduce the sample.

After fully reducing the sample, the cuvette is opened and spectra are taken after 90, 180 and 270 minutes as well as after five days in which the sample is in contact with oxygen from the air (light to dark green curves in **Figure 29a**). An increase of the LSPR can be observed. The conductance of the sample also increases back to initial levels.

Subsequently, the sample is again reduced by adding CuHFP to the electrolyte solution and the LSPR again decreases (green to brown curve after the addition of 20 µL of CuHFP solution). The conductance also decreases.

10.1.3.2 Electrochemical Reduction and Oxidation

To find out more about how electrochemical reduction and oxidation influences the conductance, ECG measurements are performed on a film of $Cu_{1.1}S$ nanoplatelets with their native OLA ligands and a film interlinked with CuPc. The films are prepared on IDEs as described in **Chapter 10.1.2** and immersed into an electrochemical cell with acetone/TBAHFP as the electrolyte.

The film with OLA is measured in reductive direction first (purple curve in **Figure 30a**) and shows a conductance of roughly 4 mS on the forward scan and no conductance on the backward scan. Cycling the same sample to the oxidative direction (green curve in **Figure 30a**) yields four times higher conductance. Upon cycling the same sample into the reductive direction afterwards (yellow curve in **Figure 30a**), the initial conductance stays higher than in the first cycle. It drops at about -1.5 V vs. Fc/Fc^+ and returns at around -0.7 V.

The film with CuPc is measured in the oxidative direction first (purple curve in **Figure 30b**) and shows a conductance of roughly 12 mS. It keeps this conductance upon cycling in the reductive direction until a potential of -1.7 V vs. Fc/Fc^+ is reached. There, the conductance goes sharply down to zero. At -2.1 V, it returns to initial levels and stays there throughout the backwards scan. Repeating the experiment (yellow curve in **Figure 30b**) results in the conductance not going fully back to initial levels after reduction. A further broadening and flattening of the "peak" can be observed when repeating the experiment a third time (not shown). On average, this experiment can be repeated around three times with the same sample before the data becomes inconclusive and the sample shows signs of visible degradation (darker color).

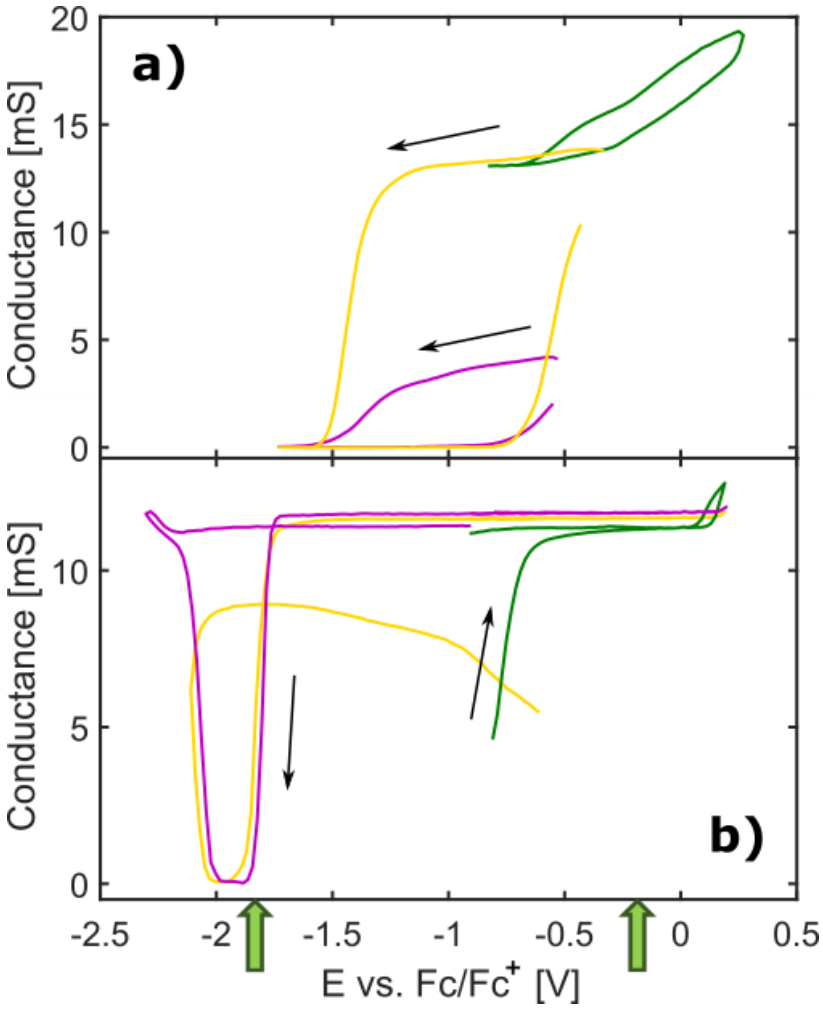

Figure 30: ECG experiments with $Cu_{1.1}S$ QDs.
a) ECG experiments with $Cu_{1.1}S$ QDs their native ligands and b) COIN films based on $Cu_{1.1}S$ QDs and CuPc.

Adding a small quantity (20 µL) of CuHFP to the electrolyte and then cycling to oxidative potentials causes the curve to start at around 5 mS conductance (green curve in **Figure 30b**). Electrochemical oxidation soon overcomes the effect of the chemical reduction and leads to conductances around 12 mS. In the backwards cycle, the conductance stays at that level.

In order to further investigate the kinetics of the electrochemical oxidation and reduction, a steady-state conductance experiment is performed. The two potentials used for this experiment are indicated with green arrows in **Figure 30**.

Contrary to the experiments described in the previous section, the slope of the current is not averaged over 10 cycles for kinetic steady-state conductance measurements. Instead, it is recorded for each cycle separately and assigned to the timestamp of the experiment.

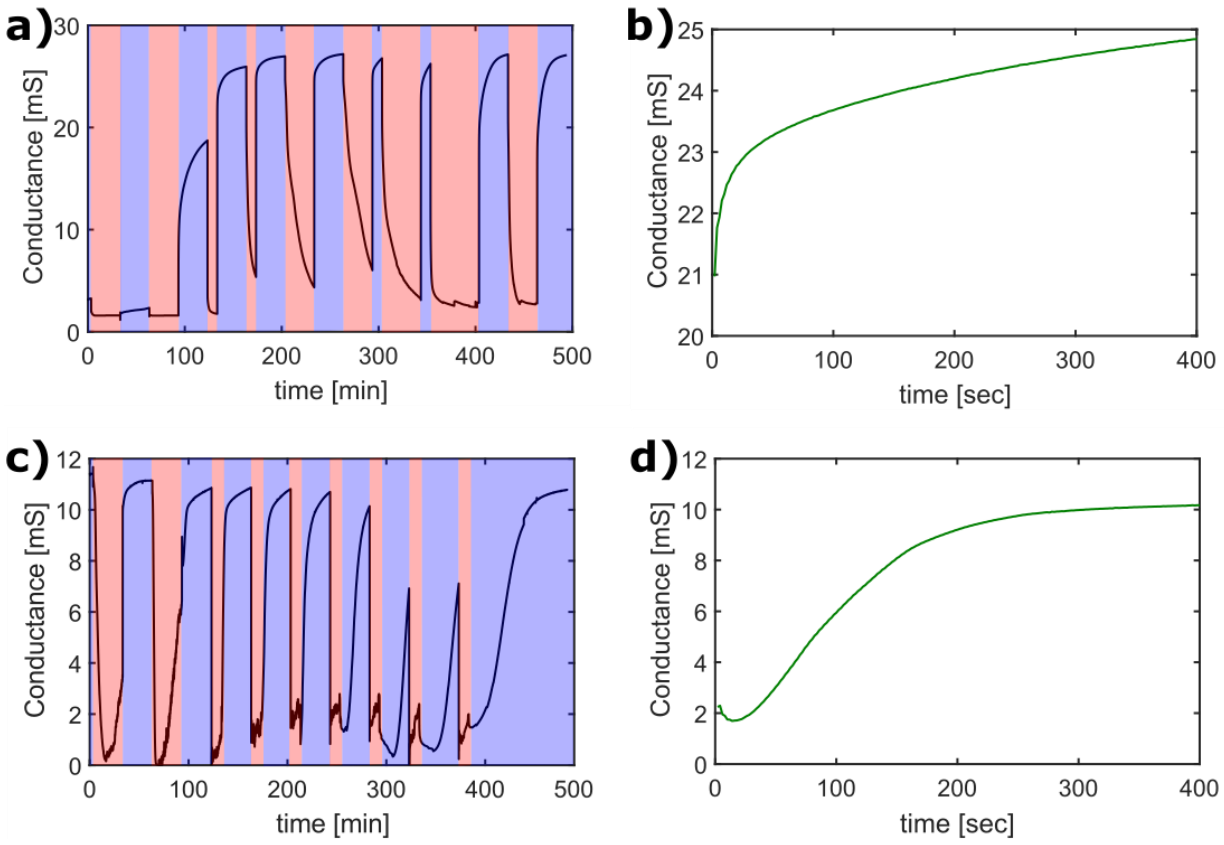

Figure 31: Kinetic steady-state conductance experiments on films of $Cu_{1.1}S$ nanoplatelets. Steady-state conductance of QD films is plotted as a function of time. **Upper row:** $Cu_{1.1}S$ particles with their native ligands. **Bottom row:** $Cu_{1.1}S$ particles interlinked with CuPc. The curves on the right are a magnification of the third oxidation cycle from the graphs on the left. In the graphs on the left, areas shaded in red mark the reduction of the sample with a potential of -1.77 V vs. Fc/Fc^+, areas shaded in blue mark the reduction of the sample with a potential of -0.27 V vs. Fc/Fc^+.

The source electrode is polarized with either -1.77 V vs. Fc/Fc^+ (**Figure 31a+c**, areas shaded in red) or -0.27 V vs. Fc/Fc^+ (**Figure 31a+c**, areas shaded in blue). The graph in the top row (**Figure 31a**) is taken from a film of $Cu_{1.1}S$ QDs with OLA as the ligand. The graph on the right (**Figure 31b**) is a magnification of the third oxidation cycle. It can be observed that during the first two reduction and oxidation cycles, the conductance does not change significantly. After that, applying a more oxidative potential causes the conductance to increase and applying a more reductive potential causes it to decrease. The increase of conductance from ca. 3 mS to 21 mS upon applying the more oxidative potential is instantaneous. The further increase to ~ 25 mS develops over the course of several minutes.

The graph in the bottom row (**Figure 31c**) is taken from a film of $Cu_{1.1}S$ QDs with CuPc. The graph on its right (**Figure 31d**) is a magnification of the third oxidation cycle. It can be seen that after reducing the sample and allowing the conductance to decrease, it takes about 40 seconds for the conductance to start rising again when the more positive potential is applied. This time lapse can be observed to increase over the course of the experiment. It can also be observed that upon applying the highly reductive potential

(areas shaded in red), the conductance drops first, but starts to increase again after about 15 minutes. It reaches almost the initial level after another 15 minutes.

10.1.4 Discussion

The VB is reported to be located at 0.29 V vs. Fc/Fc^+ in the literature for the fully reduced Cu_2S and at 0.22 V for $Cu_{1.1}S$[145]. (These values are reported here under the assumption that the Ag/AgCl reference used in this paper is 0.2 eV over the potential of the NHE and the potential of the NHE is -4.6 eV under the potential of the absolute vacuum scale. Bearing in mind that the potential of Fc/Fc^+ is assumed as being placed 4.8 eV under the potential of the absolute vacuum scale, that means in this case the values reported in the literature vs. Ag/AgCl are comparable to the same values reported vs. the Fc/Fc^+ scale).

The value for the VB measured in this work by DPV is 0.31 V vs. Fc/Fc^+. This value is comparable to those in the literature, however it is closer to the one for the fully reduced Cu_2S. It is unlikely that the as-synthesized QDs are very much reduced because they exhibit a considerable LSPR which is a sign for highly oxidized QDs (**Chapter 9.2.2.2**). It is however possible that the conversion of the two different measurement scales and the use of different solvents leads to slightly different results.

The value for the VB edge measured by CV (-0.11 V vs. Fc/Fc^+) is more far away from that. This measurement also shows a spacing of 330 mV between the reduction and oxidation peak so that it is not fully clear whether they actually belong together. The oxidation peak is at 0.05 V vs. Fc/Fc^+ and therefore much closer to the literature value.

In the following, the DPV value of 0.31 V vs. Fc/Fc^+ is assumed to be the potential of the VB edge for the as synthesized QDs used in this study.

When investigating the position of the CB, CV measurements show a peak at around -1.0 V vs. Fc/Fc^+ while DPV measurements show two peaks: a broad one at around -1.4 V and a sharp one at -1.75 V. Assuming the -1.0 V of the CV measurement as the CB edge would mean the $Cu_{2-x}S$ QDs have a band gap of 1.28 eV which corresponds to the quite far reduced form $Cu_{1.94}S$[77] and is therefore unlikely. Assuming the sharp peak at -1.75 V vs. Fc/Fc^+ from the DPV measurement to be the CB edge, would make the band gap 2.0 eV wide. That would correspond to the fully oxidized form (CuS)[88]. The as synthesized QDs are assumed to have a $Cu_{1.1}S$ stoichiometry because this composition builds a stable metallic phase[118]. A band gap of 2.0 eV would also match this form since CuS is only slightly more oxidized than $Cu_{1.1}S$. It is therefore assumed that the CB is located at -1.75 V vs. Fc/Fc^+ and that the broad peak at -1.4 V in the DPV corresponds to the peak at -1.0 V in the CV and can be explained as defect states in the material.

As stated in the results section (**Chapter 10.1.3**), the CV scans for the films with OLA and CuPc do not differ noticeably. This could be due to either the ligand not being properly exchanged or the ligand not interacting electronically with the QDs.

It is unlikely that the ligands are not exchanged because if that were the case the QDs would detach from the electrode during the dipcoating procedure. The tetravalent linker molecules stabilize the film and an immersion into hexane does not lead to a detachment of the film. So it can be said that ligand exchange might not be quantitative, but it did happen to a sufficient extent.

The HOMO of CuPc is reported to be in the region of -5 eV vs. absolute vacuum scale, the LUMO is reported to be around -3.2 eV[140]. Referenced against ferrocene, this places the HOMO at 0.2 V and the LUMO at -1.6 V vs. Fc/Fc^+. That means the HOMO is roughly 100 mV away from the assumed location of the VB of the QDs. The LUMO of CuPc is also roughly 100 mV away from the assumed location of the CB. That would theoretically allow for an electronic overlap of both the LUMO of CuPc with the CB of the $Cu_{1.1}S$ QDs and the HOMO of CuPc with the VB of the $Cu_{1.1}S$ QDs. An energetic similarity of electronic levels does however not automatically mean a good electronic coupling. This might be the case with $Cu_{1.1}S$ QDs and CuPc.

When chemically reducing and oxidizing the QD film with native ligands, the changes in absorption are so minor, if they show at all, that these results are not shown here. There are several reasons for these experiments not leading to comparable results vs. the films interlinked with CuPc.

The first point is that the interlinked films are built up of several layers of QDs and are therefore much thicker than the film with native ligands. These are fabricated by a dropcasting procedure with only one layer (see **Chapter 10.1.2**). The absorption of the LSPR measured in the spectrophotometer is therefore already much lower and a further decrease by reducing the sample is hard to detect.

Secondly, OLA is a monovalent ligand that does not chemically interlink the particles. The film is therefore much less mechanically stable than the one interlinked with tetravalent CuPc ligands. The addition, CuHFP or electrochemical treatments damage the (already thinner) film with native ligands more than the thicker and more mechanically stable interlinked film.

The results obtained by chemically reducing and oxidizing the interlinked COIN film are fully in line with literature[146]. Conductance and LSPR absorption go down upon reduction and come back upon oxidation. The observation that these changes occur over time rather than immediately has also been observed before[146].

ECG data of the films with native ligands shows the expected behavior of high conductance when the film is oxidized (green curve in **Figure 30a**), loss of this conductance at a certain potential when cycled in the reductive direction and regaining

of conductance upon cycling back to more oxidative potentials (yellow curve in **Figure 30a**). A few additional observations are however worth mentioning here:

The potential at which the conductance goes down, is at around -1.4 V and not at the assumed CB edge at -1.75 V vs. Fc/Fc^+. It may be that the trap states observed in DPV at -1.4 V vs. Fc/Fc^+ contribute to film conductance and their complete filling reduces the film conductance.

It is also observed that the initial reductive scan (purple curve in **Figure 30a**) stays at lower conductances than the later recorded yellow curve. This build-up of conductance is observed with this type of QD film in several experiments. In **Figure 31a**, it can be seen that polarizing the film alternatingly with a more and a less reductive potential does not lead to significant changes in conductance for the first two cycles. It is believed that the electrochemical experiment damages the surface of the QDs and thereby introduces additional states below the CB that contribute to conductance. That may sound counterintuitive to the concept that trap states decrease film conductance (**Chapter 7.1**), but $Cu_{1.1}S$ QDs with their metallic properties are likely to behave differently.

The films interlinked with CuPc show a quite different behavior (**Figure 30b**). They are conductive under oxidative conditions and stay conductive upon reduction up to a potential of about -1.7 V vs. Fc/Fc^+. This potential corresponds to the CB of the QDs. Further reduction leads to a sharp decrease of the conductance. At around -2.1 V, the conductance shows a similarly sharp increase and stays at that level on the backwards sweep towards more positive potentials. This rather unexpected observation is closely connected to what can be seen in the kinetic steady-state conductance experiment (**Figure 31c**). In this measurement, the film conductance decreases when a potential of -1.77 V vs. Fc/Fc^+ is applied to the WE. After 15 minutes the conductance starts to rise again, reaching almost initial levels after another 15 minutes. In the ECG experiment, it takes 6 minutes to go from the onset of the conductance decrease at -1.77 V to the onset of the conductance increase at -2.1 V. Taking into account that the time-dependent measurements are carried out at a constant potential of -1.77 V, the time span for conductance to come back in ECG measurements could be decreased at the more negative potentials close to -2 V.

On the backward scan (towards higher potentials) the conductance stays high. This can be explained with the time lapse between the start of applying a more oxidative potential to the film and the conductance increasing (as shown in **Figure 31d**). When the film finally reaches potentials high enough to induce conductive behavior due to oxidizing the film, the conductance is still high from the effect that causes it to increase at reductive potentials.

10.1.5 Conclusion

The $Cu_{1.1}S$ frontier orbitals are successfully characterized electrochemically. It can be shown that $Cu_{1.1}S$ films with their native ligands exhibit different conduction properties as compared to $Cu_{1.1}S$ based COIN films interlinked with CuPc. The former show low conductance at first that rises upon exposing the films to electrochemical stress. The latter show a stable high conductance, not only at oxidative potentials, but also over a wide range of reductive potentials. The conductance drops sharply at a potential of -1.7 V vs. Fc/Fc^+ and starts to rise again to initial values when the sample is exposed to this condition for about 15 min.

Up to now, there is no conclusive explanation on why this increase of conductance happens. One way to explain it is that Cu^+ gets reduced to Cu^0 which is metallic and therefore highly conductive. To verify this, XPS experiments with the reduced film and the as-prepared film have to be conducted.

10.2 Investigating the Influence of Linker Molecules on the Electronic Structure of PbS and CdSe QDs

10.2.1 Introduction

Electrochemistry is a good way to probe the quantum confined electronic states of QDs, as well as their surface trap states, but there are differences in the various electrochemical techniques and their ability to probe QDs.

The most commonly used technique, CV, is a very good technique when it comes to evaluating diffusion constants of a dissolved analyte and make observations about the reversibility of a redox reaction[147]. For QDs however, it is not a very good choice since they usually do not show a return peak and therefore the calculation of the half-wave potential is impossible. DPV is used in this chapter to determine electronic states of QDs. Its better suitability to probe electronic states in QDs is also reported in a number of publications[58, 85, 147, 148].

One of the big challenges of investigating the energy levels of semiconductor QDs is the unambiguous measurement of the CB and VB. The band edges are difficult to differentiate from trap states or states originating from the linker molecules when only looking at CV or DPV data. Spectroscopic techniques like EMAS are used to unambiguously detect the CB edge[109].

In **Chapter 10.2.3**, three sizes of PbS QDs are chosen (12, 6.5 and 4.8 nm in diameter) and investigated electrochemically with CV and DPV. A sample of QDs comparable to the medium size PbS QDs is then interlinked with amino functionalized metal phthalocyanine (MePc) ligands and the effect of those ligands on the electronic structure of the QDs is investigated. The following ligands are used: ZnPc, NiPc, CoPc, FePc, CuPc and H_2Pc.

In **Chapter 10.2.4**, the same is done for CdSe QDs. Here, two different synthetic strategies with different native ligands (OA and TOP) are compared first. These particles are of comparable size (4.1 and 4.3 nm in diameter).

CdSe particles are then interlinked with the same MePc ligands as in **Chapter 10.2.3**. This requires the use of a third synthetic strategy of CdSe particles as the native OA and TOP ligands have a higher affinity to the QDs than the MePc ligands and cannot be easily exchanged. The surface of this batch of CdSe particles is therefore functionalized with BA ligands first and the ligand exchange with the MePc ligands is verified by Raman spectroscopy.

The aim of these studies is to investigate the influence of the ligands on the position of the band edges of the QDs. Also, the effect of ligand exchange on trap states in the QD material should be assessed. The DPV experiments are conducted in two different electrolytes (methanol (MeOH) and acetonitrile (MeCN)) to increase the robustness of the data and investigate the magnitude of solvent effects.

To the best of my knowledge, the influence of phthalocyanine linkers on the position of CdSe frontier orbitals has not been investigated before. These systems are however very interesting because of the close proximity of the phthalocyanine HOMO and LUMO orbitals to the CB and VB of the QDs and the potential of those materials to show electronic coupling.

10.2.2 Experimental

The batch of large PbS QDs (12 nm) is synthesized with lead oxide as precursor (see **Chapter 9.2.4**). The other two batches (6.5 and 4.8 nm) are synthesized with lead chloride as precursor (see **Chapter 9.2.3**) and the difference in size is achieved by varying the reaction time.

A batch of 4.1 nm CdSe QDs is synthesized with TOP as native ligand (see **Chapter 9.2.6**). Another batch of 4.3 nm CdSe QDs is synthesized with OA as native ligand (see **Chapter 9.2.7**). The CdSe QDs for the preparation of the COIN films are synthesized after the procedure described in **Chapter 9.2.5**.

FTO substrates are rinsed with deionized water, then cleaned in an ultrasonic bath: first with acetone for 5 minutes, then with a mixture of 10 % Extran® (Merck) in deionized water for 10 minutes, then with deionized water for 5 minutes. The wet substrates are dried under air. To remove all remaining organic impurities on the substrate, they are treated in a UV-Ozone cleaner for 10 minutes and then inserted into a nitrogen filled glovebox.

The surface of the FTO substrates is functionalized with MPTMS to improve the binding affinity of QDs to the substrate surface[149] (**Figure 32**). Therefore, the clean FTO substrate is immersed in 6 mL of hexane, and 100 µL of MPTMS (Acros Organics, 85 % technical grade) is added. The solution is kept overnight. Excess MPTMS is subsequently removed by rinsing the substrate with hexane.

The clean and functionalized substrate is dipped for 10 minutes into a solution of QDs in hexane (when using PbS) or chloroform (when using CdSe). After letting the solvent evaporate, it is dipped into a saturated solution of the linker molecule in DMSO for 30 seconds. Then it is dipped into pure DMSO for 60 seconds to wash off any excess linkers. The substrate is then placed on a hotplate (100 °C) to evaporate excess DMSO. The whole procedure is repeated another seven times with the only difference that the substrate is dipped in the QD solution for 30 seconds instead of 10 minutes.

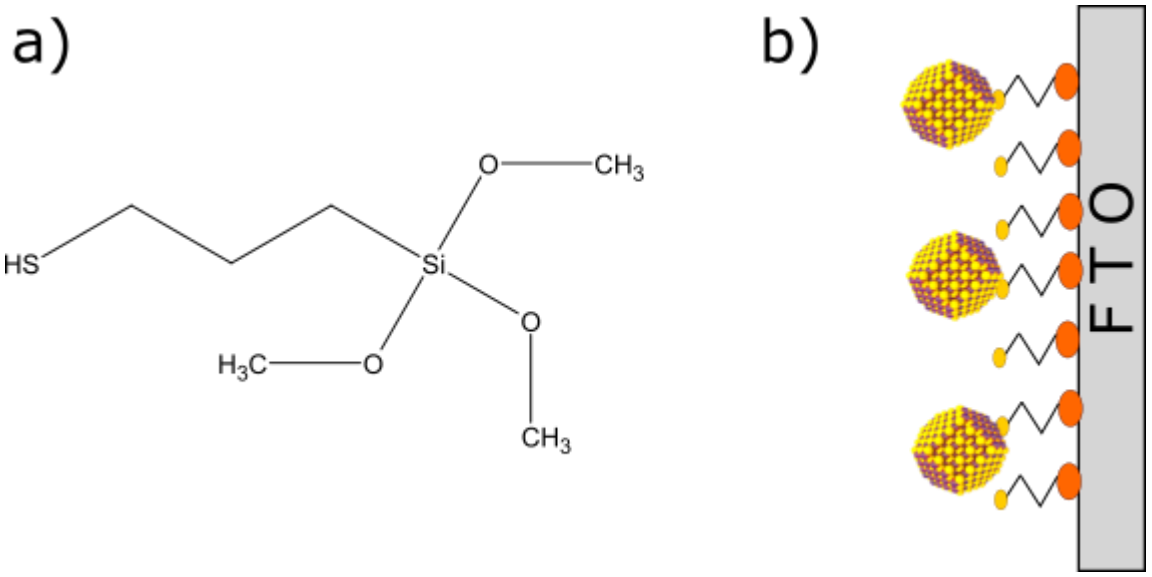

Figure 32: Surface functionalization of the FTO electrode.
a) Structural formula of MPTMS. b) QDs binding to an FTO substrate functionalized with MPTMS.

The samples with the QDs and their native ligands on FTO substrates are prepared by dipping the cleaned and functionalized FTO electrodes into a solution of QDs in hexane (when using PbS) or chloroform (when using CdSe) for 10 minutes and letting the solvent evaporate.

The samples for DPV measurements on the GC electrode are prepared by dropcasting the QD solution (ca. 10 µL) onto the GC electrode and letting the solvent evaporate.

All electrochemical experiments except EMAS are carried out under nitrogen atmosphere with the electrochemical cell placed inside a Faraday cage inside a glovebox. The EMAS experiments are carried out in a home-built, closed but not fully air-tight electrochemical cell under ambient conditions. MeOH/$LiClO_4$ and MeCN/$LiClO_4$ (both 0.1 M) are used as electrolytes for DPV. CV is only performed in MeOH/$LiClO_4$. EMAS is only performed in MeCN/$LiClO_4$. A platinum wire is used as CE and a silver wire is used as pseudo RE which is calibrated against the ferrocene/ferrocenium couple. A GC or FTO electrode is used as WE.

The sample preparation and DPV measurements with the GC electrode as well as the EMAS experiments are performed by me. The sample preparation and DPV measurements with the FTO electrode are performed by Sophia Westendorf. The preparation of the EMAS samples and the Raman measurements are performed by Björn Märker.

10.2.3 Characterization of PbS QDs

10.2.3.1 Results

A CV is recorded for the 6.5 nm PbS QDs in MeOH/$LiClO_4$ at a number of different scanning speeds. In **Figure 33a**, two of them are plotted. The recorded curves change significantly from a scanning speed of 0.1 V/s to 10 V/s. The position of the oxidation peak shifts from 0.4 V vs. Fc/Fc^+ to 0.6 V vs. Fc/Fc^+ and the magnitude changes from $1.01 \cdot 10^{-5}$ A to $6.41 \cdot 10^{-5}$ A. The reduction peak is not visible in the curve recorded at 0.1 V/s. It appears at the higher scan rate at a potential of -1.0 V vs. Fc/Fc^+ and has a magnitude of $-4.69 \cdot 10^{-5}$ A.

A DPV scan with the same batch of QDs, also in in MeOH/$LiClO_4$, (**Figure 33b**, green curve) reveals an oxidation peak at -0.04 V vs. Fc/Fc^+ and a reduction peak at -1.05 V vs. Fc/Fc^+. A smaller reduction peak can be observed at -0.89 V vs. Fc/Fc^+.

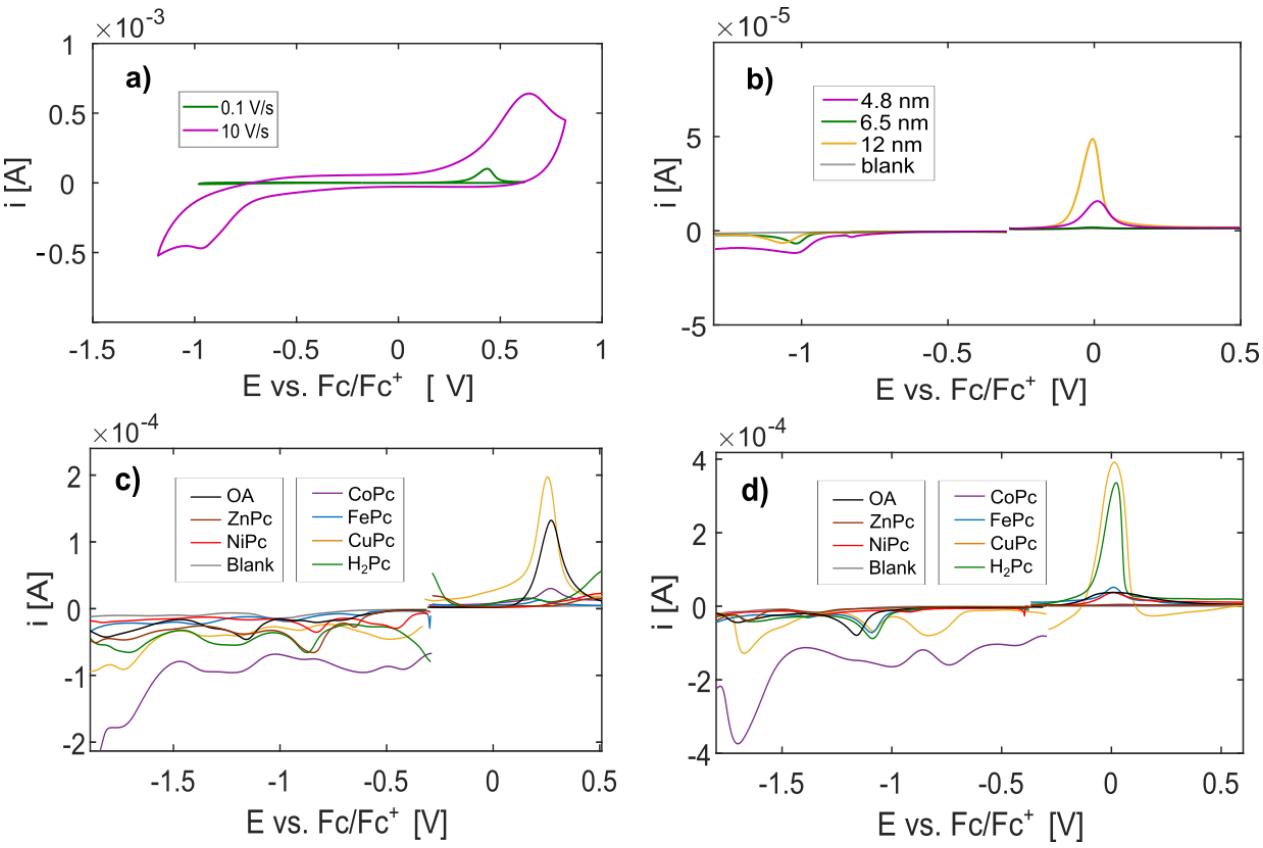

Figure 33: Electrochemical characterization of PbS QDs with their native ligand shell and various MePcs. a) CV measurement of 6.5 nm OA capped PbS QDs in MeOH/$LiClO_4$, measured on the GC WE. b) DPV measurement of the same OA capped PbS QDs in MeOH/$LiClO_4$, measured on the GC WE. c) DPV measurement of PbS QDs interlinked with MePc ligands in MeCN/$LiClO_4$, measured on the FTO WE. d) DPV measurement of PbS QDs interlinked with MePc ligands in MeOH/$LiClO_4$, measured on the FTO WE.

For the batch of large PbS QDs, only two peaks can be observed in DPV measurements: one oxidation and one reduction peak (**Figure 33b**, yellow curve). That holds true for measurements in both electrolytes. The medium large particles have a small additional

peak -0.93 V vs. Fc/Fc^+ only in MeOH, not in MeCN. The small QDs show an additional reduction peak in all measurements.

It can be seen in **Figure 33c+d** that the ligand exchange leads to a number of additional peaks, especially in the reductive scan direction. Overall, the reference sample shows the least amount of peaks, the least states in the band gap and overall the broadest peaks with the lowest intensity. This holds true for measurements in both electrolytes. An exception to this rule is only the oxidation peak of OA capped PbS QDs in $MeCN/LiClO_4$, which is quite pronounced and has a similar shape to what is observed in the experiments on the GC electrode. The COIN films interlinked with CuPc show pronounced oxidation peaks in both electrolyte solutions.

Generally, the distinct oxidation peak is retained in most cases. It can be observed that the measurements conducted in MeCN lead to a shift of the oxidative peak by about 200 mV towards more oxidative potentials as compared to measurements conducted in MeOH. This can also be observed for the measurements with PbS QDs and their native ligands on the GC WE. Reductive peaks are shifted towards higher potentials by about 150 mV when measured in MeCN.

10.2.3.2 Discussion

The observation that the peak positions of PbS QDs measured with CV change so much upon increasing the scanning speed is an indication of impaired electron transfer from the WE to the QD[91]. This is unsurprising as the QDs used in this study are capped with a layer of insulating ligands that hinder charge transfer. It can be hypothesized that even for films interlinked with conductive semiconductor molecules, a similar CV curve would be recorded since their conductive properties are not good enough to enable the transport speeds needed for a CV measurement.

The COIN films are fabricated on an FTO electrode which, in itself, is less conductive than the GC electrode used for the characterization of the QDs with native ligands. This is also the reason for the generally broader DPV peaks in the COIN measurements as compared with the measurements on QDs with their native ligands. The lower intensity of the PbS films with their native ligands on FTO can be attributed to the lower film thickness of this sample. For these films, only a monolayer can be attached to the WE, while the COIN films consist of eight layers.

The absence of return peaks in the CVs indicates that the QDs also undergo chemical reactions as a result of the electrochemical charge transfer. This can be the oxidation or reduction of surface ligands. Also, Pb^{2+} or S^{2-} atoms on the outer layer of the QDs can undergo irreversible redox reactions.

These observations lead to one big challenge when trying to characterize QDs electrochemically by CV: Usually, the half-wave potential of an electron transfer is determined by averaging the oxidative and reductive curve in a CV measurement. If

there is only one of these curves, this calculation is not possible. Just quoting the position of that one curve leads to an increasing inaccuracy the faster the scanning speed is. Going to lower scanning speeds, on the other hand, leads to lower magnitudes of the peaks (see **Chapter 8.1.2**) up to a point where they cannot be observed any more.

With DPV, a very slow scanning speed (0.008 V/s) can be used because the signal to noise ratio is increased by sampling two sets of current data per measurement point and subtracting them from one another (see **Chapter 8.2**). The half-wave potential can then easily be calculated with **Equation 9**.

In this case, the half-wave potential ($E_{1/2}$) is the same as the formal potential of the electrode ($E^{0\prime}$) because both the reduced and the oxidized species of this experiment are attached to the electrode which sets both their diffusion coefficients to 0[90].

$$E_{1/2} = E^{0\prime} + \frac{RT}{nF} ln \frac{\sqrt{D_R}}{\sqrt{D_O}} \tag{29}$$

R is the ideal gas constant, T is the absolute temperature, n is the number of transferred electrons, F is the Faraday constant, D_R is the diffusion coefficient of the reduced species and D_O is the diffusion coefficient of the oxidized species.

It can be observed that the peak positions measured in MeCN/$LiClO_4$ are shifted towards more oxidative potentials by roughly 200 mV as compared to the peak positions measured in MeOH/$LiClO_4$. This can be explained with solvation effects.

MeOH is a polar protic solvent while MeCN is a polar aprotic solvent. It is known that protic solvents can stabilize anions through coordination of the hydrogen atoms while aprotic solvents can stabilize cations through free electron pairs[150]. This way, ClO_4^- ions moving towards the WE during oxidation are better stabilized by MeOH through the formation of hydrogen bonds. The oxidation of the COIN film might then happen at lower potentials because the negative counter charges necessary for QD oxidation are more readily available.

The same might happen for Li^+ ions during reductive processes in MeCN. As they are better stabilized by the free electron pairs of the nitrogen in the aprotic solvent, they might reach the WE sooner and compensate the negative charges being injected into the QD film. These negative charges can then be injected into the film under less reductive conditions.

The following table summarizes the peaks found for the tree batches of QDs measured with their native ligands on the GC WE (OA1 = 4.8 nm QDs, OA2 = 6.5 nm QDs, OA3 = 12 nm QDs) as well as the QDs measured on the FTO WE (OA4 = 6.1 nm QDs used for ligand exchange) with the various MePcs as ligands. The peaks are grouped based on their position, intensity and shape. The peaks highlighted in green (CB) and blue (VB)

are assumed to be the band edge positions and are used for the calculations summarized in **Table 1**. The peaks highlighted in yellow are assumed to originate from the $2e_g$ orbitals in the MePcs.

Table 1: Summary of peak potentials measured for PbS QDs in MeCN/$LiClO_4$ and MeOH/$LiClO_4$. Values highlighted in yellow are assumed to result from the MePc LUMO, values highlighted in green are assumed to result from the QD CB and values highlighted in blue are assumed to result from the QD VB.

	Ligand	Peak Potentials [V vs. Fc/Fc⁺]										
MeCN/$LiClO_4$	OA1					-0.89			-0.65		0.25	
	OA2					-0.91					0.22	
	OA3					-0.84					0.18	
	OA4	-1.85		-1.33	-1.19	-0.96	-0.85	-0.75	-0.59		0.24	
	ZnPc	-1.90	-1.76	-1.52	-1.19	-0.87		-0.68		-0.29	0.15	0.48
	NiPc	-1.86	-1.76	-1.56	-1.18	-0.86			-0.58	-0.49	0.29	0.47
	CoPc	-1.91	-1.79	-1.36	-1.21	-0.92	-0.64	-0.45	-0.16	0.12	0.24	
	FePc		-1.63	-1.42		-1.00			-0.64		0.19	0.33
	CuPc	-1.90	-1.76	-1.36	-1.22	-0.94	-0.52			-0.22	0.23	
	H_2Pc	-1.87	-1.74		-1.24	-0.90			-0.60		0.13	0.51
MeOH/$LiClO_4$	OA1				-1.05		-0.88				-0.02	
	OA2				-1.05		-0.89				-0.04	
	OA3				-1.10						-0.04	
	OA4		-1.73	-1.53	-1.19	-1.02		-0.60			-0.02	
	ZnPc	-1.84	-1.68	-1.37	-0.98						0.02	
	NiPc	-1.91	-1.68	-1.37	-0.94			-0.43			-0.02	0.32
	CoPc	-1.92	-1.73	-1.21	-1.02		-0.77	-0.47			-0.01	
	FePc		-1.57	-1.42	-1.12	-0.40				-0.21	-0.02	0.16
	CuPc		-1.70	-1.55	-1.11		-0.86	-0.58			-0.02	0.32
	H_2Pc		-1.67	-1.45	-1.12						0.00	

The proposed band edge positions of the PbS QDs and PbS based COIN films are in line with those reported in the literature[60]. When they are used to calculate the electronic transport band gap $E_{g,el}$ (as done in **Table 2**), $E_{g,el}$ is bigger than the optical band gap $E_{g,opt}$ which is in line with the result expected from **Equation 4**.

The peak at -0.65 V vs. Fc/Fc⁺ for the 4.8 nm PbS QDs measured in MeCN is most likely a trap state. The same applies to the peak at -0.88 V vs. Fc/Fc⁺ for the 4.8 nm PbS QDs and at -0.89 V vs. Fc/Fc⁺ for the 6.5 nm PbS QDs measured in MeOH.

There are more trap states measured in MeCN (in the experiments both with OA and MePc ligands) which might be an indication of the trap states being associated with an excess of negatively charged sulfur atoms on the surface, which are better stabilized by MeOH. However, this is in contradiction to earlier findings in literature that the surface of PbS QDs is Pb-rich[121]. To investigate this further, more experiments in a greater variety of solvents are needed.

Table 2: Summary of proposed band potentials and band gap estimates of the PbS based COIN samples. (* Estimated optical band gap based on the UV-Vis-NIR characterization of the QDs with their native ligands.)

Electrolyte	Ligand	CB [V vs. Fc/Fc+]	CB [eV Vac]	VB [V vs. Fc/Fc+]	VB [eV Vac]	$E_{g,el}$ [V]	$E_{g,opt}$ [V]
MeCN/ $LiClO_4$	OA1	-0.89	-3.97	0.25	-5.11	1.14	0.92
	OA2	-0.91	-3.95	0.22	-5.08	1.13	0.77
	OA3	-0.84	-4.02	0.18	-5.04	1.02	0.66
	OA4	-0.96	-3.90	0.24	-5.10	1.20	0.78
	ZnPc	-0.87	-3.99	0.15	-5.01	1.02	0.78*
	NiPc	-0.86	-4.00	0.29	-5.15	1.15	0.78*
	CoPc	-0.92	-3.94	0.24	-5.10	1.16	0.78*
	FePc	-1.00	-3.86	0.19	-5.05	1.19	0.78*
	CuPc	-0.94	-3.92	0.23	-5.09	1.17	0.78*
	H_2Pc	-0.90	-3.96	0.13	-4.99	1.03	0.78*
MeOH/ $LiClO_4$	OA1	-1.05	-3.81	-0.02	-4.84	1.03	0.92
	OA2	-1.05	-3.81	-0.04	-4.82	1.01	0.77
	OA3	-1.10	-3.76	-0.04	-4.82	1.06	0.66
	OA4	-1.19	-3.67	-0.02	-4.84	1.17	0.78
	ZnPc	-0.98	-3.88	0.02	-4.88	1.00	0.78*
	NiPc	-0.94	-3.92	-0.02	-4.84	0.92	0.78*
	CoPc	-0.92	-3.94	-0.01	-4.85	0.91	0.78*
	FePc	-1.12	-3.74	-0.02	-4.84	1.10	0.78*
	CuPc	-1.11	-3.75	-0.02	-4.84	1.09	0.78*
	H_2Pc	-1.12	-3.74	0.00	-4.86	1.12	0.78*

The peaks measured for the COIN films are not as easily assigned as those for the QD films with their native ligands because the peaks expected for the MePc linkers have to be taken into account. A good estimate about orbital energies in MePcs can be given based on the calculations done by Liao et al.[140]. These values are based on the unsubstituted phthalocyanines, while the ones used here have four amino substituents. Thus, care should be taken when interpreting the data. The LUMO of the MePcs has a $2e_g$ symmetry and the HOMO has a a_{1u} symmetry. Their energies based on the work of Liao et al.[140] are summarized in **Table 3**.

Table 3: Theoretical estimates for the orbital energies of MePcs.

MePc Ligand	Orbital Energy Level ($2e_g$) [V vs. Fc/Fc+]	Orbital Energy Level (a_{1u}) [V vs. Fc/Fc+]
ZnPc	-1.75	0.15
NiPc	-1.20	0.15
CoPc	-1.90	0.15
FePc	-1.40	0.20
CuPc	-1.80	0.15

In the PbS based COIN films, the HOMO of the MePcs aligns well with the VB of the QDs. Research in our group suggests that this leads to electronic coupling of the MePc HOMO with the QD VB and enhances hole transport[68]. It is therefore likely that the peaks seen in the DPV scans (values marked in blue in **Table 1**) are a hybrid of QD VB and MePc

HOMO orbitals. That could also explain why, especially in the measurements conducted in MeCN/$LiClO_4$, the position of the oxidation peaks differs by 160 mV from one COIN film to the other (H_2Pc -> 0.13 V vs. Fc/Fc^+, NiPc -> 0.29 V vs. Fc/Fc^+) while the position of the peaks measured for the QDs with their native ligands are quite consistent (0.18 – 0.25 V vs. Fc/Fc^+).

It is also noteworthy that the oxidation peak for the films interlinked with CuPc is quite pronounced and shows a high intensity in both electrolytes. This is also the combination that resulted in the best conductive properties in FET measurements[68]. It can therefore be speculated that the intensity of this peak in DPV measurements is linked to the electronic coupling of the QD 1 S_h orbital with the linker a_{1u} orbital. The increased intensity of the peak can result from the better conductance of this film or a better stabilization of the charge extracted from the coupled orbital.

A number of peaks in the reductive range, above the CB of the QDs, can be assigned to the LUMO of the MePcs (values marked in yellow in **Table 1**). As there is a number of peaks in this region, it is challenging to assign them to any particular orbital. For example, the location of the LUMO of ZnPc is estimated at -1.78 V vs. Fc/Fc^+ which could either be the peak at -1.90 or -1.76 V vs. Fc/Fc^+ for the measurements in MeCN/$LiClO_4$ as well as the peak at -1.84 or -1.68 V vs. Fc/Fc^+ for the measurements in MeOH/$LiClO_4$.

The remaining peaks can be attributed to initial trap states of the QD material, trap states induced during film preparation and states from the MePc linkers.

10.2.3.3 Conclusion

When comparing the results obtained with CV and DPV measurements, it can be concluded that DPV is the more suitable electrochemical method to characterize QDs.

MePcs are suitable ligands to form COIN films with PbS QDs. It is very likely that a new hybrid orbital involving the QD VB and the linker HOMO is formed based on previous research[68] and the presence of only one peak in the DPV scans that is slightly shifted compared to the VB edge peak observed in DPVs of the QDs with their native ligands.

10.2.4 Characterization of CdSe QDs

10.2.4.1 Results

Unlike the PbS particles, CdSe QDs show a larger number of peaks, the most obvious of them being a douplet at around 1 V vs. Fc/Fc^+. For the samples measured in $MeCN/LiClO_4$, the smaller peak appears at slightly lower potentials than the main peak (**Figure 34a**). For the samples measured in $MeOH/LiClO_4$, it is vice versa (**Figure 34b**). The sample with OA capped QDs in $MeCN/LiClO_4$ seems to show only one oxidative peak, but upon zooming in, the other one can be detected.

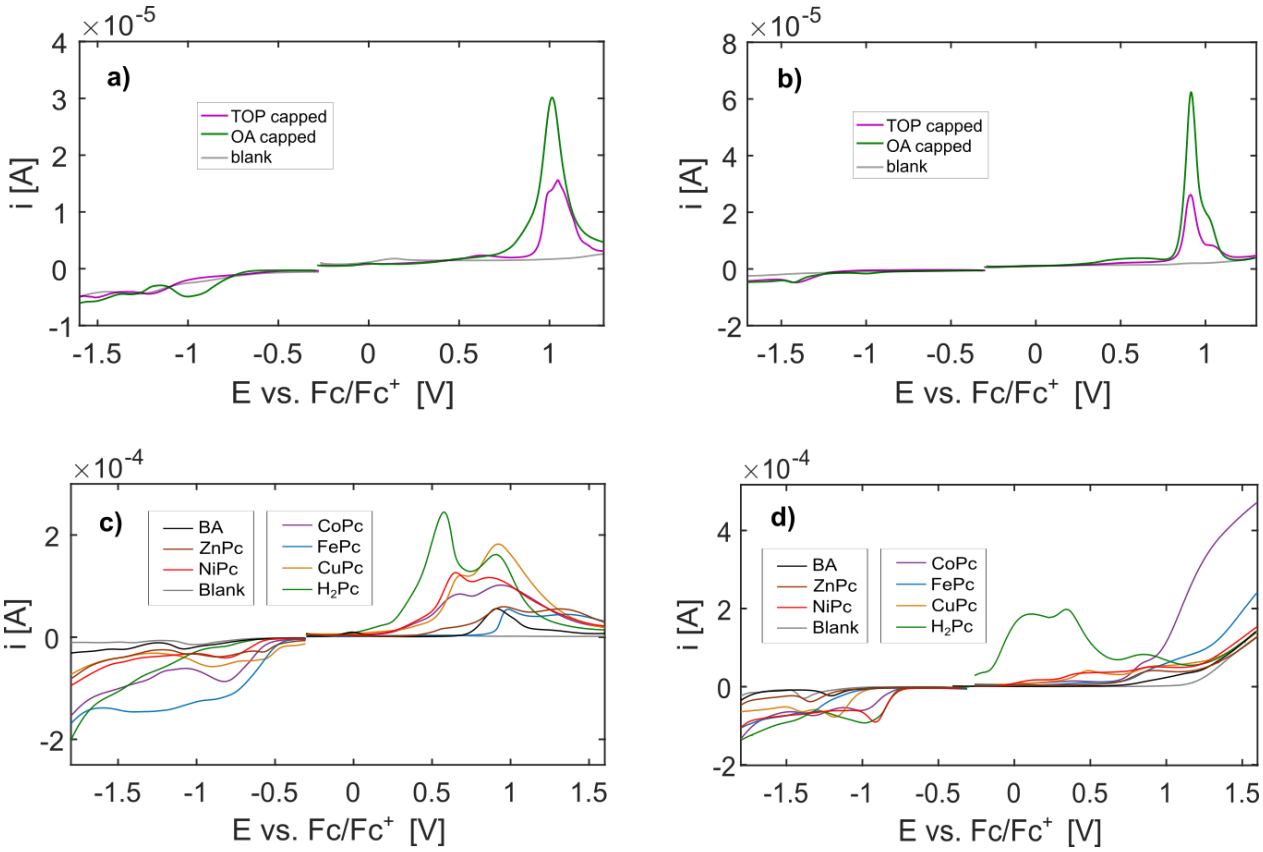

Figure 34: DPV scans of CdSe QDs with the aliphatic ligand BA and various MePcs.
a) CdSe QDs with $MeCN/LiClO_4$ as the electrolyte, measured on the GC WE. b) CdSe QDs with $MeOH/LiClO_4$ as the electrolyte, measured on the GC WE. c) CdSe QDs interlinked with MePc ligands in $MeCN/LiClO_4$, measured on the FTO WE d) CdSe QDs interlinked with MePc ligands in $MeOH/LiClO_4$, measured on the FTO WE.

Measuring into reductive potentials reveals one broad peak for the measurements conducted in $MeOH/LiClO_4$. When measuring in $MeCN/LiClO_4$, two (for the QDs capped with TOP) and three peaks (for the QDs capped with OA) can be observed.

The ligand exchange of the COIN films is verified via Raman spectroscopy. While the spectrum of CdSe particles with BA as ligand shows only the two characteristic peaks for CdSe at 207 and 412 cm^{-1}, the films interlinked with MePc ligands have a number of

peaks which are characteristic for phthalocyanines. They are summarized in **Table 4**. The film with FePc does not show any of these peaks.

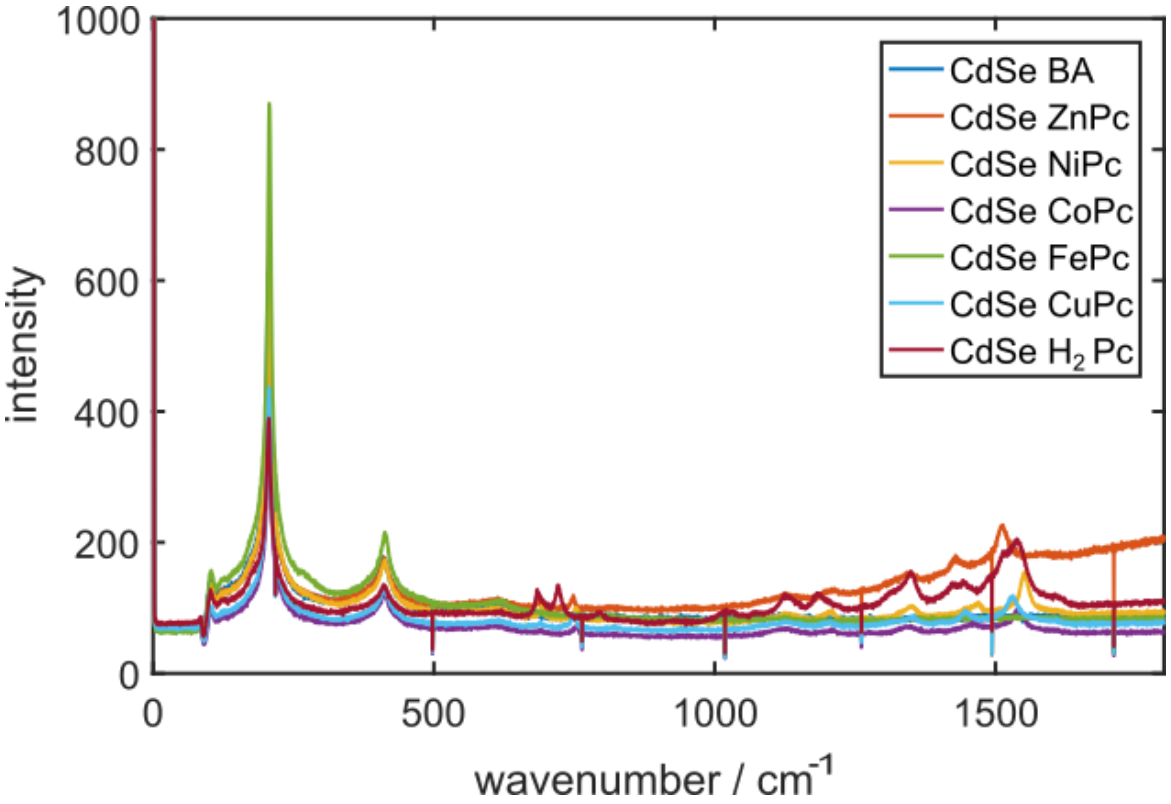

Figure 35: Raman spectra of all COIN films used in this study.

Table 4 summarizes the peaks observed in the Raman spectra and assigns them to a characteristic vibration found in the literature[151-155]:

Upon characterizing the CdSe based COIN films electrochemically with DPV, it can be observed that the reference sample shows the least amount of peaks, the least states in the band gap and overall the broadest peaks with the lowest intensity. This holds true for measurements in both electrolytes. The distinct oxidation peaks observed in the measurements on the GC electrode are broadened and overlaid by a number of additional peaks at 0.5 – 0.6 V vs. Fc/Fc^+ (**Figure 34c+d**).

Table 4: Summary of Raman peaks observed in **Figure 35** and their origins.

Peak #	CdSe + H2Pc [cm^{-1}]	CdSe + ZnPc [cm^{-1}]	CdSe + NiPc [cm^{-1}]	CdSe + CuPc [cm^{-1}]	CdSe + CoPc [cm^{-1}]	description
1	207	207	207	207	207	CdSe
2	412	412	412	412	412	CdSe
3	684	685	692	690	691	bridging C-N-C sym. deform. pyrrole ring OP bend
4	722					macrocycle stretch / central ring twisting
5		750	752	748	753	central ring contraction
6	794					NH_2 wag
7	1019					C-H deformation & aryl C-C stretch
8	1024					C-H deformation & aryl C-C stretch
9		1127	1124	1123	1129	macrocycle stretch / C-H bend
11	1184					pyrrole ring breathing
12	1350	1349	1351	1355	1344	indole
13	1422	1429				indole
14	1442		1469	1446	1457	isoindole ring stretch
15	1516	1511		1530	1542	N-H in macrocycle ring stretch benzene
16	1538	1581	1551	1608		macrocycle in plane stretch
17	1605		1611			NH_2 deformation

Table 5: Location of the first excitonic transition of CdSe based COIN films.
These values are determined from the first derivative of UV-Vis spectra (grey curves in **Figure 36**). The variation is mainly driven by noise in the curves.

Ligand	**First Excitonic Transition**	
	Wavelength [nm]	Energy [eV]
BA	623±1	1.990±0.004
ZnPc	619±7	2.00±0.03
NiPc	624±2	1.99±0.01
CoPc	619±8	2.00±0.03
FePc	626±2	1.98±0.01
CuPc	626±2	1.98±0.01
H_2Pc	638±2	1.94±0.01

The COIN samples are then characterized by UV-Vis spectroscopy and EMAS. For each sample, a UV-Vis spectrum is recorded in a Varian Cary 5000 spectrophotometer (black curves in **Figure 36**). The grey curve in **Figure 36** is the first derivative of this spectrum which is added to the figure to better visualize the optical transitions of the QDs and the absorption of the phthalocyanines around 650 – 750 nm (**Figure 52**).

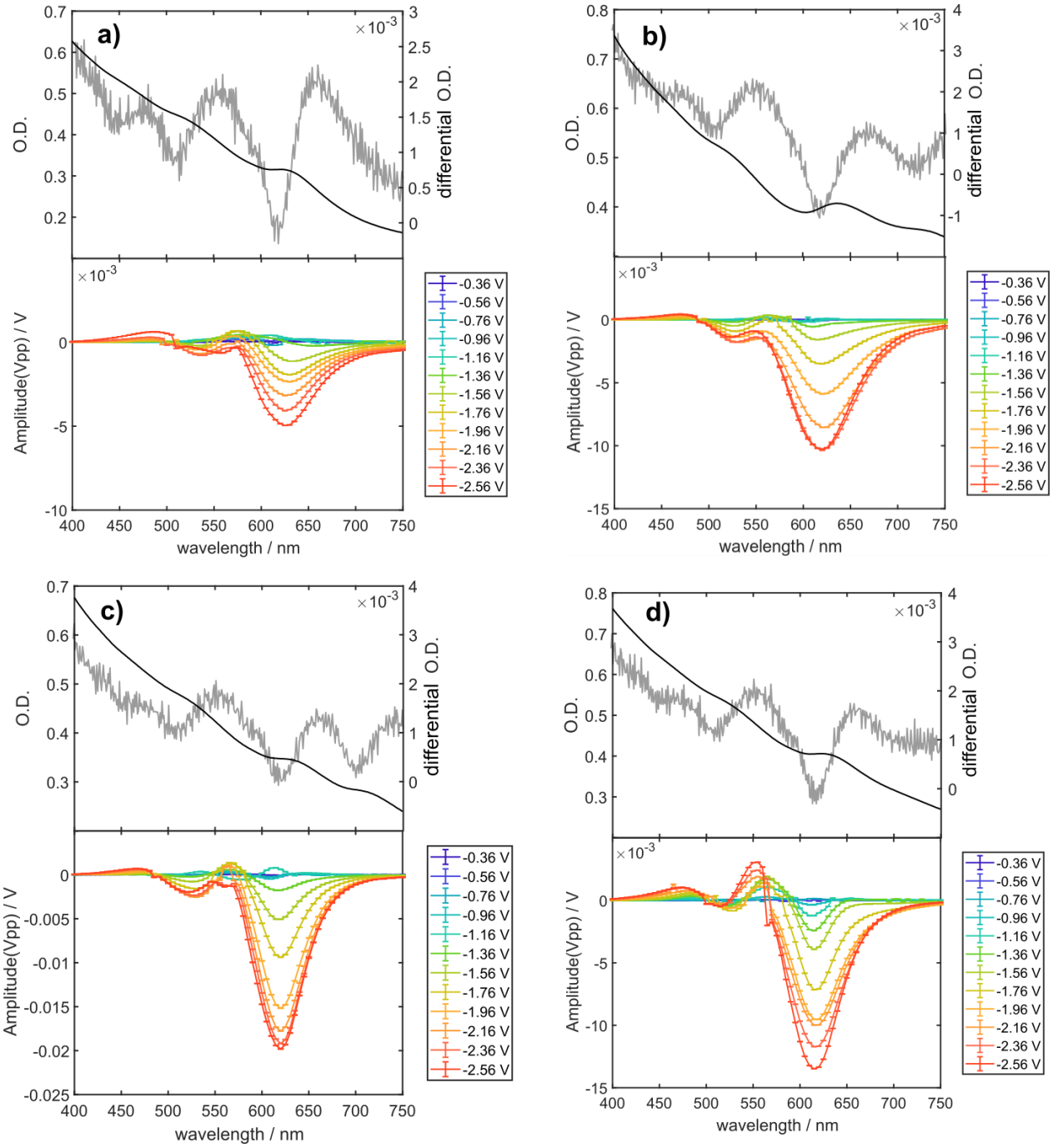

Figure 36: UV-Vis and EMAS spectra of CdSe films with BA ligands and various MePc linkes. a) CdSe QDs with BA ligands, b) CdSe QDs interlinked with H_2Pc, c) CdSe QDs interlinked with ZnPc and d) CdSe QDs interlinked with CoPc. A subsequent calibration of the monochromator showed that the real wavelength value is 3 nm higher than shown in this figure.

The location of the first excitonic transition of the CdSe based COIN films is summarized in **Table 5**. These values are determined from the first derivative of UV-Vis spectra (grey curves in **Figure 36**). The variation is mainly driven by noise in the curves.

The EMAS spectra show four peaks: two of them are bleaches and two induced absorptions. In the following, the bleach at ~620 nm is called peak 4 (the first excitonic

transition), the bleach at ~520 nm is called peak 2, the induced absorption at ~560 nm is called peak 3 and the induced absorption at ~470 is called peak 1.

The electrochemical potential quoted for EMAS data in this chapter is the potential set by the potentiostat (E_{DC_ref}). A value of 0 V is chosen for E_{DC_ref} because it is inside the band gap and sufficiently far away from the CB edge. This value is referenced against the ferrocene/ferrocenium couple (0.26 V for all EMAS measurements quoted here) and the reference amplitude U_{ref} is added to it. Each graph in **Figure 36** corresponds to one combination of E_{DC_ref} and U_{ref}, referenced against Fc/Fc^+.

The same measurement is also performed on bare FTO with the same electrolyte (**Figure 37**). It can be seen that the UV-Vis spectrum of FTO is not entirely smooth and the EMAS measurement reveals a certain absorption change in the region between 400 and 750 nm. The magnitude of this absorption change is however so low that the analyte signal of the QD films can be clearly observed.

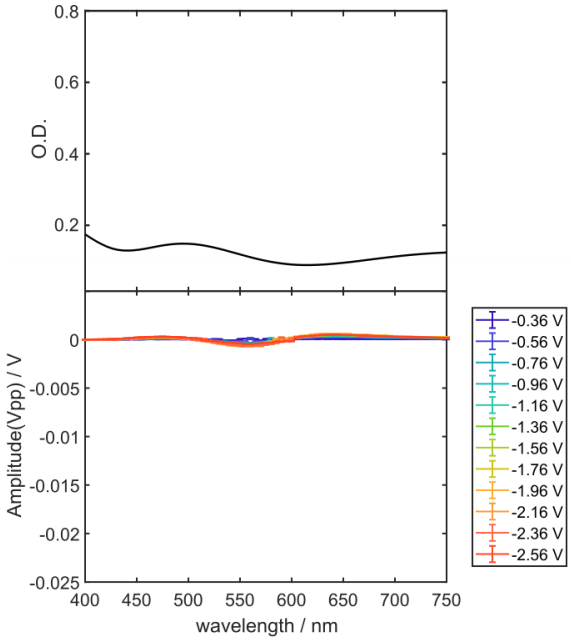

Figure 37: UV-Vis spectrum (above) and EMAS spectrum (below) of the uncoated FTO electrode. A subsequent calibration of the monochromator showed that the real wavelength value is 3 nm higher than shown in this figure.

It can be seen that peaks 2 and 4 are always bleaches and peak 1 is always an induced absorption. Peak 3 always starts as an induced absorption, but drops into negative values (bleach) for all samples except CoPc and FePc. The wavelength at which the graph crosses the x-axis between peak 1 and 2 stays constant over all applied potentials for all samples except those films interlinked with CoPc.

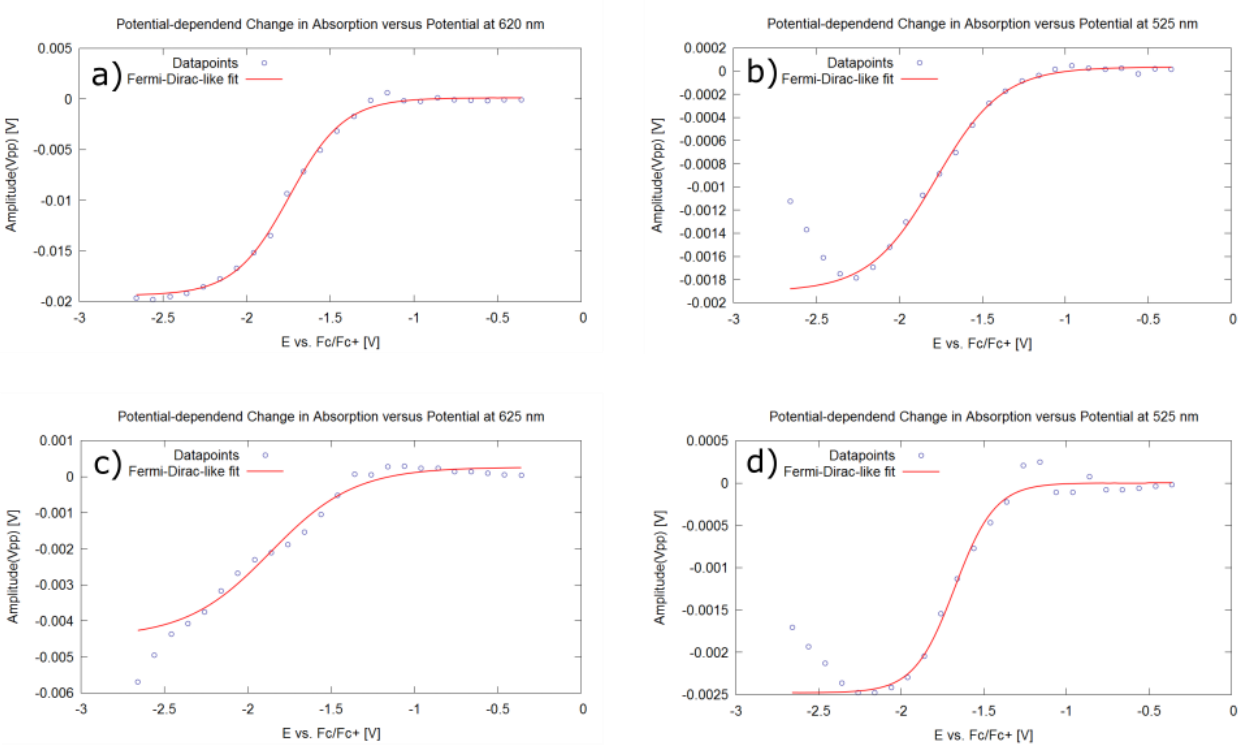

Figure 38: Fermi-Dirac fits of EMAS peaks recorded at a single wavelength and the observed fit errors. a) Fermi-Dirac fit at the maximum of peak 4 in an EMAS spectrum recorded for a CdSe film interlinked with ZnPc. The Fermi-Dirac function is a good fit for the data. b) Error 1, observed in a CdSe film interlinked with H_2Pc, c) Error 2, observed in a CdSe film interlinked with BA, d) Error 3, observed in a CdSe film interlinked with ZnPc.

The EMAS peaks do not grow linearly, but rather show a sigmoidal curve progression which is similar to a Fermi-Dirac distribution. When plotting the absorption values of an EMAS peak at only one wavelength against the potential, a voltabsorptogram with a sigmoidal shape is obtained. As stated in **Chapter 7.3**, the Fermi level is located at the inflection point of the Fermi-Dirac distribution. Similarly, the CB edge can be derived from the inflection point of the curve shown in **Figure 38a**. To localize this inflection point, the curve is fitted with a Fermi-Dirac function of the form[156]:

$$V_{PP}(E) = \frac{V_{PP,end} - V_{PP,start}}{1 + e^{\frac{E-E_0}{\xi}}} + V_{PP,end} \qquad (30)$$

$V_{PP}(E)$ is the peak to peak amplitude measured in an EMAS experiment as a function of the electrochemical potential E. $V_{PP,start}$ and $V_{PP,end}$ are the asymptotically approached values of V_{PP} far away from E_0. ξ indicates the broadness of the sigmoidal curve.

In this work, the Fermi-Dirac fit is conducted with an initial ξ value of 0.05 V because values of this size are reported in the literature[109]. After iterating the fit parameters with the experimental data, ξ values ranging from 0.07 to 0.35 V are calculated (see

Appendix 14.2). E_0 is the potential at which 50 % of the absorption is changed (quenched or induced). It is the most important parameter that comes out of the model calculation and corresponds to the lowest unoccupied state in the QD film[109].

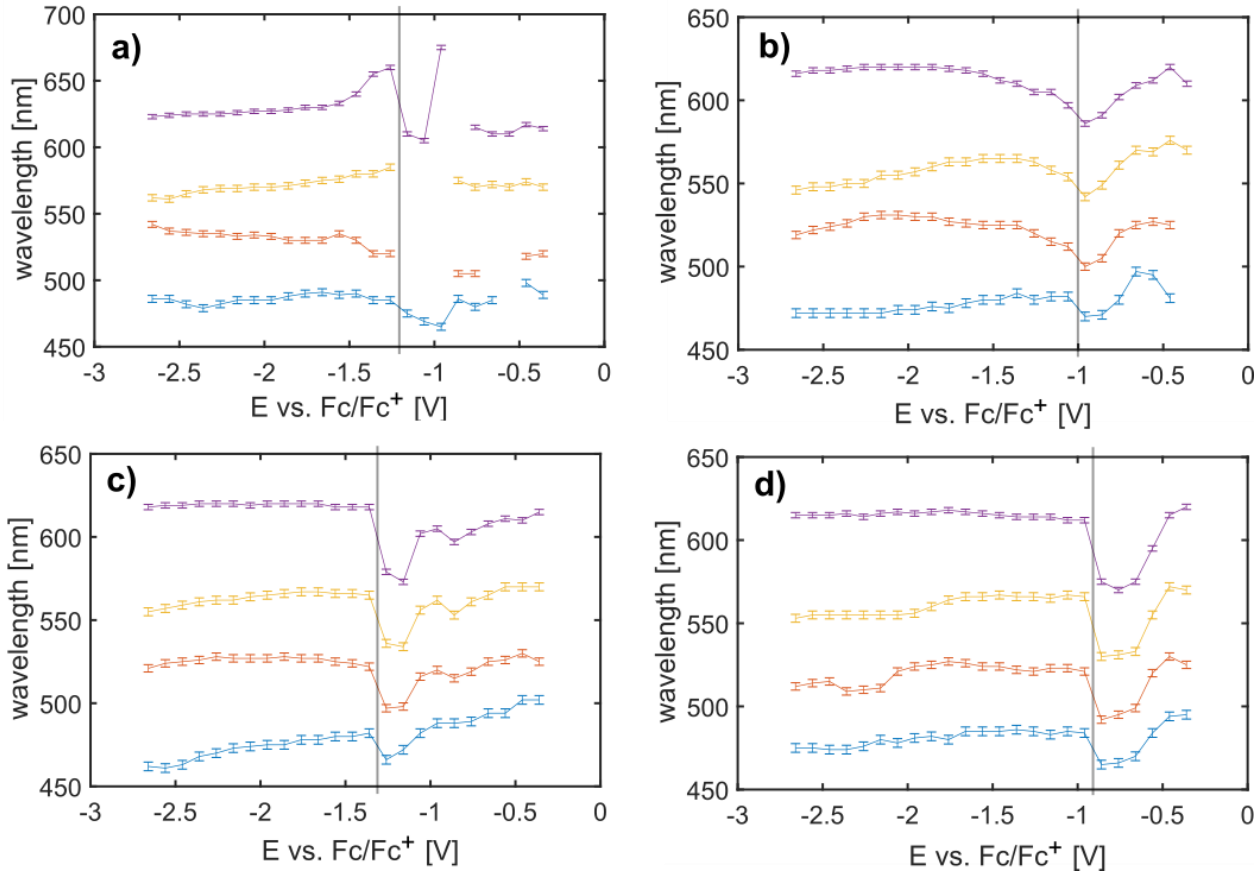

Figure 39: Maxima of the EMAS peaks as a function of the applied potential.
Peak 1 is depicted in blue, peak 2 in orange, peak 3 in yellow and peak 4 in purple. a) CdSe QDs with BA ligands. b) CdSe QDs interlinked with H_2Pc. c) CdSe QDs interlinked with ZnPc. d) CdSe QDs interlinked with CoPc. A subsequent calibration of the monochromator showed that the real wavelength value is 3 nm higher than shown in this figure.

The fit works generally well for peaks 1, 2 and 4. Peak 3 does not yield any conclusive curve as it starts as an induced absorption and becomes a quenched absorption at higher potentials. Care must be taken when interpreting the E_0 value obtained for these curves since the fit is not always ideal. For some samples, the absorption change goes back towards 0 when measuring at higher potentials (error 1), for some samples there is no plateau formed towards higher potentials (error 2) and some samples show quite scattered data that is generally hard to fit (error 3).

The values with the best fits (not showing error 2) for E_0 of peaks 1, 2 and 4 (the EMAS measurements are repeated twice) are summarized in **Table 6**.

Starting at a potential within the band gap (-0.36 V vs. Fc/Fc^+), the samples get polarized with increasingly negative potentials. This leads to a blue shift of the maximum of all

four peaks and then a sudden red shift. To investigate this observation further, the position of the peak maxima is determined for each graph separately (other than in the Fermi-Dirac fits where all absorption values are picked for one wavelength) and plotted against the electrochemical potential. The error bars in **Figure 39** show ±1 standard deviation. The standard deviation is calculated by averaging the standard deviation per peak over all measured samples. While it is possible to determine the peak positions for the COIN films, the sample with BA ligands does not always allow a definitive assignment of peaks in the lower potential regime.

The potential at which the peaks find their final position, differs from sample to sample. When determining the onset potential from the peak position plots (**Figure 39**), an onset potential (marked by a vertical grey line) of -1.30 V vs. Fc/Fc^+ can be found for CdSe particles interlinked with ZnPc, the films interlinked with NiPc and FePc show an onset potential of -1.25 V vs. Fc/Fc^+. An onset potential of -1.15 V vs. Fc/Fc^+ can be observed for CdSe films interlinked with CuPc and an onset potential of -1.00 V vs. Fc/Fc^+ can be seen for CdSe films interlinked with H_2Pc. The films interlinked with CoPc have the lowest onset potential at -0.90 V vs. Fc/Fc^+.

The position of the red shift also marks the potential at which the peaks start growing in magnitude. At the beginning of the experiment when the peak positions show a blue shift, the peaks are not very clearly defined (see **Figure 40a**). When passing that potential, the shape of the peaks becomes much smoother (see **Figure 40b**), they grow in magnitude (see **Figure 40c**) and the phase of the measured data changes less frequently (see **Figure 40d**). This often happens from one potential step to the next. In the following, the first potential where a smooth curve can be observed is referred to as the onset potential. The example below depicts the measurement at -1.26 V vs. Fc/Fc^+ (**Figure 40a**+**c**) and -1.36 V vs. Fc/Fc^+ (**Figure 40b**+**d**) for a CdSe film interlinked with ZnPc.

The yellow line in **Figure 40a**+**b** is a guide to the eye and depicts 0 V V_{PP}. The areas shaded in yellow in **Figure 40c**+**d** indicate the datapoints for which a phase > ± 90° is measured (absorption bleach). The areas shaded in green indicate the datapoints for which a phase < ± 90° is measured (induced absorption).

One might expect more peaks in the EMAS spectrum towards higher wavelengths because the absorption of the phthalocyanines starts at around 600 nm and goes up to 900 nm. However, no peaks can be observed in this area in EMAS measurements.

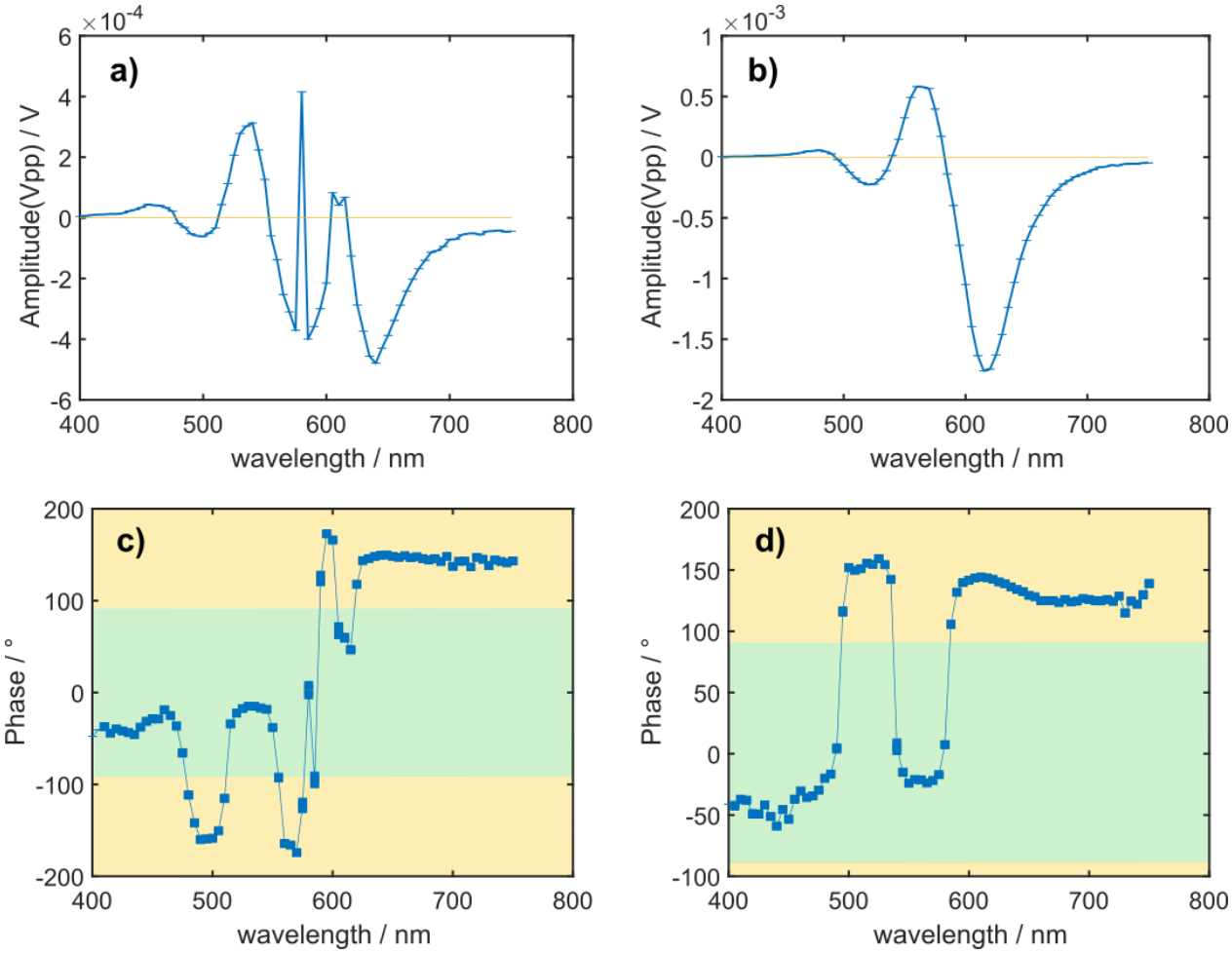

Figure 40: EMAS amplitude and phase for CdSe QDs interlinked with ZnPc.
The upper row depicts the peak to peak amplitude in V for a potential of (a) -1.26 V vs. Fc/Fc^+ and (b) -1.36 V vs. Fc/Fc^+. The bottom row depicts the respective phase of the datapoints.

Table 6 summarizes the values for E_0 calculated from the Fermi-Dirac fits of the EMAS data as well as the peak onset potentials as there is a significant discrepancy in these numbers. The last column summarizes this difference in electrochemical potential of the E_0 value of peak 4 and the onset potential.

Table 6: Fermi-Dirac inflection points E_0 and peak onsets for CdSe films interlinked with MePc ligands.

Sample	E_0 for peak 1 [V vs. Fc/Fc^+]	E_0 for peak 2 [V vs. Fc/Fc^+]	E_0 for peak 4 [V vs. Fc/Fc^+]	onset potential [V vs. Fc/Fc^+]	Δ between E_0 and onset potential [mV]
CdSe + BA		-1.48		-1.20	280
CdSe + ZnPc	-2.07	-1.67	-1.75	-1.30	450
CdSe + NiPc	-2.02	-1.61	-1.70	-1.25	450
CdSe + CoPc	-1.75		-2.13	-0.90	1230
CdSe + FePc		-1.60	-1.89	-1.25	640
CdSe + CuPc	-1.94	-1.82	-1.51	-1.15	360
CdSe + H_2Pc	-2.10	-1.78	-1.95	-1.00	950

Only E_0 values from fits with a good or medium quality (see **Appendix 14.2**) are selected. Good quality fits do not show any of the above errors, medium quality fits show errors 1 or 3, poor quality fits show error 2.

10.2.4.2 Discussion

The success of ligand exchange in COIN films based on CdSe is verified via Raman spectroscopy. The presence of a number of peaks typical for phthalocyanines in the COIN films means that the linker molecules are present in the film. It cannot be concluded from these Raman measurements that the linkers actually bind to the QDs, but the mechanical stability of the films speaks for a chemical binding between the linkers and the QDs. If there would be no chemical binding, the films would detach from the electrode when dipping them into the QD solution during the layer-by-layer fabrication of the films.

The COIN film with FePc does not show any of the characteristic phthalocyanine peaks, but does show the characteristic green color originating from the phthalocyanine when being visually inspected. It is therefore assumed that the ligand exchange with FePc is not as complete with the other linkers, leading to less FePc in the film. It does however lead to a mechanically stable film that can be characterized electrochemically without any preliminary detachment of the QDs from the electrode.

Upon characterizing CdSe based COIN films, it can be observed that the samples measured on FTO WEs are broadened. This is due to the lower conductance of the FTO electrode as compared to the GC WE used in the experiments on CdSe particles with BA ligands. It can also be observed that the films with CdSe QDs and BA ligands on the FTO electrode have the lowest magnitude. This is based on the lower film thickness of this sample because it has only one layer of QDs while the COIN films consist of eight layers.

The DPV peaks resulting from the CdSe VB (peak positions highlighted in blue in **Table 7**) can be clearly distinguished from the peaks resulting from the MePc a_{1u} orbital (peak positions highlighted in orange in **Table 7**). The VB of the QDs can be observed at around 1 V vs. Fc/Fc^+ which is roughly in accordance with the literature value of 0.7 V vs. Fc/Fc^+[60]. The HOMO of the MePc linkers is expected at 0.15V vs. Fc/Fc^+. The data shows that the HOMO of the linkers is observed at slightly more oxidative potentials which might be due to the amino groups on the experimentally investigated molecules that are absent in the theoretical calculations performed by Liao et al.[140]. Since the VB of the QDs as well as the HOMO of the linkers is shifted towards more oxidative potentials as compared to the literature, this could as well be an effect of the solvent.

The LUMO of the MePcs (peak positions highlighted in green in **Table 7**) is expected to be located at a similar energy as the QD CB (peak positions highlighted in yellow in **Table 7**) from the literature[60, 140]. The results obtained here suggest that there is some interaction between the MePc $2e_g$ orbitals and the QD $1S_e$ state as will be shown later.

Table 7: Summary of peak potentials measured for CdSe QDs in MeCN/$LiClO_4$ and MeOH/$LiClO_4$. Values highlighted in yellow are assumed to result from the MePc LUMO, values highlighted in green are assumed to result from the QD CB, values highlighted in orange are assumed to result from the MePc HOMO and values highlighted in blue are assumed to result from the QD VB.

	Ligand	Peak Potentials [V vs. Fc/Fc⁺]										
MeCN/LiClO4	TOP		-1.54	-1.23						0.59	0.97	1.05
	OA		-1.42	-1.17		-0.84			0.46		0.84	1.01
	BA	-1.72	-1.51		-1.11	-0.93		0.02			0.89	1.24
	ZnPc		-1.52		-1.09	-0.90	-0.60		-0.26	0.56	0.93	1.31
	NiPc		-1.50	-1.22	-0.84				0.40	0.62	0.84	
	CoPc		-1.37	-1.18	-0.85				0.38	0.65	0.91	
	FePc		-1.36	-1.28	-0.92					0.47	0.95	1.35
	CuPc		-1.50		-0.92	-0.68	-0.40		0.39	0.66	0.89	
	H_2Pc	-1.58	-1.26		-0.84				0.15	0.55	0.88	
MeOH/LiClO4	TOP			-1.43			0.50	0.91	1.04			
	OA			-1.39			0.60	0.95	1.06			
	BA	-1.61		-1.24	-1.05			1.15				
	ZnPc	-1.71		-1.37		0.00		0.92				
	NiPc	-1.54	-1.14	-1.38	-0.94	0.10	0.43	0.92				
	CoPc			-1.36	-1.04		0.35	0.85				
	FePc	-1.57		-1.39			0.46	1.02				
	CuPc	-1.79	-1.42	-1.21		0.02	0.46	0.92				
	H_2Pc	-1.50		-1.25	-1.01	0.08	0.31	0.85				

There is, however, also some evidence of the states not fully coupling, as the MePc a_{1u} orbitals and the PbS QD $1S_h$ state do, since there are still some peaks visible that can be attributed to the MePc $2e_g$ orbitals. Also, initial conductance measurements with the CdSe based COIN films interlinked with MePcs are not successful which is an indication of the MePcs not coupling with the QDs in a way that a CB/LUMO miniband is formed.

Generally speaking, it is easier to distinguish trap states from CB and VB edge for PbS particles than for CdSe samples. Especially towards the CB, peaks often look very similar in terms of shape and intensity.

Table 7 summarizes all the peak potentials measured in the DPV experiments with CdSe QDs. The peaks highlighted in green (CB) and blue (VB) are assumed to be the band edge positions and are used for the calculations summarized in **Table 8**. The peaks highlighted in yellow are assumed to originate from the $2e_g$ orbitals in the MePcs, the peaks highlighted in red are assumed to originate from the a_{1u} orbitals in the MePcs.

There is a lower lying state close to the CB for the COIN films with NiPc, CoPc and FePc for the measurements conducted in MeCN. The same state can be observed for the film with BA ligands and the COIN films with NiPc, CoPc and H_2Pc for the measurements conducted in MeOH. Assuming this to be a sort of newly formed hybrid orbital from the QD $1S_e$ state with the MePc $2e_g$ orbital is helpful to interpret the findings from the EMAS measurements. It is however necessary to mention that the band gap calculated with these values leads to slightly smaller electronic transport band gaps than optical band

gaps for the COIN films with NiPc, CoPc and FePc for the measurements conducted in MeCN.

Table 8: Summary of proposed band potentials and band gap estimates of the CdSe based COIN samples.

Electrolyte	Ligand	CB [V vs. Fc/Fc⁺]	CB [eV Vac]	VB [V vs. Fc/Fc⁺]	VB [eV Vac]	$E_{g,el}$ [V]	$E_{g,opt}$ [V]
MeCN/ $LiClO_4$	TOP	-1.54	-3.32	0.97	-5.77	2.45	2.11
	OA	-1.42	-3.44	0.84	-5.64	2.20	2.09
	BA	-1.51	-3.35	0.89	-5.75	2.40	1.99
	ZnPc	-1.52	-3.34	0.93	-5.79	2.45	2.00
	NiPc	-1.22	-3.64	0.84	-5.70	2.06	1.99
	CoPc	-1.18	-3.68	0.91	-5.77	2.09	2.00
	FePc	-1.28	-3.58	0.95	-5.81	2.23	1.98
	CuPc	-1.50	-3.36	0.89	-5.75	2.39	1.98
	H2Pc	-1.26	-3.6	0.88	-5.74	2.14	1.94
MeOH/ $LiClO_4$	TOP	-1.43	-3.43	0.88	-5.74	2.31	2.11
	OA	-1.39	-3.47	0.92	-5.78	2.31	2.09
	BA	-1.05	-3.81	1.12	-5.98	2.17	1.99
	ZnPc	-1.37	-3.49	0.89	-5.75	2.26	2.00
	NiPc	-0.94	-3.92	0.89	-5.75	1.83	1.99
	CoPc	-1.04	-3.82	0.82	-5.68	1.86	2.00
	FePc	-1.39	-3.47	0.99	-5.95	2.38	1.98
	CuPc	-1.21	-3.65	0.89	-5.75	2.10	1.98
	H2Pc	-1.01	-3.85	0.82	-5.68	1.83	1.94

The appearance of this state at the film with the aliphatic ligand BA contradicts the assumption that this might be an indication of the coupling between CdSe QDs with MePc ligands. This peak is however quite shallow and in close proximity with an irregularity in the background scan (**Figure 34**) and can therefore also be interpreted as a measurement artifact.

The optical band gaps reported in **Table 8** are calculated from the first derivative of the UV-Vis spectra recorded for these films.

From the calculations performed in this table, it can be seen that some electronic band gaps are smaller than the corresponding optical band gaps for the measurements conducted in MeOH. This is true for the films interlinked with NiPc, CoPc and H_2Pc and is usually a strong indication that a proposed CB signal is, in fact, a state within the band gap since $E_{g,el}$ has to be always bigger than $E_{g,opt}$ according to the laws behind **Equation 4**. It is however worth mentioning that $E_{g,el}$ is only max. 160 mV smaller than $E_{g,opt}$ and only in one of the electrolytes that are used in this study. The discrepancy of 140 mV between $E_{g,el}$ and $E_{g,opt}$ in the COIN films with CoPc might also be smaller when taking the uncertainty of $E_{g,opt}$ into account. That can as well be 1.97 eV instead of 2.00 eV.

The peaks can therefore not be ruled out as the CB but need further verification. That can be done by the use of a spectroelectrochemical technique such as EMAS.

Upon investigating the films with EMAS, the assignment of optical transitions to peaks 2 and 4 is relatively straightforward. In the work of Spittel et al.[109], the first four optical

transitions of the QDs can be seen as two pairs of peaks in the EMAS spectrum. Due to the thicker films used in this experiment (ca. 8 layers instead of one) these peaks are most likely broadened and the two peaks of one pair are not distinguishable any more. Peak 4 is therefore caused by the quenching of the $1S_{3/2} - 1S_e$ and the $2S_{3/2} - 1S_e$ transition. Peak 2 is caused by the quenching of the $1S_{1/2} - 1S_e$ and the $2S_{1/2} - 1S_e$ transition[109, 157, 158].

Peaks 1 and 3 may result from absorption of the CdSe particles in their excited states. Optically excited electron-hole pairs can interact with electrons in their ground states and enable initially forbidden optical transitions[157, 159] to be allowed. As these transitions become allowed only during the measurement, they can be seen as induced absorptions in the EMAS spectrum.

I hypothesize that the bleaching of peak 3 (initially starting as an induced absorption) at more negative potentials is an effect of the absorption of the phthalocyanine ligands, since this phenomenon is described nowhere in the literature for measurements of CdSe QDs with aliphatic ligands. An EMAS measurement of pure ZnPc on FTO reveals an induced absorption at about the wavelength range of peak 3 that decreases upon increasing the potential (see **Figure 49** in **Appendix 14.2**).

EMAS measurements of the pure linkers are however hard to interpret since the peaks are not as strong as for CdSe QDs, which could also explain the absence of any signals in the EMAS spectra above 700 nm. Pure MePc ligands also detach quite easily from the electrode which makes it difficult to assess whether a change in intensity is due to electrochemical changes in the material or a depletion of material on the electrode.

The FTO used in this study also changes its absorption characteristics upon electrochemical polarization. This fact led to some confusion in the early stages of operating this EMAS setup, but clarity could be gained by now. The UV-Vis spectrum of pure FTO shows a broad peak at 500 nm (**Figure 37**). Upon placing the FTO in an electrical field, as done so during an EMAS experiment, this peak broadens due to the quantum confined Stark effect[160]. This broadening leads to a bleach of the peak at its center and an induced absorption at the edges of the peak. It is unfortunate that these peaks coincidently overlap with the peaks of the CdSe QDs that should actually be observed in this experiment.

When applying a potential to the FTO electrode coated with QDs, the peaks originating from the QDs are initially influenced and partially obscured by the peaks originating from the FTO. This leads to an apparent blue shift of the QD peaks. At a certain potential, they outgrow the FTO peaks in magnitude and their position is not influenced by the measurement artifact any more. So the apparent blue and red shifts seen in **Figure 39** are not actually changes in optical transitions. The information gained from these plots is however quite useful since it helps to easily and accurately define the potential at which the peaks start to grow in magnitude (peak onset).

The peak onset describes the potential, at which the first states of the CB get filled. Due to the broadening of the Fermi level at room temperature, the first states are expected to get filled at about 4 k_BT = 100 mV before the Fermi level equals the CB edge[109] (see **Figure 3**). The occupancy of the CB is assumed to be 1 % then. When the Fermi level equals the CB edge, 50 % of the states are occupied (assuming a symmetrical energy distribution of the $1S_e$ state). Full occupation (99 %) of the $1S_e$ state is assumed to happen when the Fermi level is expected to be about 100 mV above the CB edge.

When plotting the absorption of the material against the potential, this behavior can be visualized through the amount that the optical transitions get bleached (**Figure 38**). The position of the CB edge is in the inflection point of this curve. Some caution has to be exercised when quoting these E_0 numbers because the fitting of the data is not always good.

As shown in **Figure 38**, there are three types of errors that can happen when fitting the data. Error 1 is a lack of fit when the data approaches 0 V V_{PP} after forming a (very brief) plateau region from which $V_{PP,end}$ can be determined. This behavior of the data is most likely due to degradation or detachment of the analyte from the electrode. The fit can still be made, however the last data points have to be excluded.

Error 2 is a lack of fit due to the data not forming a plateau region towards the end of the measurement at all. This might be due to inhomogeneous charging of the COIN film and is particularly hard to fit. The values obtained with this fit should be treated with great caution.

Error 3 is a general noisiness of the data that can have a variety of causes. However, the fit of these data sets is relatively robust, as compared to those which show error 2.

Generally, the inflection point of this Fermi-Dirac distribution (E_0) is supposed to be higher (about 100 mV) than the potential of the peak onset as determined from the peak-position plots (**Figure 39**). It can however be observed that the peak onsets measured here are up to 1.23 V lower than the E_0 (**Table 6**). Especially the peak onsets of the films with CoPc (1.23 V) and H_2Pc (0.95 V) are considerably lower than their respective E_0 values. These fits show errors 1 and 3 which still allows a good estimate on the position of E_0.

There are several possible explanations for the larger than expected discrepancy between the peak onset and E_0.

When comparing the E_0 values of the different peaks of one sample, it can be seen that they can already differ by as much as 410 mV (peak 1 and 2 for the sample interlinked with NiPc, see **Table 6**). From the theory described in **Chapter 8.5.2**, the optical transitions behind peaks 2 an 4 should get bleached at the exact same potential. The ground state of the electrons might be different, but they all get excited to the 1 S_e level. It is therefore not clear whether the E_0 value for peak 2 or peak 4 is the correct one.

It was also assumed first that peaks 1 and 2 are correlated which would mean that they develop simultaneously and have a clear isosbestic point between them[161]. This point can be observed in all samples except the one interlinked with CoPc. It can however not be seen that the peaks develop simultaneously at the same potentials. Peak 1 might therefore not be connected to peak 2, that is, the optical $1S_{1/2} - 1S_e$ and $2S_{1/2} - 1S_e$ transition is influenced by other optical transitions like those originating from the linker molecules.

A possible reason for the less than ideal correlation of the EMAS peaks may be the detachment of sample material from the electrode. All films are inspected visually before and after the experiment and only minor changes in the film opacity are observed. This could however be enough to be seen in a technique as sensitive as EMAS. The Raman spectra (**Figure 35**) of the COIN films reveal higher intensities for the peaks specific to phthalocyanies for the samples prepared with NiPc, ZnPc and H_2Pc than for the sample prepared with CoPc and FePc. It can therefore be assumed that the ligand exchange with Fe and CoPc is not as successful compared with the other three linkers and the film is therefore less stable to electrochemical stress.

It has to be mentioned however that the samples prepared with CoPc and FePc do not show error 1 (which is associated with sample degradation) in the Fermi-Dirac fits more often than the other samples. It is also not clear how sample detachment from the electrode would affect the correlation of the EMAS peaks to one another.

When coming back to the E_0 values of peaks 2 and 4, it can be said that they differ from each other by maximally 310 mV for CdSe films interlinked with CuPc. It has to be said that in this case, -1.51 V vs. Fc/Fc^+ for peak 4 is a quite low value and it is obtained from a different sample than the value for peak 2. The fit for peak 4 on the same sample is less satisfactory, so it has to be treated with caution, but when comparing its value to peak 2, it is more appropriate to use this value (-1.93 V vs. Fc/Fc^+) because it is measured on the same sample. So when using values for peaks 2 and 4 from the same sample, the discrepancy shrinks down to 110 mV.

The next highest discrepancy can be found for the films interlinked with FePc where a quite similar issue arises. When comparing the E_0 value of peak 2 here to the E_0 value of peak 4 in the same sample (which has a poor fit quality and an E_0 value of -1.76 V vs. Fc/Fc^+), the discrepancy between the peaks shrinks down to 170 mV.

The outcome of these comparisons shows that there are clear trends visible in the data, but also some variation from sample to sample can be observed. It is therefore advisable to repeat the measurements in order to get a better statistical basis for the conclusions drawn from the results. So in the following, data will be discussed on a more qualitative level.

The generally higher discrepancy of the peak onset and E_0 across all measured samples can be attributed to the thicker QD films on the electrode compared to what is used in

the literature. Here, the lower layers start to show a change in absorption while the electric field has not yet reached the outer layers of the film. Even though lithium is a very small cation, there might be limited diffusion of the electrolyte through the film because phthalocyanines are quite stiff ligands (see **Chapter 8.1.2**). Electron injection from the electrode to the QDs can only happen when the charge in the film is compensated by the presence of positive charges in the form of electrolyte cations. Dielectric charging of the film is possible, but cannot extend as far and is leading to a charge gradient in the film.

This way, the electric field that the outer layers of the film "see" is always lower than that applied to the electrode and the inner layers of the film. The result here is that the peak onsets accurately describe the position where the first electrons from the electrode get injected into the CB of the COIN film while E_0 is measured tendentially at too high reductive potentials. The values for E_0 measured in this work range from -1.51 to -2.13 V vs. Fc/Fc^+ while the literature reports values around -2.9 to -3.5 eV vs. Vac for the CB of CdSe QDs of comparable size which can be converted to -1.3 to -1.9 V vs. Fc/Fc^+[60, 162]. So the E_0 values measured here are only shifted to higher reductive potentials by 200 mV. This is still in quite good agreement with the literature, especially given that the values in the literature are determined under different experimental conditions.

It can thus be said that while there is still room for improvement on the measurement accuracy on the EMAS setup, it is very suitable for determining the position of the CB edge.

The only observation that is not in line with results in the literature[109, 156] is the high discrepancy between the peak onset values and the E_0 values. This might be due to the coupling of the phthalocyanine LUMO orbitals with the electronic states in the QD CB. If all ligands within one film would couple with the QDs that way, the first excitonic peak of the QDs as observed in the UV-Vis spectra (**Figure 36**) would completely vanish because the CB would be completely replaced by this new type of hybrid orbital and optical transitions would be completely quenched. It is however likely that not all QDs couple electronically with their ligands, thus leaving some QDs coupled and some uncoupled. That would explain the still existing excitonic peak in the UV-Vis spectrum. In DPV measurements, a peak at the expected position of the CB can be detected, as well as a state just below it (see **Table 7**). It is also noteworthy that the two films that show this state just below the CB in DPV measurements are also the samples with much lower peak onsets and higher discrepancies between peak onsets and E_0 values in EMAS measurements (CoPc and H_2Pc, see **Table 6**).

This effect is most pronounced for the films interlinked with CoPc. Here, the state below the CB can be observed in both electrolytes in DPV measurements, it has the lowest potential for the peak onset and the highest discrepancy between peak onset potential and E_0 value.

It can be hypothesized that in CdSe films with CoPc, the $2e_g$ orbital of the MePcs interacts with the $1S_e$ state of the QDs in a way that it partially couples with it, resulting in a new hybrid state as well as evidence of the remaining initial state. This leads to a "smearing out" of states below the CB and therefore a lower peak onset in EMAS measurements.

One might think that the filling of these states leads to optical transitions in quite different regions of the electromagnetic spectrum, but it has to be kept in mind that the peaks observed in the EMAS spectra are very broad. Peak 4 for example spans from 580 to 750 nm which is an energy range of 2.14 to 1.65 eV. Optical transitions to the lower lying hybrid orbitals discussed in the above must appear at higher wavelengths which could also explain the trailing of peak 4 towards higher wavelengths. This trailing cannot be observed in the literature. However, it has to be mentioned that the peak measured by the group of Eychmüller[109] is cut short at its lower energy end by an induced absorption of the FTO electrode.

10.2.4.3 Conclusion

It can be concluded that interlinking CdSe QDs with MePc ligands does not only increase the mechanical stability of the films, but also shows some interesting effects that can be attributed to electronic coupling of the MePc LUMO with the QD CB. There is also evidence that not all tested MePc linkers couple with the QDs in the same way. An additional state below the CB can be detected both by DPV and EMAS, which is an indication of this state not being only a surface trap, but linked to optical transitions to the CB. This effect is most pronounced in CdSe films interlinked with CoPc ligands.

10.3 Efficient Electron Transport Enabled via Crosslinking of PbS QDs with T3DSH and T3DSAc

10.3.1 Introduction

As stated in the overall introduction, the goal is to prepare highly conductive films by interlinking semiconductor QDs with a semiconducting organic molecule. The two important properties of these materials are that a) they have a strong chemical coupling and b) an electronic coupling of their energy levels which align in a way that makes it possible for charge carriers to cross from one material to the next[30].

T3DSH is chosen as a suitable linker for PbS QDs because the thiol groups bind strongly to lead chalcogenide QDs[67, 121]. Previous FET experiments have shown a good electron conductivity[114] leading to the assumption that it must be the CB of the QDs and the LUMO of the linker molecule that couples. Electrochemical experiments and theoretical calculations show however that the LUMO is too far away from the CB edge to make this possible. In further experiments, another state in the organic semiconductor is observed that apparently plays a big part in the COIN conductance.

In the work of André et al.[114] only the final thiol form of the semiconductor is investigated. Additional information about the acetylated precursor of that molecule is shown here. Despite the protection of the binding thiol group, it also leads to conductive COIN films in ECG experiments. However, the films do not show conductivity in FET experiments.

10.3.2 Experimental

All electrochemical experiments in this chapter are performed in acetone/TBAHFP (0.1 M) electrolyte. T3DSH and T3DSAc are dissolved in the electrolyte. A platinum wire is used as CE, a silver wire as pseudo RE and a GC electrode as WE. The recording speed is chosen to be 0.1 V/s and the cathodic direction is recorded first. The setup is placed inside a Faraday cage in a nitrogen filled glovebox.

For UV-Vis measurements, the substances are dissolved in acetone and measured in a quartz cuvette in a Cary 5000 spectrophotometer.

For SE measurements, a home-built transparent electrochemical cell is fitted into the same spectrometer. The reference channel is left unfilled and a baseline of the cell with FTO WE and the pure electrolyte is recorded.

FTIR measurements are performed in a Bruker Vertex 70v and a Vertex 70 spectrometer. The linker molecules are dropcasted from a concentrated solution in acetone on a KBr window. The QDs are dropcasted from hexane on a KBr window. The COIN film is prepared by a dipcoating procedure similar to the one described in **Chapter 10.1.2**. The substrate is first immersed into a solution of the QDs in hexane for 30

seconds. After the hexane is evaporated, it is dipped into a saturated solution of the linker molecule in acetone for 30 seconds and then in pure acetone for another 60 seconds to get rid of excess ligands. This procedure is repeated 10 times. The same dipcoating procedure is used to fabricate the COIN films on the IDEs for ECG measurements. The sample with PbS QDs and their native ligands for ECG measurements is prepared by dropcasting a solution of PbS QDs in hexane on the IDE (~ 10 µL). Prior to applying the QD films, the IDE is rinsed with acetone to clean it.

Quantum chemical calculations are performed to back up the experimental results obtained on the linker molecules by CV measurements. The calculation methods are based on the work on thiophenes by Kölle et al.[163]. Details on the geometry and basis set can be found in the work of André et al.[114].

All electrochemical experiments and the FTIR measurement on the Vertex 70 spectrometer are performed by me. Theoretical calculations, all FTIR measurements on the Vertex 70v spectrometer and the deprotonation experiment on T3DSH are performed by Alexander André.

10.3.3 Results

10.3.3.1 Characterization of the Linker Molecules

In order to learn more about their electronic structure, both T3DSH with free thiol groups as well as its acetylated precursor T3DSAc are investigated by CV.

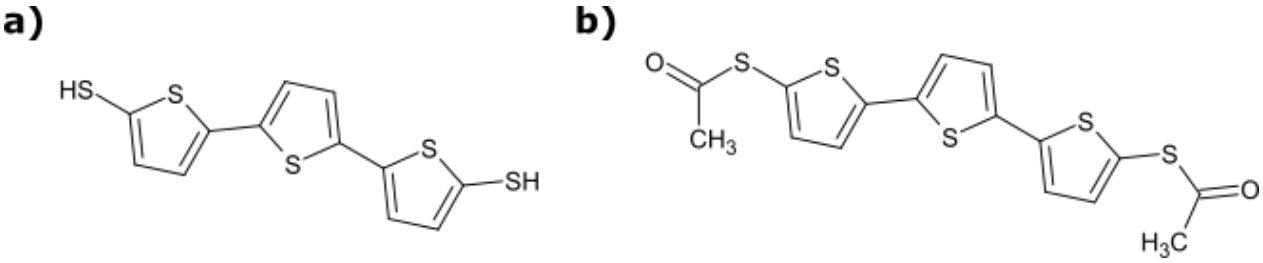

Figure 41: Structural formula of the ligands used in this study: a) T3DSH and b) T3DSAc.

The CV curves of the protected and unprotected molecule look similar with some shared peaks and some peaks shifted to slightly different potentials (**Figure 42**). Peak 1 is more distinct for the protected molecule. Its two subpeaks are closer together and shifted towards more oxidative potentials. Peak 2 is almost identical for both analytes, as is also shown in the inset. Peak 3 is again shifted towards higher potentials for the protected molecule, while the position of Peak 4 is almost identical for both molecules.

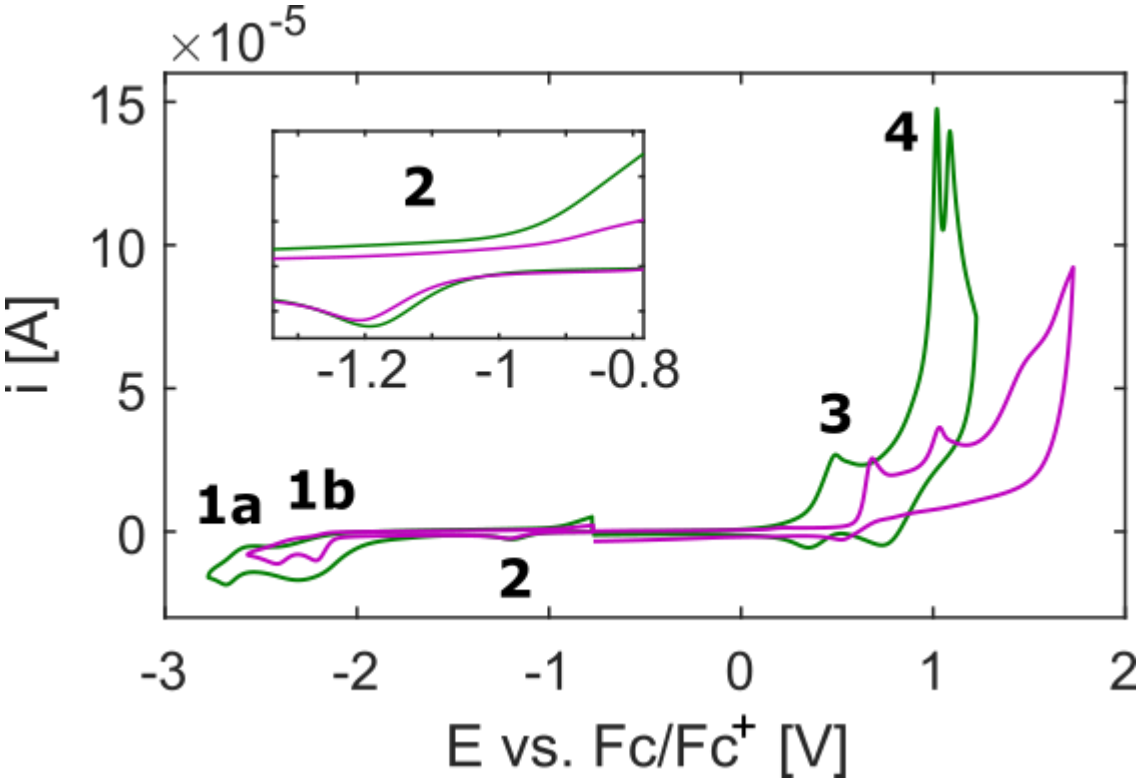

Figure 42: CV of T3DSH and T3DSAc acetone/TBAHFP (0.1 M).
Green: terthiophene with open SH groups (T3DSH). Purple: acetylated form (T3DSAc). Inset: common peak around -1.2 V vs. Fc/Fc^+.

The values for the peaks shown in **Figure 42** are summarized in the table below:

Table 9: Summary of the measured electrochemical potentials for T3DSH and T3DSAc.

	T3DSH		**T3DSAc**	
Peak #	vs. Fc/Fc^+	vs. Vac	vs. Fc/Fc^+	vs. Vac
1a	-2.62	-2.18	-2.37	-2.43
1b	-2.27	-2.53	-2.18	-2.62
2	-1.20	-3.60	-1.20	-3.60
3	0.42	-5.22	0.60	-5.40
4	0.88	-5.68	1.00	-5.80

The electrochemical potentials measured by CV are a good starting point to investigate the electronic structure of the linker molecules. It is however not possible to link an electrochemical potential to an electronic level of the analyte without additional information. Therefore, spectroscopic and SE experiments are conducted with both substances.

A peak at 370 nm for T3DSH and a peak at 380 nm for T3DSAc can be observed (**Figure 43a**) in a UV-Vis absorption spectrum. This corresponds to an optical band gap of 3.35 eV for T3DSH and 3.26 eV for T3DSAc.

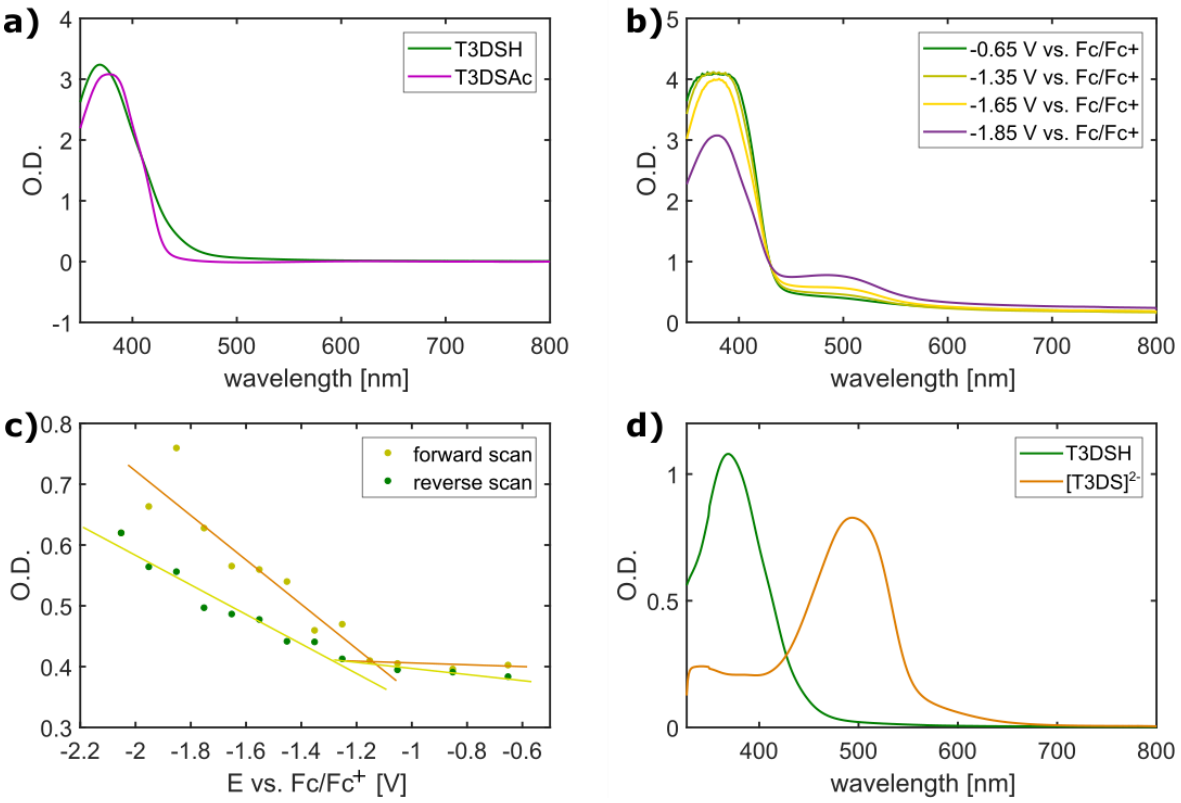

Figure 43: Spectroscopic measurements of T3DSH and T3DSAc. a) Spectra of the pure analytes in acetone. The spectra are normalized to show a similar intensity. b) SE dataset of T3DSH. c) Voltabsorptogram of T3DSH at 500 nm, plotted with the same dataset as used in b. The yellow and orange lines are the linear fit. d) Spectra of the protonated (green curve) and deprotonated (orange curve) form of T3DSH, both dissolved in acetone.

In an SE experiment, a polarization of the FTO working electrode with increasingly negative potentials leads to the formation of a peak at 500 nm for T3DSH (**Figure 43b**) while the peak at 370 nm decreases at the same time. In order to better visualize the dependence of this peak at 500 nm on the electrochemical potential, the same dataset is plotted as a voltabsorptogram (**Figure 43c**). Therefore, the optical density of all data points recorded at 500 nm is plotted against the corresponding electrochemical potential. It can be observed that upon polarizing the electrode with increasingly reductive potentials, the optical density at 500 nm stays nearly constant up to a potential of -1.2 V vs. Fc/Fc^+. From there it increases linearly till the end of the experiment at -2 V vs. Fc/Fc^+. When moving the potential back to the OCP, the optical density at 500 nm decreases linearly till a potential of -1.2 V vs. Fc/Fc^+, from where on it stays constant.

A sample of T3DSAc is cleaved with NaOH according to the synthesis procedure[114] described in **Chapter 9.1.1** to yield the doubly deprotonated form of T3DSH (from now on denoted as $[T3DS]^{2-}$). A spectrum of this compound is taken and a peak at 495 nm can be observed (**Figure 43d**).

Positive polarization of a solution of T3DSH in acetone/TBAHFP leads to a general decrease in absorbance and the formation of a film of yellow solid on the working electrode at a potential of roughly 0.4 V vs. Fc/Fc^+. Neither negative nor positive potentials lead to any changes in the spectrum of T3DSAc.

10.3.3.2 Characterization of the QDs

The PbS QDs used in this study are the same as the medium large PbS QDs used in **Chapter 10.2.3** where their electrochemical characterization is thoroughly discussed.

10.3.3.3 Characterization of the COIN Films

To investigate the quality of the chemical coupling between the QDs and linkers, FTIR spectroscopy is conducted.

In the spectrum of pure T3DSAc (**Figure 44a1**), aromatic C-C vibrations coming from the terthiophene rings can be seen in the fingerprint region. The C=O vibrations, resulting from the acetyl-group, are shown at 1700 cm^{-1}. An S-H vibration can be seen at 2500 cm^{-1} and aromatic C-H vibrations from the terthiophene rings are observed at 3100 cm^{-1}.

In the spectrum for the film of PbS QDs interlinked with T3DSAc (**Figure 44a2**), the C=O vibrations have almost vanished, the S-H vibration is gone completely. The signal for aromatic C-H vibrations gets a bit stronger.

In the spectrum of the PbS QDs with native OA ligands (**Figure 44a3**), none of those peaks can be seen. There is an absorption between 2800 and 3000 cm^{-1} which comes from aliphatic C-H vibrations that can be observed in all three spectra.

In the FTIR spectrum of pure T3DSH (**Figure 44b1**), aromatic C-C vibrations coming from the terthiophene rings can be seen in the fingerprint region. An S-H vibration can be seen at 2500 cm^{-1} and aromatic C-H vibrations from the terthiophene rings are observed at 3100 cm^{-1}. There are very weak peaks in the region of the aliphatic C-H vibrations between 2800 and 3000 cm^{-1}.

In the spectrum of the QD film interlinked with T3DSH (**Figure 44b2**), the peak for the S-H vibrations is completely gone. There are some significant peaks in the region of the aliphatic C-H vibrations between 2800 and 3000 cm^{-1} and the peak for the aromatic C-H vibrations coming from the terthiophene ring has become stronger.

The spectrum for the PbS QDs with their native OA ligands (**Figure 44b3**) shows even stronger peaks in the region of the aliphatic C-H vibrations between 2800 and 3000 cm^{-1} and no peaks for aromatic C-H vibrations[164].

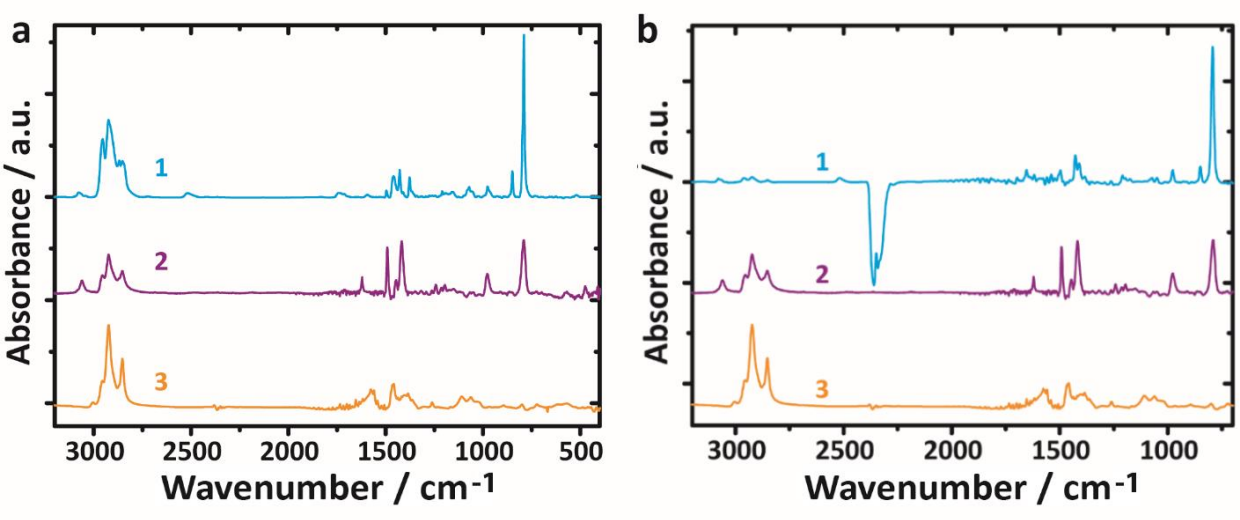

Figure 44: FTIR spectroscopy is used to investigate the quality of ligand exchange in PbS based COINs. a) FTIR spectrum of (1) the pure T3DSAc molecule. (2) PbS QDs functionalized with T3DSAc and (3) PbS QDs functionalized with OA. b) FTIR spectrum of (1) the pure T3DSH molecule. (2) PbS QDs functionalized with T3DSH and (3) PbS QDs functionalized with OA.

ECG experiments are performed on three different samples: a dropcasted film of PbS QDs with their native OA ligand shell (grey curves in **Figure 45**), a dipcoated film of PbS QDs interlinked with T3DSH (green curves in **Figure 45**) and a dipcoated film of PbS QDs interlinked with T3DSAc (purple curves in **Figure 45**).

Upon slowly moving to more reductive potentials, both COIN samples (PbS with T3DSH and PbS with T3DSAc as linker) show an increase of conductance at -1.2 V vs. Fc/Fc^+ (**Figure 45a**). The sample with PbS and OA shows a less steep increase at a potential of -1.2 V vs. Fc/Fc^+ and reaches a quarter of the conductance observed for PbS with T3DSAc.

The accumulated charge has a similar shape for all films with a rather flat region at a potential above -1.2 V vs. Fc/Fc^+ and an increase of charge accumulation for potentials below -1.2 V vs. Fc/Fc^+. The curve for PbS with T3DSAc shows almost no hysteresis, while the curve for PbS with OA ligands shows the highest hysteresis. This curve also shows a higher overall charge accumulation than the curve of the COIN films (**Figure 45b**).

The charge carrier mobility shows a maximum for both COIN films at -1.2 V vs. Fc/Fc^+. For the film with T3DSAc, it is about twice as high as the curve of the film with T3DSH. The film with PbS and oleic acid shows an order of magnitude lower charge carrier mobility (**Figure 45c**).

Experiments with the film using T3DSAc can be repeated more often without showing signs of film degradation (like a reduction of conductance and an increase of measurement outliers).

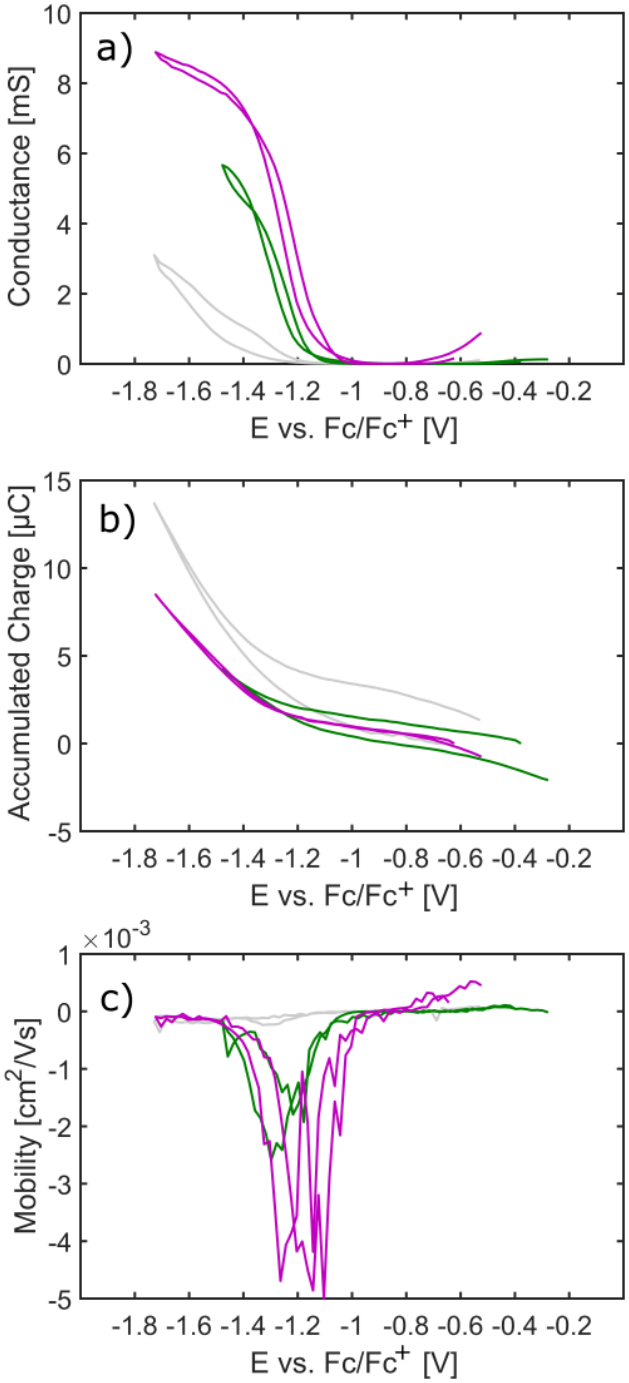

Figure 45: ECG measurements of a COIN film prepared from PbS QDs with T3DSH and T3DSAc.
a) Plot of the steady-state conductance, b) plot of the accumulated charge and c) plot of the charge carrier mobility. COINs interlinked with T3DSH are shown by a green curve, COINs interlinked with T3DSAc are shown as a purple curve and PbS QDs with their native OA ligands are shown as a grey curve.

10.3.4 Discussion

10.3.4.1 Chemical Coupling of the COIN Films

FTIR measurements of pure T3DSAc (**Figure 44a1**) show all the expected peaks for this molecule with aromatic C-H vibrations from the rings, C=O vibrations and aliphatic C-H

vibrations from the acetyl group. Additionally, S-H vibrations can be seen that can be interpreted with the presence of some deprotected S-H groups.

The COIN film with T3DSAc (**Figure 44a2**) does not show these S-H vibrations any more, giving rise to the idea that they are bound to the QDs. The decrease of the C=O peak in the COIN film could also mean that uncleaved thioesters have attached to the QDs via the acetyl-oxygen.

The spectrum of the pure QDs (**Figure 44a3**) is expectedly free of all aromatic C-H vibrations, S-H and C=O vibrations as it only contains PbS QDs and OA ligands. Aliphatic C-H vibrations can be found in all three spectra. They result from the acetyl group in the spectrum of pure T3DSAc, from a mixture of acetyl groups and remaining OA ligands in the COIN spectrum and exclusively from OA in the QD spectrum.

The spectrum of pure T3DSH (**Figure 44b1**) has to be recorded in a different spectrometer (a Bruker Vertex 70) under atmospheric conditions because of technical problems with the other spectrometer. The spectrometer in which all other spectra are recorded (a Vertex 70v) can be flushed with nitrogen. It can be assumed however that the only difference between the spectra is the presence of a peak at 2400 cm^{-1} that results from atmospherical carbon dioxide. In the FTIR spectrum, all the expected peaks for this molecule with aromatic C-H vibrations from the rings and S-H vibrations from the thiol group can be seen. There are some very weak aliphatic C-H vibrations, which can be attributed to traces of leftover acetate in the sample.

In the spectra of the COIN film (**Figure 44b2**), the peaks of the S-H vibrations are gone, which indicates that the molecules are probably bound to the QDs via the thio-groups. The aliphatic C-H vibrations in this spectrum come from the OA ligands of the QDs that are not fully removed during ligand exchange. They are however stronger in the spectrum of pure QDs (**Figure 44b3**) as there are more OA ligands present in that film.

It can therefore be concluded that the ligand exchange is successful, but not quantitative in both COIN films.

10.3.4.2 Electronic Coupling of the COIN Films

ECG experiments reveal a low intrinsic conductance of the sample with pure PbS QDs. Conductance of the films interlinked with the terthiophene linkers is 4-5 times higher. The conductance of the COIN films starts to increase at a potential of -1.2 V vs. Fc/Fc^+ (3.6 eV vs. Vac) which means that the film is not conductive below this energetic level. The conductance of the film does not occur over the VB of the QDs and the HOMO of the molecules, as already suspected from the discrepancy of their energetic positions. It rather goes over the CB of the QDs and the state at peak 2 from the linker molecules' CV measurements.

The accumulated charge reveals quite a big hysteresis for the film without terthiophene linkers. Apparently, more charge is extracted from the film than it is charged with. This leads to the assumption that the film with OA ligands is less stable under the experimental conditions. The reason for this is most likely that the divalent terthiophene linkers increase the mechanical stability of the film and avoid that particles get charged and then detach from the film. The least hysteresis is shown for the film interlinked with T3DSAc, which is counterintuitive because the free thiol groups of the T3DSH molecule are expected to bind much stronger to the QDs than the thioester groups with the occasional free thiol group in the T3DSAc sample.

The sample with PbS particles and their native ligands shows almost no mobility. This is unsurprising when looking at the graphs recorded for conductance and accumulated charge for this sample. To calculate the mobility, the conductance goes into the numerator of **Equation 15** and the accumulated charge in the denominator. If the conductance is smaller than that for the COIN films and the accumulated charge is larger, then the mobility becomes a lot smaller. It is also in line with the expectation that the isolating OA ligands hamper the movement of charges in the film more than the semiconducting terthiophene ligands do. The samples interlinked with T3DSH and T3DSAc show a peak in the mobility at -1.2 V vs. Fc/Fc^+ which backs the assumption that charge carriers go over the level of CV peak 2.

When comparing the CV data with theoretical calculations, it can be said that peak 1 (**Figure 42**) is in reasonably good agreement with the calculated LUMO. Peak 1b better fits the calculated LUMO value for T3DSH and peak 1a better fits the calculated LUMO value for T3DSAc. The calculated HOMO values are in good agreement with the CV values of peak 4.

When calculating the band gap from the theoretical values, a value of 3.43 eV for T3DSH and 3.44 eV for T3DSAc is predicted. This band gap is a bit wider than the spectroscopically measured band gaps of 3.35 eV for T3DSH and 3.26 eV for T3DSAc, which makes sense because the optical band gap also takes the polarization energy into account and the calculated values represent the electronic transport band gap.

When using experimental data and taking peak 1b to be the LUMO, an electronic transport band gap of 3.15 eV can be calculated for T3DSH. Using peak 1a as the LUMO would lead to a band gap of 3.50 eV. It makes therefore more sense to assume peak 1a as the LUMO, as this leads to a larger electronic band gap than optical band gap. The same holds true for T3DSAc, where the band gap with peak 1b as the LUMO would be 3.18 eV and with peak 1a it would be 3.37 eV. The theoretically calculated values, as well as the measured values, for the terthiophene frontier orbitals are summarized in **Table 10**. For the CV data, the peak number is added in brackets.

The values for the HOMO of T3DSH and T3DSAc reported in the literature[165] (5.58 V and 5.50 V vs. Vac respectively) are located between peaks 3 and 4 in the CV measurements performed in this study. It has to be kept in mind that the values

measured in the study conducted by DeBoer et al.[165] are measured in dichloromethane as solvent and T3DSH is attached to the electrode as a monolayer. As already discussed in **Chapter 10.2.3.2,** the solvent can cause shifts in electrochemical potentials. Since peak 3 is assumed to be linked to the oxidation of the sulfur atom (as will be described later), based on SE experiments and peak 4 fits quite well the theoretical predictions which use acetone as the solvent, it is likely that peak 4 is actually the HOMO of the linker molecules.

Table 10: Theoretical and measured values for the HOMO and LUMO of T3DSH and T3DSAc. Peak numbers as in **Figure 42** are denoted in brackets.

Method	**Calculated**	**CV**	**Calculated**	**CV**
Molecule	T3DSH	T3DSH	T3DSAc	T3DSAc
HOMO	5.92	5.68 (4)	5.89	5.80 (4)
LUMO	2.49	2.18 (1a)	2.45	2.43 (1a)

Both T3DSH and T3DSAc show a CV peak at -1.2 V vs. Fc/Fc^+ (-3.6 vs. Vac) (peak 2). This peak cannot be linked to any quantum chemical level of the organic semiconductor, but must still have a real meaning for the investigated system as it is also the potential at which the conductance of the material increases and the charge carrier mobility has its maximum. Spectroelectrochemical measurements of T3DSH reveal that at this potential of -1.2 V vs. Fc/Fc^+ the absorption peak at 380 nm decreases and a peak at 495 nm emerges. It is also shown that when T3DSH gets deprotonated, the peak at 380 nm vanishes and is replaced by a peak at 495 nm. It can therefore be concluded that the T3DSH molecule most likely shows a deprotonation reaction at – 1.2 V vs. Fc/Fc^+.

Cathode: $T3DSH + 2\ e^- \rightarrow [T3DS]^{2-} + 2\ H\cdot$ (31)

Given that the measurements are all carried out in acetone as solvent and no bubbles can be observed, it can be hypothesized that the two hydrogens reduce the surrounding acetone to isopropanol.

Calculations of the molecule symmetry with the complete active space self-consistent field (CASSCF) method reveal that in the neutral state, the T3DSH molecule exists in a slightly twisted C_2 or C_S conformation (**Figure 46a**+**b** respectively), while the deprotonated molecule moves into a planar C_{2V} conformation[114] (**Figure 46c**+**d**).

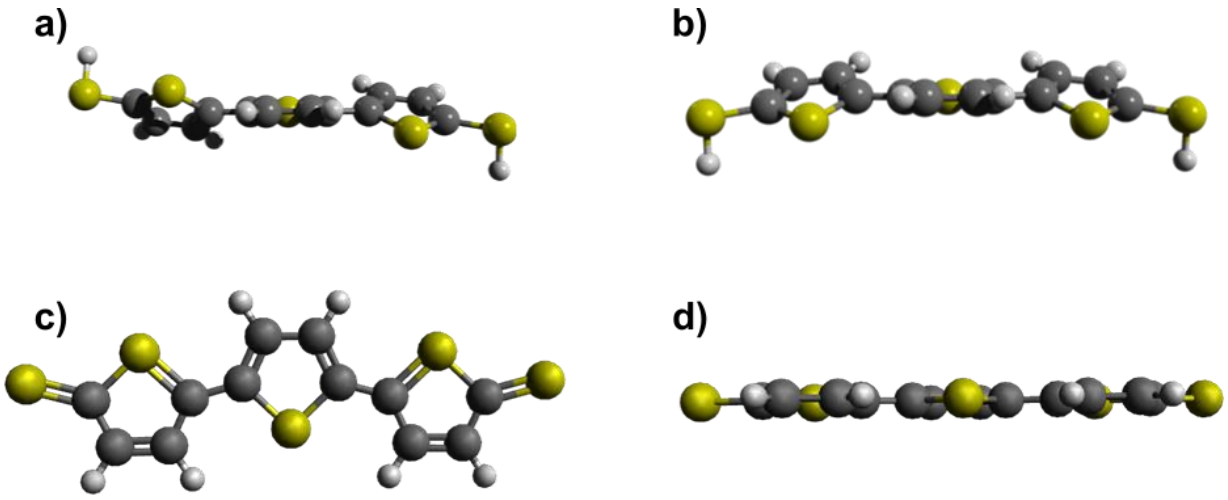

Figure 46: Molecule symmetry of T3DSH and $T3DS^{2-}$ modelled with the CASSCF method.
a) T3DSH in C_2 conformation. b) T3DSH in C_S conformation. c) $T3DS^{2-}$ in C_{2V} conformation (top view).
d) $T3DS^{2-}$ in C_{2V} conformation (side view).

It can be speculated that the flat conformation of the linker molecules leads to a better transfer of electrons through a better spatial alignment of the π-orbitals.

At this point it is worth mentioning that the protected form T3DSAc also shows the CV peak at -1.2 V, but does not undergo any visible changes in SE measurements. Yet the COIN film using T3DSAc as linker still shows an increase in conductance and mobility at that potential. A possible explanation is that the peak in the CV does not directly show the deprotonation, but the conformation change of the molecule that accompanies the deprotonation.

Spectroelectrochemical investigations of T3DSH also show that upon positive polarization, the absorption decreases for potentials more positive than 0.4 V vs. Fc/Fc^+ and a yellow/orange solid is found on the electrode after the experiment. This irreversible change occurring at the potential of peak 3 is most likely linked to the polymerization of the T3DSH molecules through forming disulfide bridges. The presence of peak 3 in the CV of T3DSAc, which does not undergo polymerization, gives rise to the assumption that the peak actually stands for the oxidation of the sulfur atoms from oxidation state -2 to -1, which is a reaction that can happen in both molecules.

When plotting the measured and calculated energy levels of the linker molecules together with the measured and calculated[166] energy levels for VB and CB edge of the QDs, it becomes apparent that the molecule's HOMO is not well aligned with the QD's VB edge (black lines in **Figure 47**). The QD's CB edge is however in quite good agreement with CV peak 2 (yellow lines in **Figure 47**) at -3.6 eV on the absolute vacuum scale. This is the energetic level over which the charge carrier transport occurs and that therefore contributes the most to the film conductance according to ECG measurements. The linker molecule's LUMO levels (dark grey lines in **Figure 47**) are way too far from the CB

edge of the QDs to lead to any energetic coupling. Peak 3 in the CVs (green lines in **Figure 47**) is assumed to be linked to the oxidation of the sulfur atom.

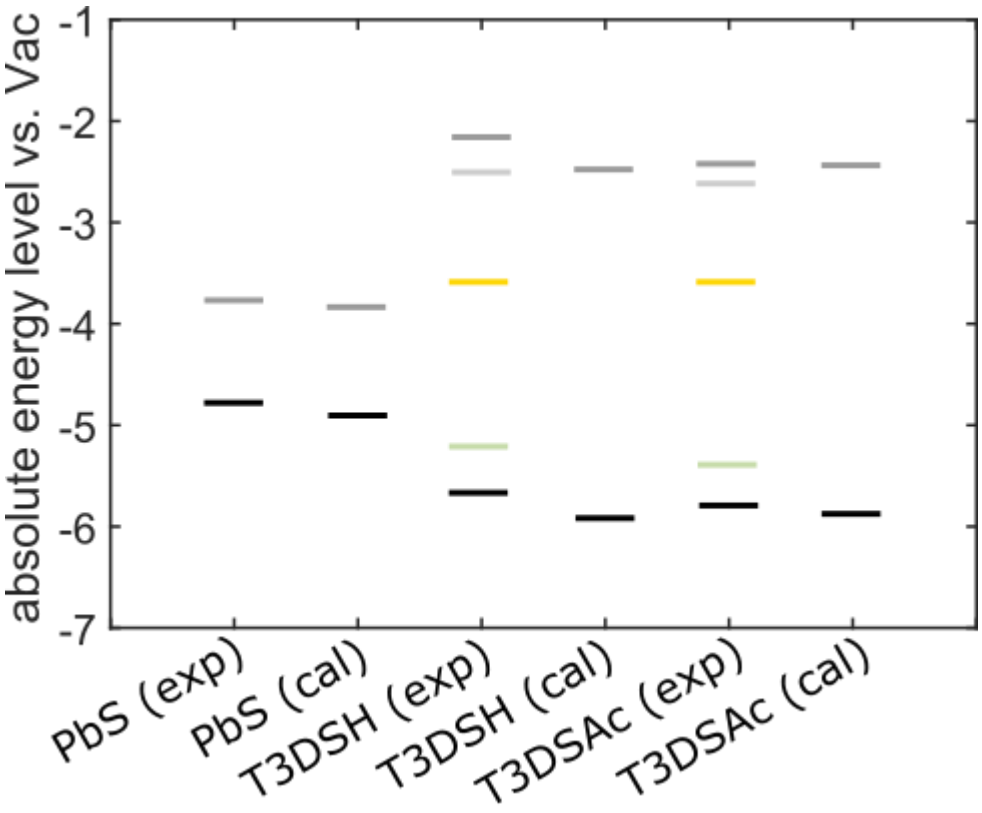

Figure 47: Measured and calculated energy levels of the linker molecules together with the measured and calculated energy levels for the VB and CB edge of the QDs.
The black lines indicate the QD VB and the linker HOMO, the two green lines indicate the position of CV peak 3, which is most likely linked to the oxidation of the S atom. The yellow lines indicate the position of CV peak 2 which is most likely linked to a conformation change in the linker molecule. The grey lines indicate the QD CB and the linker LUMO (peaks 1a, dark grey and 1b, light grey, in the case of the linkers).

10.3.5 Conclusion

It can be concluded that interlinking PbS QDs with semiconducting T3DSH or T3DSAc molecules leads to chemical and electronical coupling between these materials. Electron mobility in the COIN film is about an order of magnitude higher than in the QD film with its native OA ligands. The majority charge transport occurs over the QD 1 S_e state and a suitable energy level in the linker molecules. This level can be linked to a conformation change in the linker molecules and likely leads to a better alignment of the π-orbitals of the aromatic terthiophene rings.

11Final Conclusions

An approach to increasing the conductivity of QD films is to link the particles with multivalent organic semiconductor molecules. Ideally, the film not only gets mechanically more stable through chemically connecting the particles, but also shows increased electronic conductance. The conductance is thought to be enhanced by the electronic coupling of the frontier orbitals in the QD's VB and CB with the organic semiconductor's HOMO and LUMO.

In the three experimental chapters of this work, three different systems are introduced and investigated with a number of electrochemical and spectroscopic methods.

$Cu_{1.1}S$ nanoplatelets interlinked with CuPc show some interesting properties in the reductive regime of the ECG measurements. The typically observed behavior of losing their conductive properties when reduced is lost when applying even more reductive potentials. By holding the film at -1.77 V vs. Fc/Fc^+, the conductivity starts to rise and reaches original levels. However, this behavior is more likely to be attributed to the increased mechanical stability of the film interlinked with CuPc than to any electronic coupling of the QDs with the organic semiconductors.

DPV experiments on COIN films based on PbS QDs interlinked with a number of different metal phthalocyanines show only one peak in the oxidative regime which is an indication of an overlap of the QD VB and the MePc HOMO. Coupling of these states is likely as shown by previous work in our group[68].

CdSe based COIN films interlinked with MePcs show an interaction of the QD CB with the MePc LUMO. DPV and EMAS experiments show that linking the QDs with CoPc or H_2Pc leads to a broadening and lowering of the CB, while linking them with ZnPc does not.

The conductance of PbS films is significantly increased when being interlinked with the terthiophene derivatives T3DSH and T3DSAc. ECG experiments show that the QDs couple electronically with their linker molecules and that the majority of the charge carrier mobility goes over an electronic state that is associated with the QD CB. It is however not the linker molecule's LUMO that couples with the QDs. The energy level at which the conductance increases, is rather linked to a conformation change in the linker molecule, most likely aligning the π-bonds of the aromatic molecule in a way that charge carrier transport from one QD to the next is facilitated.

Overall, it cannot be said that an energetic proximity of the frontier orbitals of the QDs and linkers automatically leads to an electronic coupling. That is something that has to be investigated for each system. Electrochemistry offers a powerful toolbox for these investigations.

12Next Steps

A defining characteristic of scientific research is that answering one question often opens up a few new ones. This is not different in this work.

The phenomenon of increasing electronic conductance in $Cu_{1.1}S$ films upon reduction is not only new, but also poorly understood. The theory that elemental copper is formed at highly reductive potentials has to be backed up by additional experiments. It is possible to determine a material's oxidation state by XPS, so experiments with this technique will probably shed some light on this question.

EMAS experiments helped to get a better understanding of the CB band position in CdSe based COIN films. The same would also help understand the PbS based COIN films better. It is however challenging to measure EMAS with PbS since their exitonic absorption maximum is located in the NIR region where also common electrolyte solvents show increased spectral absorption. A different solvent or a thinner electrochemical cell will solve that challenge.

Repeating the EMAS experiments is advisable to increase the statistical basis for data analysis. It is also advisable to conduct these experiments with thinner COIN films to eliminate the effects of inhomogeneous films charging on the results and make them easier and less ambiguous to analyze.

Finally, it would be very interesting to investigate the CdSe films interlinked with MePc linkers with ECG. The interaction of the MePc linkers with the QD CB looks very promising in terms of orbital coupling and probably leads to increased film conductance over that level.

13Acknowledgements

I think it is quite evident that a work like this can never be achieved by one person alone. For this reason, I would like to take the opportunity to thank all the people and institutions who contributed.

I would like to start by thanking those who enabled this thesis in the first place by providing the financial means: the DFG excellence initiative “Zukunftskonzepte” and the DFG grant SCHE1905/3.

I am much indebted to Dr. Marcus Scheele, for not only hiring me and giving me the opportunity to work on this project, but also his continued scientific support.

Many thanks go also to Dr. Wolfgang Langer who was a great help with the paperwork associated with my work contract and admission as a PhD student.

I also want to thank Prof. Dr. Bernd Speiser for very fruitful discussions about electrochemistry, a subject I had no knowledge of prior to starting the work on this thesis. In the same way, I also want to thank Simon Schundelmaier for answering all the more or less intelligent questions about the basics of electrochemistry.

A big thank you has to go to Dr. Kai Braun, who contributed with his knowledge about electronics a big part to the timely commissioning of the EMAS setup. Without him, it would have taken me a lot longer. I also want to mention Daniel Spittel and Walter Schaal whose expertise helped a lot with the trouble shooting on that setup.

Many thanks have to also go to Björn Märker who synthesized the CdSe particles used in **Chapter 10.2** and prepared the EMAS samples. Thanks also to Sophia Westendorf who conducted most of the DPV measurements in this chapter.

I want to thank my colleague Dr. Alexander André for the theoretical calculations in **Chapter 10.3** as well as his generally helpful ways and his motivational speeches that I really appreciated. Talking about the same chapter, I also want to mention the work Kai Wurst put into synthesizing the terthiophene linkers. I also want to thank Markus Katzenmeyer for synthesizing the phathalocyanine linkers.

At this point I also have to thank Jan Hagenlocher who taught me the basics of MatLAB and thereby set the foundation for my ongoing enthusiasm about programming. Without that, it would have been a nightmare to analyze the data generated in this project. I also want to thank Dr. Frank Wackenhut for his support with any problems I encountered with writing my MatLAB scripts.

Also the competent support of the glass workshop as well as the mechanical workshop should not go unmentioned. Without the dedication and precision craftwork of the workshop crews, none of the setups used in this work could have been realized.

I want to thank Elke Nadler for skillfully recording of the SEM images used in this work as well as for the great discussions we had while finding the perfect image.

13 Acknowledgements

As everyone knows (at least those who did a PhD), a project like this does not only depend on funding and knowledge, but also on a human factor. Therefore, I want to thank all the members of the whatsapp group “Bierruf” (engl.: “call for beer”) for their more or less sensible ways to distract me from the worries of my every day research life.

I want to thank my parents for listening to many a Saturday morning my-life-sucks rant and for celebrating with me when my life finally started looking better.

Finally I want to thank my friends and buddies from my previous employer Procter & Gamble, especially Mike Ogden, who gave me the feeling of not being forgotten by the world while working on my PhD.

I am quite sure that I have forgotten to mention at least one person who deserves my deeply felt thankfulness. In the end, there are just too many people who helped me in the one or the other way in the course of a three and a half years of working at the University of Tuebingen.

14Appendix

14.1MatLAB Scripts

14.1.1 Ferrocene Calculator

This script is used to analyze a CV curve recorded for ferrocene. It reads in the raw data. finds the maximum of the oxidative and reductive current and reports the mean value for the associated potentials (the half-wave potential).

```
clear % deletes all previous data from the MatLAB workspace

list0=dir; % takes all files in the directory and puts them in a MatLAB
structure
list1={list0.name}; % new list with just file names
index0=strfind(list1, '.txt'); % looks for text-files
index1=~cellfun(@isempty,index0); % logical vector with 1 if file in index0
is .txt and 0 if not
list2=list1(index1); % creates list with just the .txt files
[Selection]=listdlg('PromptString','Select
files:','SelectionMode','multiple','ListString',list2); % opens the
selection windows
file_names=list2(Selection); % contains the selected files

results_pot=zeros(4,numel(file_names)); % creates a placeholder results
matrix

for k=1:numel(file_names) % runs stepwise from 1 to 'number of files'

% extracts data:

    name=cell2mat(file_names(k)); % extracts the file name from the list
    data=importdata(name,'.'); % imports the contents of the .txt file
    data_cell=struct2cell(data); % converts the data from structure to cell
    format
    data_mat=cell2mat(data_cell(1)); % converts the data from cell to
matrix
    format
    pot=(data_mat(:,1)); % specifies that the data found in the first
column
    is the potential
    cur=(data_mat(:,2)); % specifies that the data found in the second
column
    is the current

% finds current maximum and minium:

    [~,I]=max(cur); % indexes the position of the vector where the current
has
    its maximum
    [~,J]=min(cur); % indexes the position of the vector where the current
has
    its minimum

    max_pot=pot(I); % finds the potential that corresponds to the maximal
    current
```

```
    min_pot=pot(J); % finds the potential that corresponds to the minimal
    current
    delta=(min_pot-max_pot)*1000; % calculates the difference between the
    potential of the maximal and the potential of the minimal current
    mean=(min_pot+max_pot)/2; % calculates the half-wave potential

    results_pot(1,k)=min_pot; % writes potential at current minimum into
    results matrix
    results_pot(2,k)=max_pot; % writes potential at current maximum into
    results matrix
    results_pot(3,k)=delta; % writes peak spacing into results matrix
    results_pot(4,k)=mean; % writes half-wave potential into results matrix

% plots data:

    plot(pot,cur)
    hold on

end

xlabel('E [V]') % labels the x-axis
ylabel('i [A]') % labels the y-axis
legend(file_names) % adds the legend

saveas(gcf,'plot Fc.fig') % saves the figure as MatLAB figure
saveas(gcf,'plot Fc.jpg') % saves the figure as .jpg file
dlmwrite('results_Fc.txt',results_pot) % saves the results matrix as .txt
file
```

14.1.2 DPV Script

This script is used to analyze DPV data and label the peaks with their respective peak potential.

```
clear % deletes all previous data from the MatLAB workspace

list0=dir; % takes all files in the directory and puts them in a MatLAB
structure
list1={list0.name}; % new list with just file names
index0=strfind(list1, '.txt'); % looks for text-files
index1=~cellfun(@isempty,index0); % logical vector with 1 if file in index0
is .txt and 0 if not
list2=list1(index1); % creates list with just the .txt files
[Selection]=listdlg('PromptString','Select
files:','SelectionMode','multiple','ListString',list2); % opens the
selection windows
file_name=list2(Selection); % contains the selected files

Fc = 0.3065; % ferrocene half-wave potential. to be entered manually from
the result of Script 14.1.1

for k=1:numel(file_name) % runs stepwise from 1 to 'number of files'

% extracts data:
```

```
    name_rawdata = cell2mat(file_name(k)); % extracts the file name from
the
    list
    struct_rawdata = importdata(name_rawdata,','); % imports the contents
of
    the .txt file
    cell_rawdata = struct2cell(struct_rawdata); % converts the data from
    structure to cell format
    mat_rawdata = cell_rawdata[111]; % converts the data from cell to
matrix
    format

    x_raw = mat_rawdata(:,1); % specifies that the data found in the first
column are the x-values
    y = mat_rawdata(:,2); % specifies that the data found in the second
column are the y-values
    x = x_raw - Fc; % references the x-scale to the half-wave potential of
the ferrocene/ferrocenium couple

% plots data:

    plot(x,y)
    hold on

end


xlabel ('E vs. Fc/Fc+ [V]') % labels the x-axis
ylabel ('i [A]') % labels the y-axis
legend (file_name) % adds the legend


% finds and labels peaks:

[pks,locs,w,p] = findpeaks(smooth(y))
plot(x(locs),pks,'xr')
text(x(locs),pks,num2str(x(locs)))

hold off
```

14.1.3 ECG Script

This script is used to analyze the cyclovoltammetry and chronoamperometry experiments conducted during an ECG run and calculate the conductance, differential capacitance, charge, accumulated charge and charge carrier mobility.

```
clear % deletes all previous data from the MatLAB workspace

list0=dir; % takes all files in the directory and puts them in a MatLAB
structure
list1={list0.name}; % new list with just file names
index0=strfind(list1, '.txt'); % looks for text-files
```

```
index1=~cellfun(@isempty,index0); % logical vector with 1 if file in index0
is .txt and 0 if not
list2=list1(index1); % creates list with just the .txt files
[Selection]=listdlg('PromptString','Select
files:','SelectionMode','multiple','ListString',list2); % opens the
selection windows
file_names=list2(Selection); % contains the selected files

CA_names_i=contains(file_names,'CA_name'); % checks for chronoamperometry-
files and creates logical vector
CV_names_i=contains(file_names,'CV_name'); % checks for cyclovoltammetry-
files and creates logical vector

file_names_CA=file_names(CA_names_i); % list that contains only the CA-
files
file_names_CV=file_names(CV_names_i); % list that contains only the CV-
files

% CV-data analysis:

run = 'r5-'; % manual entry of the run number. This is important to create
the meta-data files of several runs and save them in the same folder.

if numel(file_names_CV)>0 % checks if there any CV-files

    x_pot=zeros(1,numel(file_names_CV)); % empty vector to fill with x-
values
    slope=zeros(1,numel(file_names_CV)); % empty vector to fill with slope-
    values from fit

for k=1:numel(file_names_CV) % runs stepwise from 1 to 'number of CV-files'

    name_CV=cell2mat(file_names_CV(k)); % extracts the file name from the
    list
    data_CV=importdata(name_CV,','); % imports the contents of the .txt
file
    data_cell_tot_CV=struct2cell(data_CV); % converts the data from
structure
    to cell format
    data_mat_CV=cell2mat(data_cell_tot_CV(1)); % converts the data from
cell
    to matrix format
    file_number_CV=name_CV(11:13); % gets the file number

    x=data_mat_CV(:,1); % specifies that the data found in the first column
    are the x-values
    y=data_mat_CV(:,2); % specifies that the data found in the second
column
    are the y-values

    G=polyfit(x,y,1); % fits x any y data with a linear fit
    yfit=G(1)*x+G(2); % creates y-data from the fitfunction (G(1) and G(2)
are
    the Parameters)

    x_pot(k)=x(1); % saves x-data for this file
    slope(k)=G(1); % puts G(1) parameter from fit(slope of the function) in
a
    slope vector
```

```
    if k <= 50 % checks requirements for first plot

   slopes1=figure(1); % defines first plot as figure(1)
   subplot(5,10,k); % creates subplot with 5 rows and 10 columns
   subplot_title=file_number_CV; % uses file number as subplot title
   plot(x,y,'k+')
   title(subplot_title); % sets plot title
   set(gca,'TitleFontSizeMultiplier',0.7); % formats figure
   grid on % formats figure
   hold on
   plot(x,yfit,'r.-') % plots fitfunction
   set(gca,'XTickLabel',[]); % formats figure
   set(gca,'YTickLabel',[]); % formats figure

    end

    if k > 50 && k <= 100 % checks requirements for second plot
    slopes2=figure(2); % defines second plot as figure(2)
    subplot(5,10,k-50); % creates subplot with 5 rows and 10 columns
    subplot_title=file_number_CV; % uses file number as subplot title
    plot(x,y,'k+')
    title(subplot_title); % sets plot title
    set(gca,'TitleFontSizeMultiplier',0.7); % formats figure
    grid on % formats figure
    hold on
    plot(x,yfit,'r.-')
    set(gca,'XTickLabel',[]); % formats figure
    set(gca,'YTickLabel',[]); % formats figure

    end

    if k > 100 && k <= 150 % checks requirements for third plot
    slopes3=figure(3); % defines second plot as figure(2)
    subplot(5,10,k-100) % creates subplot with 5 rows and 10 columns
    subplot_title=file_number_CV; % uses file number as subplot title
    plot(x,y,'k+')
    title(subplot_title); % sets plot title
    set(gca,'TitleFontSizeMultiplier',0.7); % formats figure
    grid on % formats figure
    hold on
    plot(x,yfit,'r.-')
    set(gca,'XTickLabel',[]); % formats figure
    set(gca,'YTickLabel',[]); % formats figure

    end
end


% CA-data analysis:

if numel(file_names_CA)>0 % checks if there are any CA-files

area_vec_DC=zeros(1,numel(file_names_CA)); % creates placeholder vector for
filling differential capacitance values
area_vec_CAcorr=zeros(1,numel(file_names_CA)); % creates placeholder vector
for filling with charge values

for i=1:numel(file_names_CA) % runs stepwise from 1 to 'number of CA-files'

    name_CA=cell2mat(file_names_CA(i)); % extracts the file name from the
```

```
    list

    data_CA=importdata(name_CA,','); % imports the contents of the .txt
file
    data_cell_tot_CA=struct2cell(data_CA); % converts the data from
structure
    to cell format
    data_mat_CA=cell2mat(data_cell_tot_CA(1)); % converts the data from
cell
    to matrix format
    file_number_CA=name_CA(11:13); % gets the file number
    x=data_mat_CA(:,1); % specifies that the data found in the first column
    are the x-values
    y1=data_mat_CA(:,2); % specifies that the data found in the second
column
    are the y1-values
    y2=data_mat_CA(:,3); % specifies that the data found in the second
column
    are the y1-values

    y=y1+y2; % sums up y1 and y2 values (current of WE1 and current of WE2)
    y_CA=mean(y(200:end)); % extracts the last 200 values of the vector and
    averages them
    y_CAcorr=y-y_CA; % subtracts the average of the last 200 values from
the
    data vector (subtraction of faradaic background currents)
    y_corr=((y-y_CA)/0.02); % calculate differential capacitance (for a
0.02V
    potential step)
    area_DC=trapz(x,y_corr); % calculates area under the data curve
    area_vec_DC(i)=area_DC; % stores area in area-vector
    area_CA=trapz(x,y_CAcorr);  % calculates area under the data curve
    corrected
    area_vec_CAcorr(i)=area_CA; % stores area in area-vector

        if i <= 50 % checks requirements for first plot
        charge1=figure(4); % defines first plot as figure(4)
        subplot(5,10,i) % creates subplot with 5 rows and 10 columns
        subplot_title=file_number_CA; % uses file number as subplot title
        plot(x,y,'b-')
        title(subplot_title); % sets plot title
        set(gca,'TitleFontSizeMultiplier',0.8); % formats figure
        grid on
        set(gca,'XTickLabel',[]); % formats figure
        set(gca,'fontsize',8); % formats figure
        hold on
        end

        if i > 50 && i <= 100 % checks requirements for second plot
        charge2=figure(5); % defines second plot as figure(5)
        subplot(5,10,i-50); % creates subplot with 5 rows and 10 columns
        subplot_title=file_number_CA; % uses file number as subplot title
        plot(x,y,'b-')
        title(subplot_title); % sets plot title
        set(gca,'TitleFontSizeMultiplier',0.7); % formats figure
        grid on
        set(gca,'XTickLabel',[]); % formats figure
        set(gca,'fontsize',8); % formats figure
        hold on
        end
```

```
        if i > 100 && i <= 150 % checks requirements for third plot
        charge3=figure(6); % defines third plot as figure(5)
        subplot(5,10,i-100) % creates subplot with 5 rows and 10 columns
        subplot_title=file_number_CA; % uses file number as subplot title
        plot(x,y,'b-')
        title(subplot_title); % sets plot title
        set(gca,'TitleFontSizeMultiplier',0.7); % formats figure
        grid on
        set(gca,'XTickLabel',[]); % formats figure
        set(gca,'fontsize',8); % formats figure
        hold on
        end

end

cd ../ % goes one folder up in the folder structure of the rawdata

if k <= 50
saveas(slopes1,'Slopes1.fig') % saves the plot as MatLAB figure
end
if k > 50 && k <= 100
saveas(slopes2,'Slopes2.fig') % saves the plot as MatLAB figure
end
if k > 100 && k <= 150
saveas(slopes3,'Slopes3.fig') % saves the plot as MatLAB figure
end


if i <= 50
saveas(charge1,'Charge1.fig') % saves the plot as MatLAB figure
end
if i > 50 && i <= 100
saveas(charge2,'Charge2.fig') % saves the plot as MatLAB figure
end
if i > 100 && i <= 150
saveas(charge3,'Charge3.fig') % saves the plot as MatLAB figure
end

slope_scaled_1000 = slope*1000; % converts conductance from Siemens to
milliSiemens

% creates file-names for the conductance plots
name_figure_jpg = sprintf('%3sConductance.jpg', run);
name_figure_fig = sprintf('%3sConductance.fig', run);
name_figure_txt = sprintf('%3sConductance.txt', run);

figure(7)
    plot(x_pot,slope_scaled_1000,'k-','LineWidth',1.5) % plots the slope
    (conductance) vs. the potential
    set(gca,'LineWidth',1.5) % formats figure
    set(gca,'FontSize',16) % formats figure
    grid on % formats figure
    ylabel('Conductance [mS]') % labels the y-axis
    xlabel('E vs. Ag [V]') % labels the x-axis
    saveas(gcf,name_figure_jpg) % saves the figure as .jpg file
    saveas(gcf,name_figure_fig) % saves the figure as MatLAB figure
    dlmwrite(name_figure_txt,slope_scaled_1000) % writes the conductance
values into a .txt file
```

```
area_vec_AC=zeros(1,numel(file_names_CA)); %empty vector for filling
accumulated charge values

area_vec_AC(1)=0; % creates a placeholder value
area_vec_AC(2)=area_vec_CAcorr(1)+area_vec_CAcorr(2); % adds up the first
and second value of the accumulated charge vector

for n=2:1:numel(file_names_CA) % runs stepwise from 2 to 'number of CA-
files'
    if n+1<=numel(file_names_CA)
    area_vec_AC(n+1)=area_vec_AC(n)+area_vec_CAcorr(n+1); % integrates
charge
    end
end

% creates file-names for the charge plots:
name_figure_jpg = sprintf('%3sCharge.jpg', run);
name_figure_fig = sprintf('%3sCharge.fig', run);
name_figure_txt = sprintf('%3sCharge.txt', run);

figure(9)
    plot(x_pot,area_vec_CAcorr,'r+--','LineWidth',1.5) % plots the
    charge vs. the potential
    set(gca,'LineWidth',1.5) % formats figure
    set(gca,'FontSize',16) % formats figure
    grid on% formats figure
    ylabel('Charge [C]') % labels the y-axis
    xlabel('E vs. Ag [V]') % labels the x-axis
    hold on
    saveas(gcf,name_figure_jpg) % saves the figure as .jpg file
    saveas(gcf,name_figure_fig) % saves the figure as MatLAB figure
    dlmwrite(name_figure_txt, area_vec_CAcorr) % writes the charge
    values into a .txt file

% creates file-names for the differential capacitance plots:
name_figure_jpg = sprintf('%3sDiff Cap.jpg', run);
name_figure_fig = sprintf('%3sDiff Cap.fig', run);
name_figure_txt = sprintf('%3sDiff Cap.txt', run);

figure(10)
    plot(x_pot,area_vec_DC,'b+--','LineWidth',1.5) % plots the differential
    capacitance
    set(gca,'LineWidth',1.5) % formats figure
    set(gca,'FontSize',16) % formats figure
    grid on % formats figure
    ylabel('Differential Capacitance [C/V]') % labels the y-axis
    xlabel('E vs. Ag [V]') % labels the x-axis
    saveas(gcf,name_figure_jpg) % saves the figure as .jpg file
    saveas(gcf,name_figure_fig) % saves the figure as MatLAB figure
    dlmwrite(name_figure_txt, area_vec_DC) % writes the differential
    capacitance values into a .txt file

gapwidth=0.0005; % width of the gap between electrode in cm
gaplength=337.324; % length of channel between electrodes in cm
filmthickness=0.00001; % thickness of NP film in cm
activearea=0.5*0.7; % active area of the electrode (interdigigtated part)
in cm^2

fac_geo=gapwidth/(gaplength*filmthickness); % calculation of geometrical
factor
```

```
vol=activearea*filmthickness; % calculates NP film volume

% parital derivation of the conductance after the charge:
dG=diff(slope);
Q=area_vec_AC/vol;
dQ=diff(Q);
dGdQ=dG./dQ;
mu=dGdQ*fac_geo;
x_pot_new=x_pot(1,2:end); % shortening of the vector with the potential
values by 1. so the length of the two vectors match

% creates file-names for the charge carrier mobility plots:
name_figure_jpg = sprintf('%3sMobility.jpg', run);
name_figure_fig = sprintf('%3sMobility.fig', run);
name_figure_txt = sprintf('%3sMobility.txt', run);

figure(11)
    plot(x_pot_new,mu,'k-','LineWidth',1.5) % plots the differential
    capacitance
    set(gca,'LineWidth',1.5) % formats figure
    set(gca,'FontSize',16) % formats figure
    grid on % formats figure
    ylabel('Mobility [cm^2/Vs]') % labels the y-axis
    xlabel('E vs. Ag [V]') % labels the x-axis
    saveas(gcf,name_figure_jpg) % saves the figure as .jpg file
    saveas(gcf,name_figure_fig) % saves the figure as MatLAB figure
    dlmwrite(name_figure_txt, mu) % writes the charge carrier mobility
values
    into a .txt file

% creates file-names for the charge accumulated charge plots:
name_figure_jpg = sprintf('%3saccumulated charge.jpg', run);
name_figure_fig = sprintf('%3saccumulated charge.fig', run);
name_figure_txt = sprintf('%3saccumulated charge.txt', run);

% creates file-names for the vectors with the electrochemical potential:
name_pot2 = sprintf('%3spot_cond.txt', run);
name_pot1 = sprintf('%3spot_mob.txt', run);

area_vec_AC_scaled_1000000 = area_vec_AC*1000000; % converts accumulated
charge from Coulomb to mikroCoulomb

figure(12)
    plot(x_pot,area_vec_AC_scaled_1000000,'k-','LineWidth',1.5) % plots the
    accumulated charge
    set(gca,'LineWidth',1.5) % formats figure
    set(gca,'FontSize',16) % formats figure
    grid on % formats figure
    ylabel('accumulated charge [µC]') % labels the y-axis
    xlabel('E vs. Ag [V]') % labels the x-axis
    saveas(gcf,name_figure_jpg) % saves the figure as .jpg file
    saveas(gcf,name_figure_fig) % saves the figure as MatLAB figure
    dlmwrite(name_figure_txt, area_vec_AC_scaled_1000000) % writes the
    accumulated charge values into a .txt file

% writes the electrochemical potential into .txt files:
    dlmwrite(name_pot1,x_pot_new)
    dlmwrite(name_pot2,x_pot)
end
```

14.1.4 EMAS Script

This script is used to analyze the data collected in an EMAS experiment and plot the absorption difference.

```
clear % deletes all previous data from the MatLAB workspace

list0=dir;      % takes all files in the directory and puts them in a
MatLAB structure
list1={list0.name}; % new list with just file names
index0=strfind(list1, '.txt'); % looks for text-files
index1=~cellfun(@isempty,index0); % logical vector with 1 if file in index0
is .txt and 0 if not
list2=list1(index1); % creates list with just the .txt files
[Selection]=listdlg('PromptString','Select
files:','SelectionMode','multiple','ListString',list2); % opens the
selection windows
file_names=list2(Selection); % contains the selected files

num_WL = 71; % number of measured wavelengths (has to be entered
manually)
WL = zeros(1,num_WL); % creates an empty vector for wavelengths
num_E = 24; % number of measured potentials (has to be entered
manually)
E = zeros(1,num_E); % creates an empty cell array for potentials
Fc = -0.26; % Ferrocene half-wave potential. to be entered manually from
the result of Script 14.1.1

% creates the wavelengths vector:

for x=1:num_WL % runs stepwise from 1 to 'number of wavelengths'

    name = cell2mat(file_names(x)); % selects the xth file
    wl = str2double(name(5:7)); % reads out the wavelength from the title
of
    the file
    WL(1,x) = wl; % stores the number in a vector.

end

% creates the potentials vector:

n=1;

for y=1:num_WL:numel(file_names) % runs stepwise from 1 to 'number of
files' in steps of the number of wavelenths

    name = cell2mat(file_names(y)); % selects the yth file
    E(1,n) = str2double(name(1:4)); % reads out the potential from the
title
    of the file and stores it into a vector
    n=n+1;

end
```

```
% Converts the potentials vector into a cell array:

E_cell = cell(1,num_E);

for y=1:num_E

   E_cell{y} = num2str(E(y));

end


finaldata = zeros (numel(file_names),6); % creates empty matrix to store
processed values

extracts raw data from .txt files:

for k=1:numel(file_names) % runs stepwise from 1 to 'number of files'

    name=cell2mat(file_names(k)); % selects file
    struct=importdata(name); % imports data
    values=struct.data; % extracts data from a structure array


    n = numel(values)/3; % divides the whole data set by three (3 measured
    values: R,P,DC)

% computes the mean and standard error of the mean for each data point

    block1 = values(1:n,1); % extracts the first third of the raw data (DC)
    DC_mean = mean(block1(:,1)); % averages the DC signal
    DC_std = (std(block1(:,1)))/sqrt(n/3); % calculates the standard error
    block2 = values(n+1:2*n,1); % extracts the second third of the raw data
(Amplitude. R)
    R_mean = mean(block2(:,1)); % averages the Amplitude signal
    R_std = (std(block2(:,1)))/sqrt(n/3); % calculates the standard error
    block3 = values((2*n)+1:3*n,1); % extracts the last third of the raw
data (Phase)
    P_mean = mean(block3(:,1)); % averages the Phase signal
    P_std = (std(block3(:,1)))/sqrt(n/3); % calculates the standard error

% writes values in one central storage matrix

    finaldata(k,1) = DC_mean;
    finaldata(k,2) = DC_std;
    finaldata(k,3) = R_mean;
    finaldata(k,4) = R_std;
    finaldata(k,5) = P_mean;
    finaldata(k,6) = P_std;
end

% evaluates Phase shift (0° ind. abs./ 180° bleach):

Phase = finaldata(:,5); % extracts the phase from the central storage
matrix
Phase_sig = zeros(numel(Phase),1); % creates a placeholer phase vector

for p=1:numel(Phase) % runs stepwise from 1 to 'number of values stored for
the phase'
```

```
    if sqrt(Phase(p)^2)>= 90 % evaluates whether the phase is above 90°
(treated as "180°" = bleach)
    Phase_sig(p) = -1;
    else
    Phase_sig(p) = 1;
    end
end


R = finaldata(:,3).*Phase_sig; % multiplies the amplitude data with the
sign of the phase vector
Vpp = R*2*sqrt(2); % calculates the peak to peak amplitude


for z=num_WL:num_WL:numel(file_names) % runs stepwise from 1 to 'number of
files' in steps of the number of wavelenths

    plot1 = figure(1); % defines first plot as figure(1)
    errorbar(WL,finaldata(1+(z-num_WL):z,1),finaldata(1+(z-num_WL):z,2))
    % plots the DC data including the standard error
    hold% plots the DC signal:
 on
end

    set(gca,'LineWidth',1.5) % formats figure
    set(gca,'FontSize',16) % formats figure
    xlabel ('wavelength / nm') % labels the x-axis
    ylabel ('DC / V') % labels the y-axis
    legend(E_cell) % adds the legend

% plots the Amplitude signal:

for z=num_WL:num_WL:numel(file_names) % runs stepwise from 1 to 'number of
files' in steps of the number of wavelenths

    plot2 = figure(2); % defines second plot as figure(2)
    errorbar(WL,Vpp(1+(z-num_WL):z),finaldata(1+(z-num_WL):z,4))
    % plots the Amplitude data including the standard error
    hold on
end

    set(gca,'LineWidth',1.5) % formats figure
    set(gca,'FontSize',16) % formats figure
    xlabel ('wavelength / nm') % labels the x-axis
    ylabel ('Amplitude(Vpp) / V') % labels the y-axis
    legend(E_cell) % adds the legend

% plots the Phase signal:

for z=num_WL:num_WL:numel(file_names) % runs stepwise from 1 to 'number of
files' in steps of the number of wavelenths

    plot3 = figure(3); % defines third plot as figure(3)
    errorbar(WL,finaldata(1+(z-num_WL):z,5),finaldata(1+(z-num_WL):z,6))
    % plots the phase data including the standard error
    hold on
end
```

```
    set(gca,'LineWidth',1.5) % formats figure
    set(gca,'FontSize',16) % formats figure
    xlabel ('wavelength / nm') % labels the x-axis
    ylabel ('Phase / °') % labels the y-axis
    legend(E_cell) % adds the legend

cd ../ % goes one folder up in the folder structure of the rawdata

saveas(plot2,'Amplitude sample.fig') % saves the Amplitude plot as MatLAB
figure
saveas(plot2,'Amplitude sample.jpg') % saves the Amplitude plot as .jpg
file
saveas(plot2,'Amplitude sample.pdf') % saves the Amplitude plot as .pdf
file
saveas(plot3,'Phase sample.fig') % saves the Phase plot as MatLAB figure
saveas(plot3,'Phase sample.jpg') % saves the Phase plot as .jpg file
saveas(plot3,'Phase sample.pdf') % saves the Phase plot as .pdf file
saveas(plot1,'DC sample.fig') % saves the DC plot as MatLAB figure
saveas(plot1,'DC sample.jpg') % saves the DC plot as .jpg file
saveas(plot1,'DC sample.pdf') % saves the DC plot as .pdf file
dlmwrite('finaldata sample.txt',finaldata); % saves the central storage
matrix as .txt file
dlmwrite('WL.txt',WL); % saves the wavelenths vector as .txt file
dlmwrite('E.txt',E); % saves the potentials vector as .txt file

num_R = numel(Vpp); % determines the number of amplitude values

per_E = zeros (num_E.num_WL); % creates a placeholder matrix in which the
amplitude values will be sorted by potential and wavelenths to create
voltabsorptogram plots
b=1;

for a=num_WL:num_WL:num_R % runs stepwise from 1 to 'number of amplitude
values' in steps of the number of wavelenths

    per_E(b,:) = Vpp(1+(a-num_WL):a); % fills the matrix with values

    b = b + 1;

end

% calculates the potential in Volt. corrected for the ferrocene half-wave
potential:

E = -1*(E/1000)+Fc;
E = E';
```

14.2 Supporting Information for Chapter: "Investigating the Influence of Linker Molecules on the Electronic Structure of PbS and CdSe QDs"

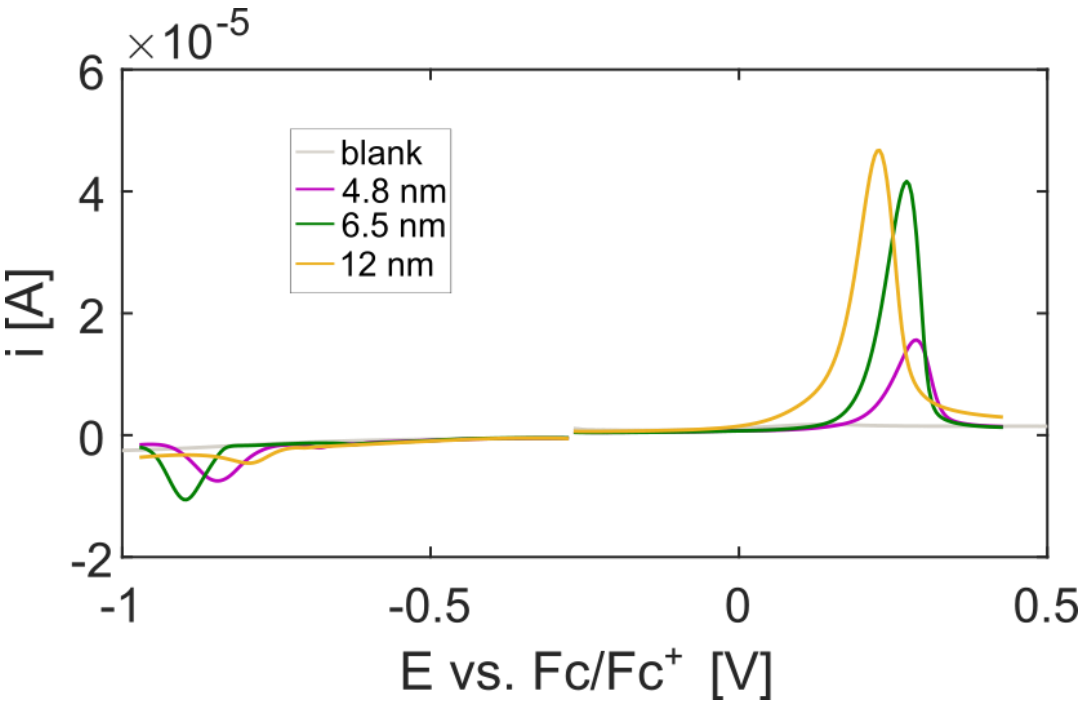

Figure 48: DPV scans of PbS QDs, measured in MeCN/$LiClO_4$.

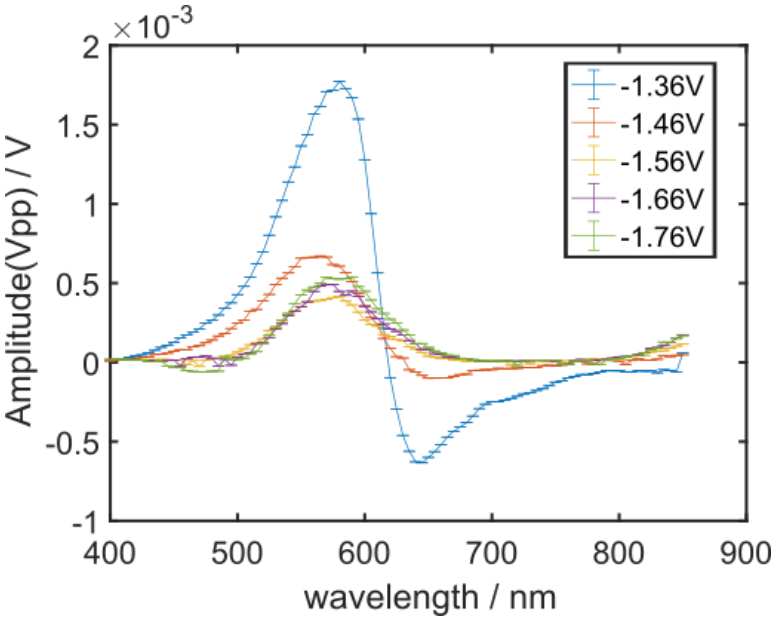

Figure 49: EMAS measurement of pure ZnPc linkers on FTO with MeCN/$LiClO_4$ as electrolyte.
A subsequent calibration of the monochromator showed that the real wavelength value is 3 nm higher than shown in this figure.

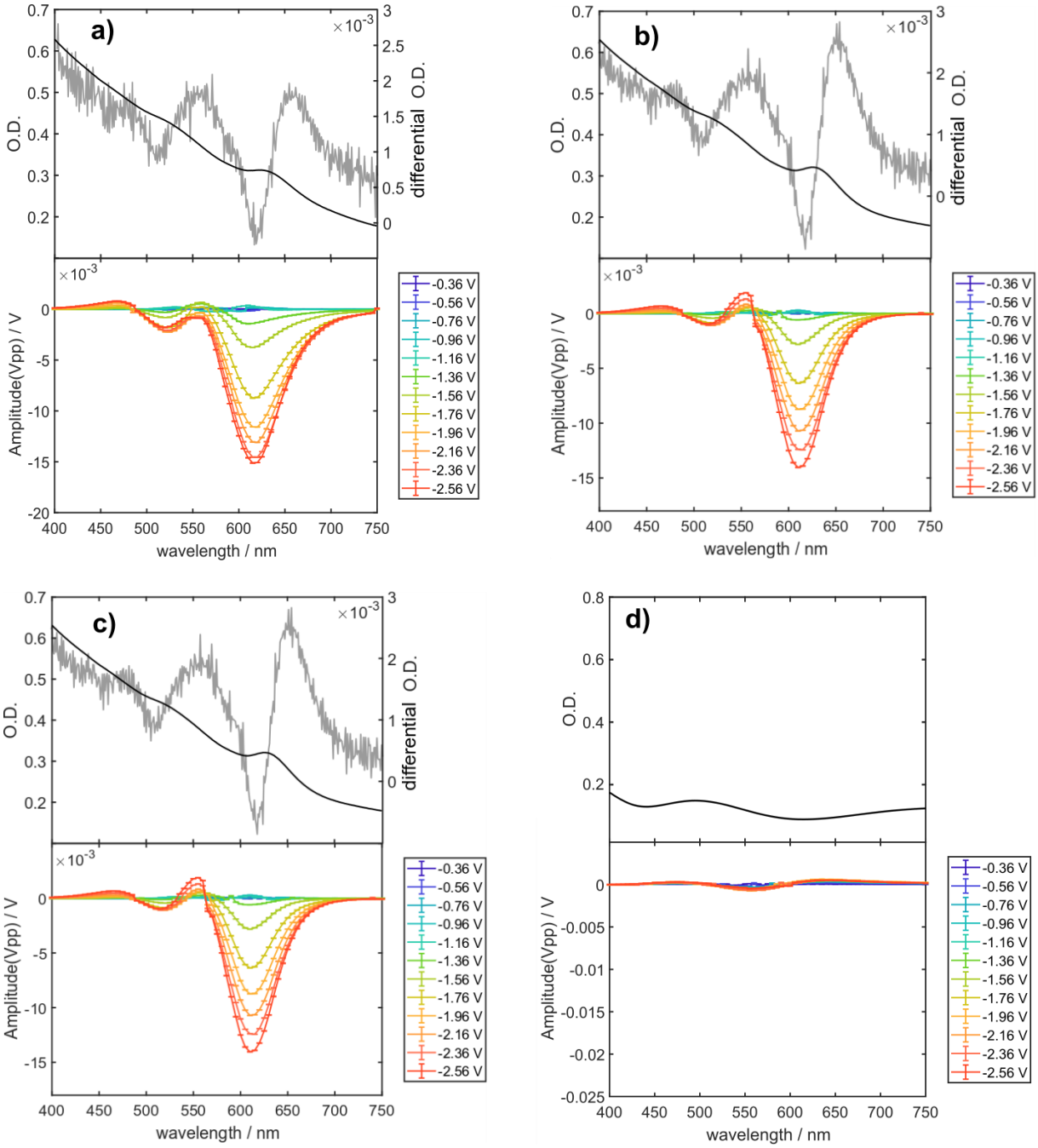

Figure 50: UV-Vis and EMAS spectra of CdSe films with various MePc linkers.
a) CdSe QDs interlinked with NiPc, b) CdSe QDs interlinked with FePc, c) CdSe QDs interlinked with CuPc and d) UV-Vis and EMAS spectrum of the clean FTO electrode. A subsequent calibration of the monochromator showed that the real wavelength value is 3 nm higher than shown in this figure.

14 Appendix

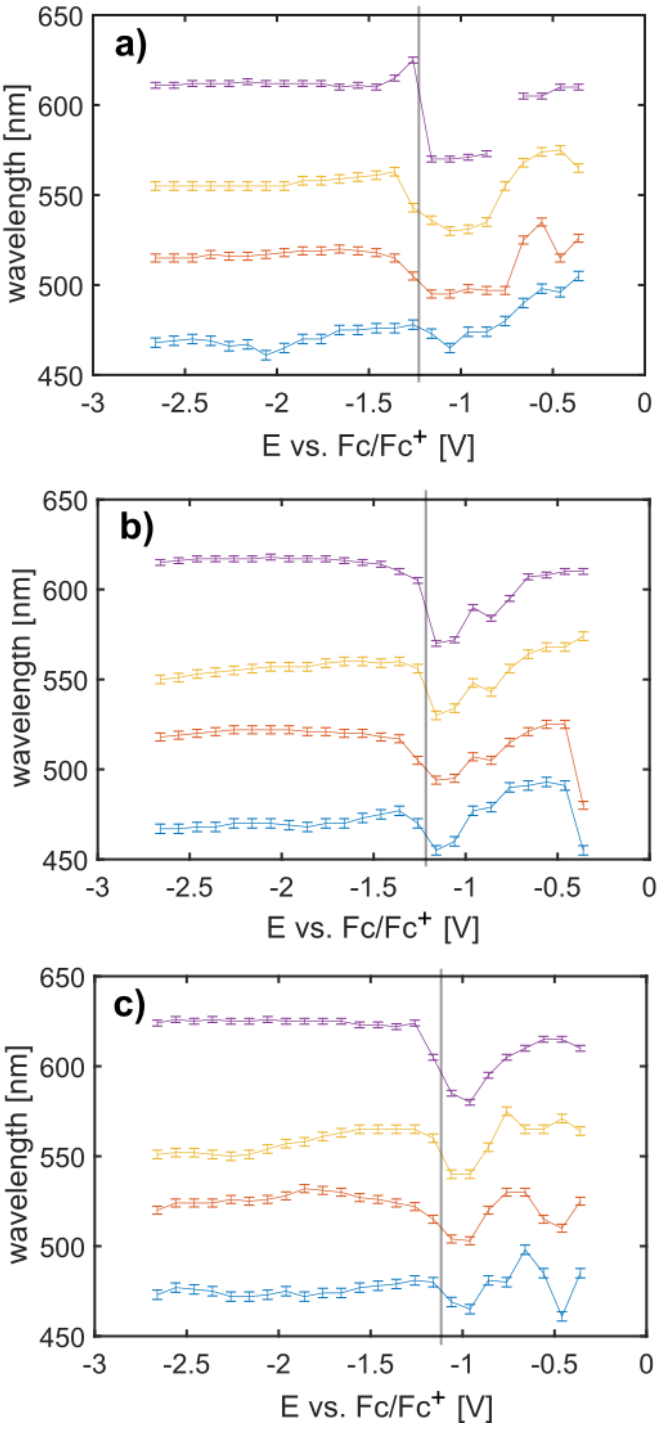

Figure 51: Maxima of the EMAS peaks as a function of the applied potential.
Peak 1 is depicted in blue, peak 2 in orange, peak 3 in yellow and peak 4 in purple. a) CdSe QDs interlinked with FePc. b) CdSe QDs interlinked with NiPc. c) CdSe QDs interlinked with CuPc. A subsequent calibration of the monochromator showed that the real wavelength value is 3 nm higher than shown in this figure.

Table 11: Fermi-Dirac plots for all peaks measured in the EMAS experiments.

Sample	Peak	Graph	Fit parameters	
CdSe + BA (measurement 1)	2	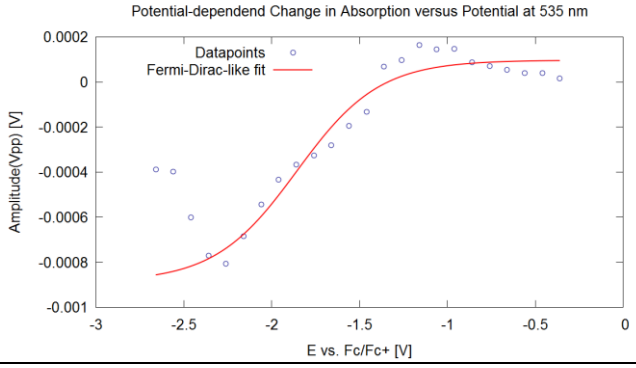	$V_{PP,end}$: $-4.46 \cdot 10^{-3}$ V	U_0: -1.87 V vs. Fc/Fc⁺
			$V_{PP,start}$: $2.61 \cdot 10^{-4}$ V	ξ: 253 mV
			Fit quality: medium (error 1+3)	
CdSe + BA (measurement 1)	4	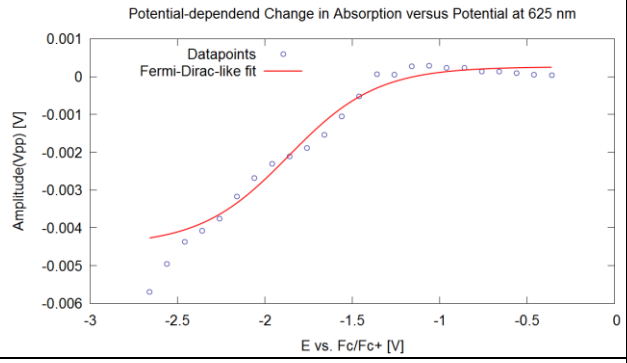	$V_{PP,end}$: $-8.8 \cdot 10^{-4}$ V	U_0: -1.87 V vs. Fc/Fc⁺
			$V_{PP,start}$: $4.99 \cdot 10^{-3}$ V	ξ: 253 mV
			Fit quality: poor (error 2)	
CdSe + BA (measurement 2)	2	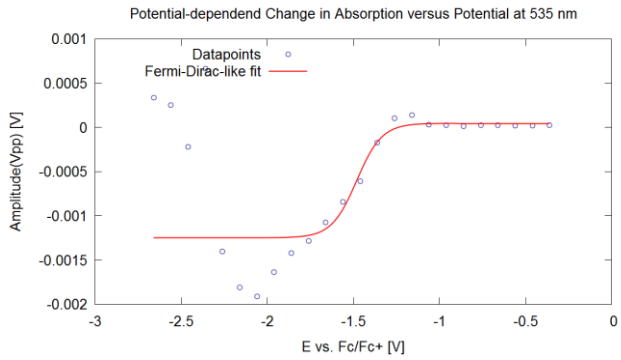	$V_{PP,end}$: $-1.24 \cdot 10^{-3}$ V	U_0: -1.48 V vs. Fc/Fc⁺
			$V_{PP,start}$: $4.60 \cdot 10^{-5}$ V	ξ: 73 mV
			Fit quality: medium (error 1)	

14 Appendix

Sample	Peak	Graph	Fit parameters	
CdSe + ZnPc (measurement 1)	1	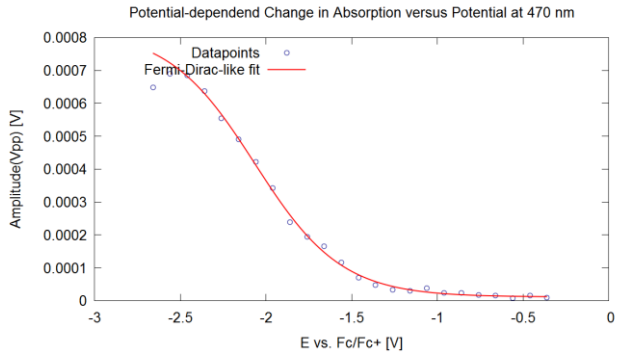	$V_{PP,end}$: $8.23 \cdot 10^{-4}$ V	U_0: -2.07 V vs. Fc/Fc$^+$
			$V_{PP,start}$: $1.13 \cdot 10^{-5}$ V	ξ: 252 mV
			Fit quality: good	
CdSe + ZnPc (measurement 1)	2	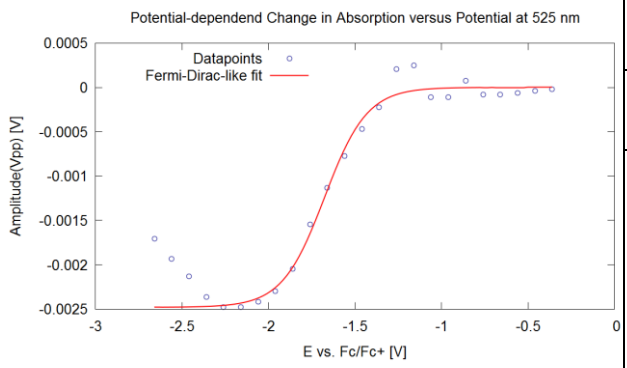	$V_{PP,end}$: $-2.48 \cdot 10^{-3}$ V	U_0: -1.68 V vs. Fc/Fc$^+$
			$V_{PP,start}$: $6.25 \cdot 10^{-7}$ V	ξ: 123 mV
			Fit quality: medium (error 1+3)	
CdSe + ZnPc (measurement 1)	4	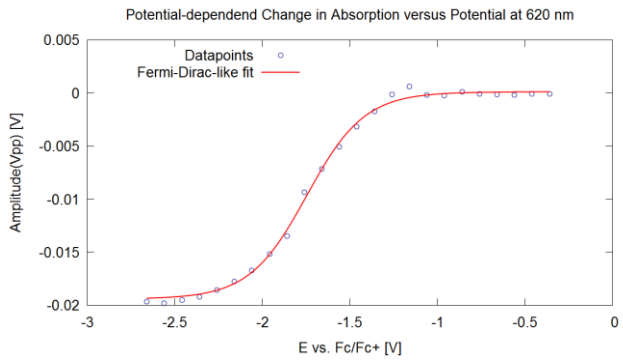	$V_{PP,end}$: $-1.94 \cdot 10^{-2}$ V	U_0: -1.75 V vs. Fc/Fc$^+$
			$V_{PP,start}$: $1.06 \cdot 10^{-4}$ V	ξ: 164 mV
			Fit quality: good	
CdSe + ZnPc (measurement 2)	2	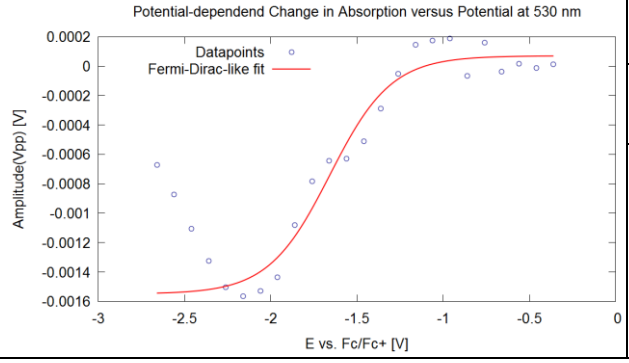	$V_{PP,end}$: $-1.55 \cdot 10^{-3}$ V	U_0: -1.66 V vs. Fc/Fc$^+$
			$V_{PP,start}$: $7.05 \cdot 10^{-5}$ V	ξ: 177 mV
			Fit quality: medium (error 1+3)	

Sample	Peak	Graph	Fit parameters	
CdSe + ZnPc (measurement 2)	4	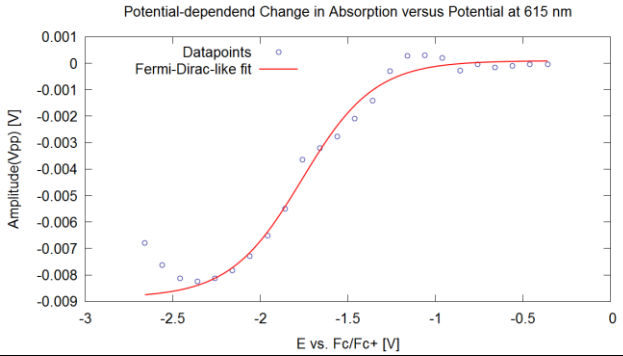	$V_{PP,end}$: $-8.86 \cdot 10^{-3}$ V	U_0: -1.76 V vs. Fc/Fc$^+$
			$V_{PP,start}$: $9.68 \cdot 10^{-5}$ V	ξ: 206 mV
			Fit quality: medium (error 1+3)	
CdSe + NiPc (measurement 1)	1	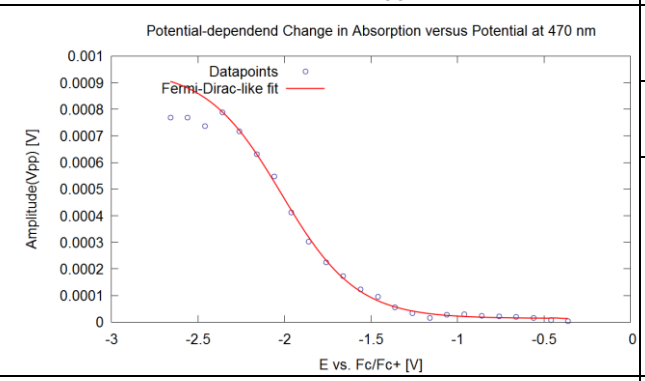	$V_{PP,end}$: $9.51 \cdot 10^{-4}$ V	U_0: -2.02 V vs. Fc/Fc$^+$
			$V_{PP,start}$: $1.40 \cdot 10^{-5}$ V	ξ: 217 mV
			Fit quality: good	
CdSe + NiPc (measurement 1)	2	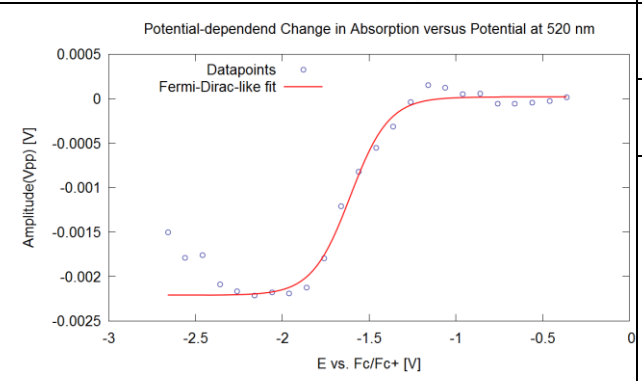	$V_{PP,end}$: $-2.21 \cdot 10^{-3}$ V	U_0: -1.61 V vs. Fc/Fc$^+$
			$V_{PP,start}$: $1.89 \cdot 10^{-5}$ V	ξ: 110 mV
			Fit quality: good	
CdSe + NiPc (measurement 1)	4	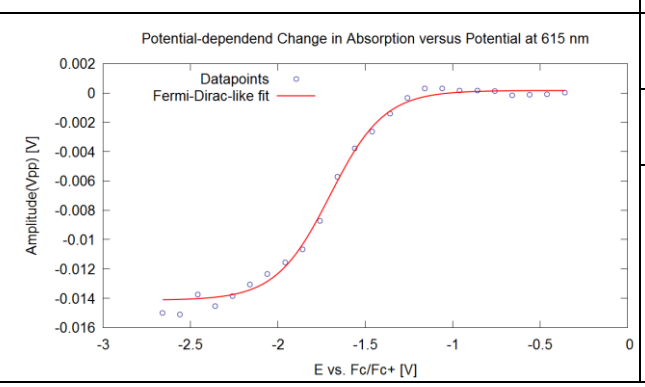	$V_{PP,end}$: $-1.41 \cdot 10^{-2}$ V	U_0: -1.70 V vs. Fc/Fc$^+$
			$V_{PP,start}$: $1.70 \cdot 10^{-4}$ V	ξ: 155 mV
			Fit quality: good	

14 Appendix

Sample	Peak	Graph	Fit parameters	
CdSe + NiPc (measurement 2)	2	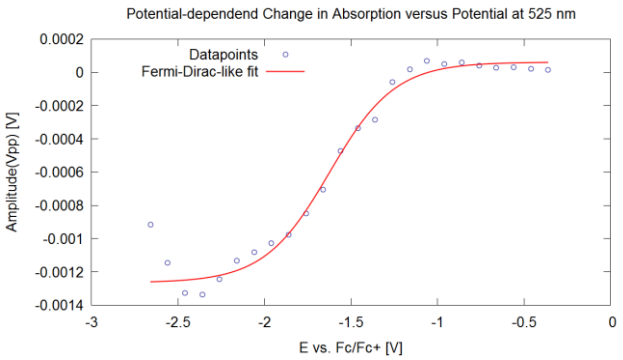	$V_{PP,end}$: $-1.27 \cdot 10^{-3}$ V	U_0: -1.62 V vs. Fc/Fc$^+$
			$V_{PP,start}$: $6.13 \cdot 10^{-5}$ V	ξ: 189 mV
			Fit quality: medium (error 1)	
CdSe + NiPc (measurement 2)	4	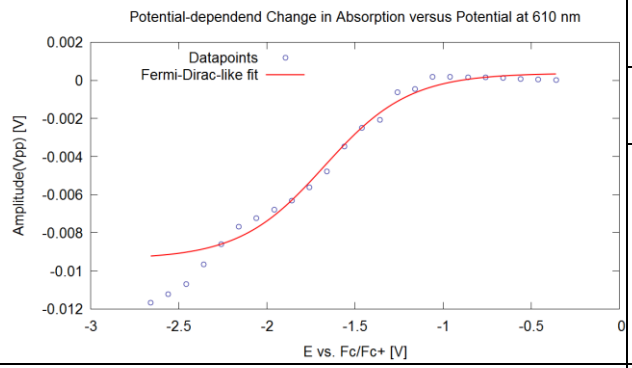	$V_{PP,end}$: $-9.38 \cdot 10^{-3}$ V	U_0: -1.67 V vs. Fc/Fc$^+$
			$V_{PP,start}$: $3.76 \cdot 10^{-4}$ V	ξ: 241 mV
			Fit quality: poor (error 2)	
CdSe + CoPc (measurement 1)	1	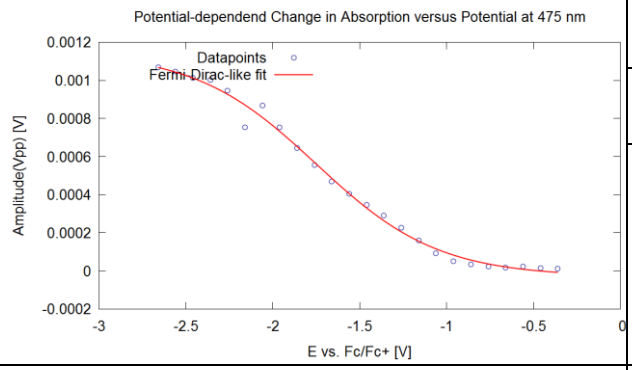	$V_{PP,end}$: $1.15 \cdot 10^{-3}$ V	U_0: -1.75 V vs. Fc/Fc$^+$
			$V_{PP,start}$: $-3.02 \cdot 10^{-5}$ V	ξ: 351 mV
			Fit quality: good	
CdSe + CoPc (measurement 1)	4	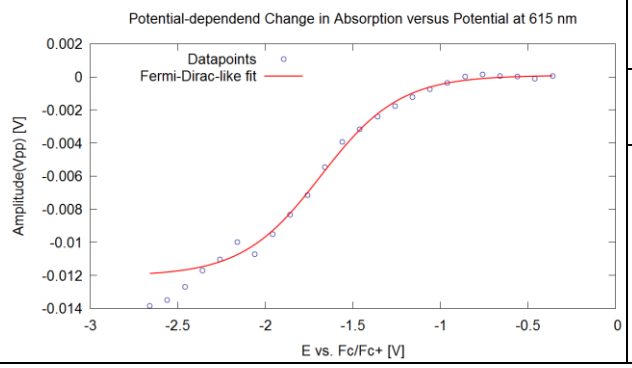	$V_{PP,end}$: $-1.01 \cdot 10^{-2}$ V	U_0: -1.68 V vs. Fc/Fc$^+$
			$V_{PP,start}$: $9.71 \cdot 10^{-5}$ V	ξ: 225 mV
			Fit quality: poor (error 2)	

Sample	Peak	Graph	Fit parameters	
CdSe + CoPc (measurement 2)	4	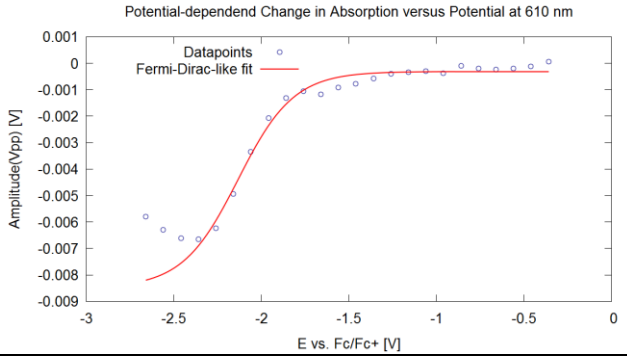	$V_{PP,end}$: $-8.48 \cdot 10^{-3}$ V	U_0: -2.13 V vs. Fc/Fc$^+$
			$V_{PP,start}$: $-3.12 \cdot 10^{-4}$ V	ξ: 158 mV
			Fit quality: medium (error 1)	
CdSe + FePc (measurement 1)	2	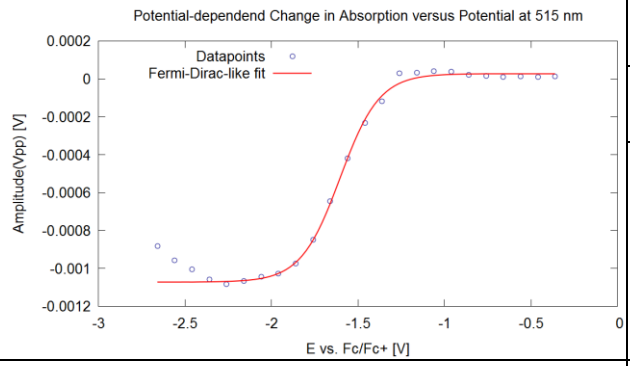	$V_{PP,end}$: $-1.07 \cdot 10^{-3}$ V	U_0: -1.60 V vs. Fc/Fc$^+$
			$V_{PP,start}$: $2.72 \cdot 10^{-5}$ V	ξ: 113 mV
			Fit quality: good	
CdSe + FePc (measurement 1)	4	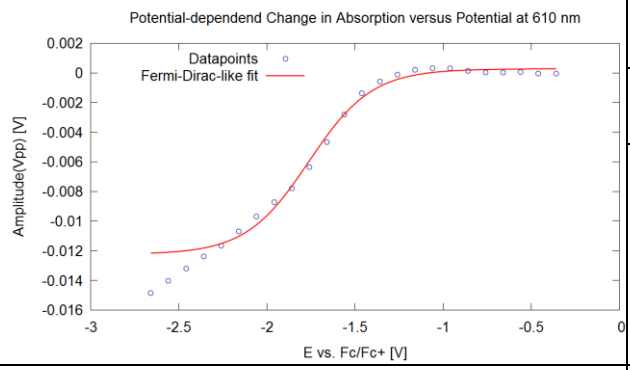	$V_{PP,end}$: $-1.22 \cdot 10^{-2}$ V	U_0: -1.76 V vs. Fc/Fc$^+$
			$V_{PP,start}$: $2.67 \cdot 10^{-4}$ V	ξ: 179 mV
			Fit quality: poor (error 2)	
CdSe + FePc (measurement 2)	4	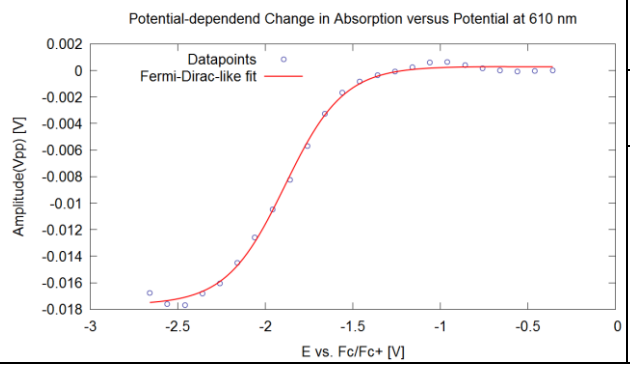	$V_{PP,end}$: $-1.77 \cdot 10^{-2}$ V	U_0: -1.89 V vs. Fc/Fc$^+$
			$V_{PP,start}$: $3.03 \cdot 10^{-4}$ V	ξ: 167 mV
			Fit quality: good	

14 Appendix

Sample	Peak	Graph	Fit parameters	
CdSe + CuPc (measurement 1)	1	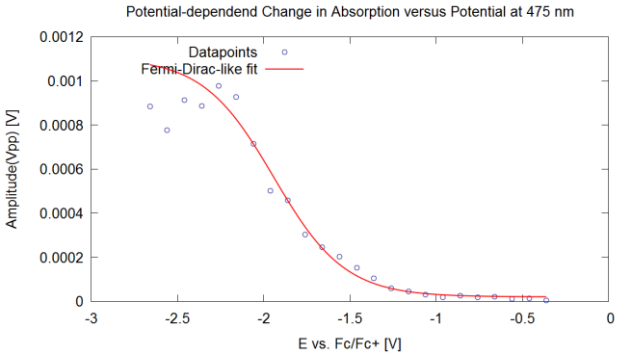	$V_{PP,end}$: $1.11 \cdot 10^{-3}$ V	U_0: -1.94 V vs. Fc/Fc$^+$
			$V_{PP,start}$: $2.05 \cdot 10^{-5}$ V	ξ: 206 mV
			Fit quality: medium (error 3)	
CdSe + CuPc (measurement 1)	4	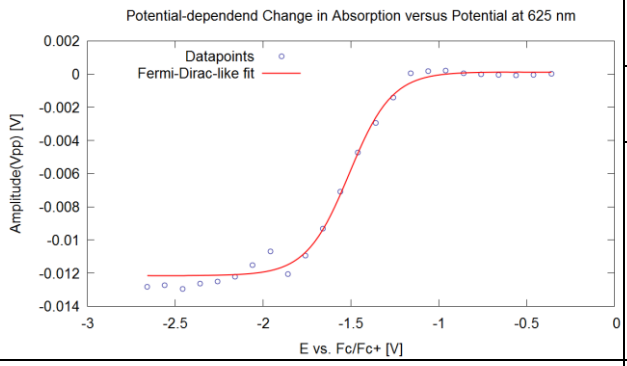	$V_{PP,end}$: $-1.01 \cdot 10^{-2}$ V	U_0: -1.51 V vs. Fc/Fc$^+$
			$V_{PP,start}$: $1.30 \cdot 10^{-4}$ V	ξ: 122 mV
			Fit quality: good	
CdSe + CuPc (measurement 2)	2	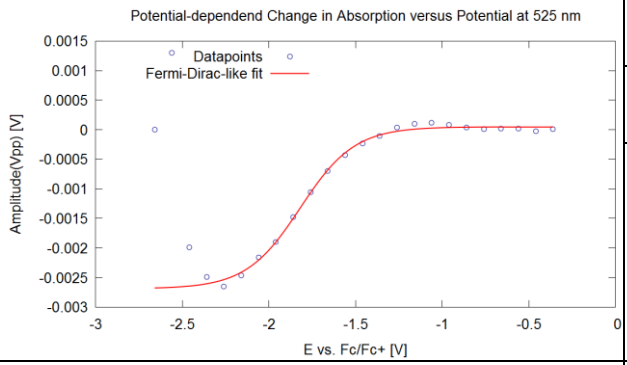	$V_{PP,end}$: $-2.70 \cdot 10^{-3}$ V	U_0: -1.82 V vs. Fc/Fc$^+$
			$V_{PP,start}$: $4.94 \cdot 10^{-5}$ V	ξ: 156 mV
			Fit quality: medium (error 1)	
CdSe + CuPc (measurement 2)	4	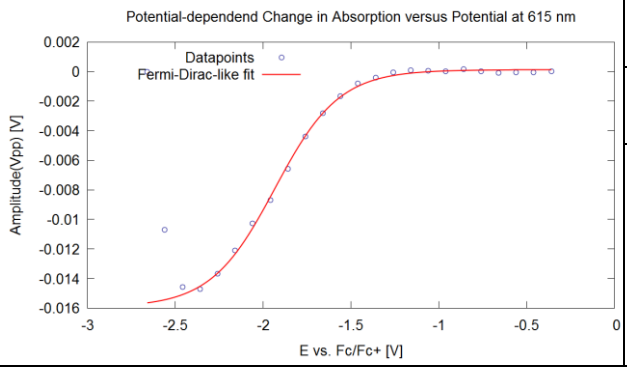	$V_{PP,end}$: $-1.59 \cdot 10^{-2}$ V	U_0: -1.93 V vs. Fc/Fc$^+$
			$V_{PP,start}$: $1.26 \cdot 10^{-4}$ V	ξ: 182 mV
			Fit quality: medium (error 1)	

Sample	Peak	Graph	Fit parameters	
CdSe + H2Pc (measurement 1)	1	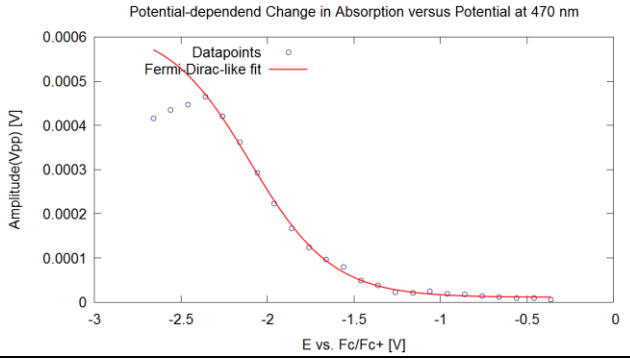	$V_{PP,end}$: $6.24 \cdot 10^{-4}$ V	U_0: -2.10 V vs. Fc/Fc$^+$
			$V_{PP,start}$: $1.11 \cdot 10^{-5}$ V	ξ: 237 mV
			Fit quality: medium (error 1)	
CdSe + H2Pc (measurement 1)	2	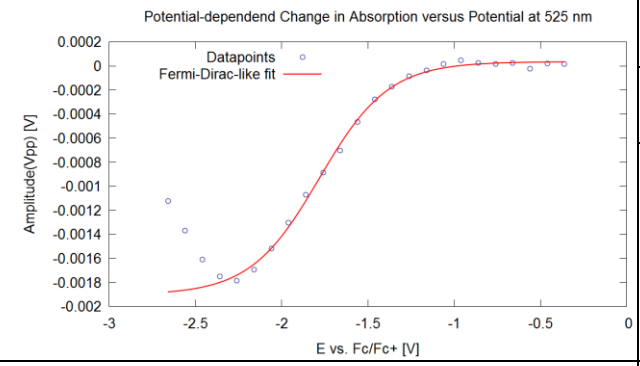	$V_{PP,end}$: $-1.90 \cdot 10^{-3}$ V	U_0: -1.78 V vs. Fc/Fc$^+$
			$V_{PP,start}$: $3.46 \cdot 10^{-5}$ V	ξ: 200 mV
			Fit quality: medium (error 1)	
CdSe + H2Pc (measurement 1)	4	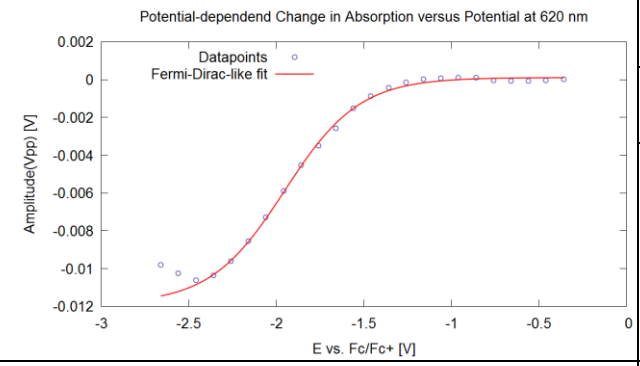	$V_{PP,end}$: $-1.19 \cdot 10^{-2}$ V	U_0: -1.95 V vs. Fc/Fc$^+$
			$V_{PP,start}$: $1.10 \cdot 10^{-4}$ V	ξ: 213 mV
			Fit quality: good	
CdSe + H2Pc (measurement 2)	2	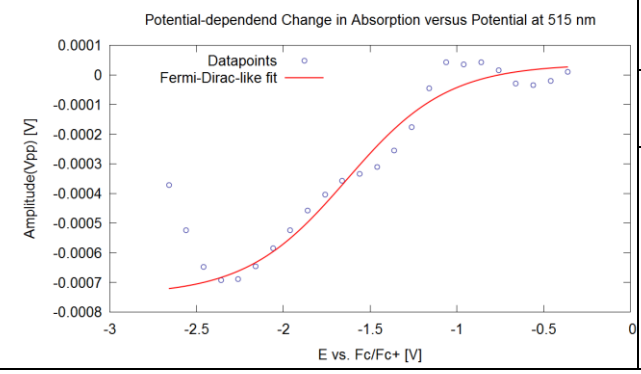	$V_{PP,end}$: $-7.44 \cdot 10^{-4}$ V	U_0: -1.63 V vs. Fc/Fc$^+$
			$V_{PP,start}$: $3.64 \cdot 10^{-5}$ V	ξ: 291 mV
			Fit quality: medium (error 1+3)	

14 Appendix

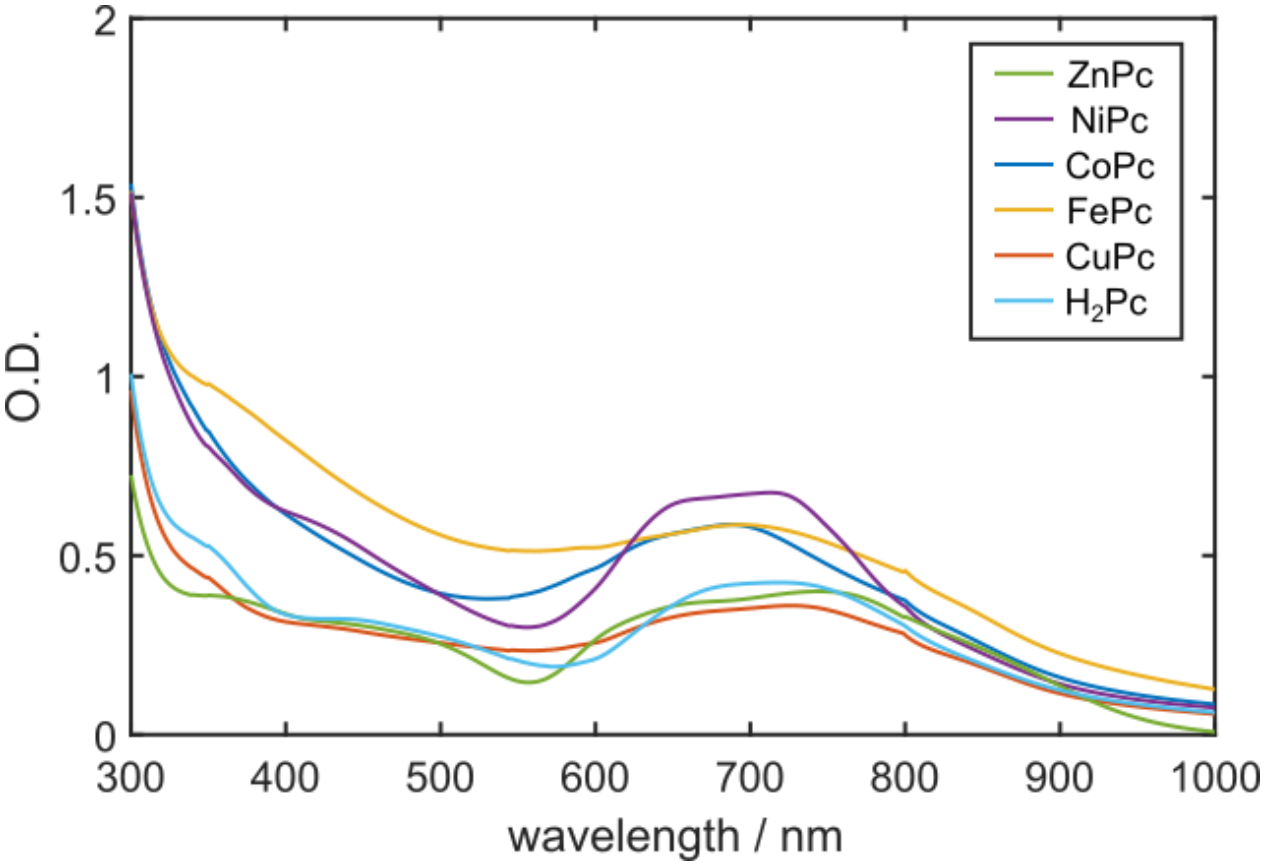

Figure 52: UV-Vis absorption spectra of the phthalocyanine linkers used in this study. All spectra are taken of the dry ligands on glass sheets.

15List of Tables

16List of Figures

17References

1. Reed, M.A., et al. *Spatial Quantization in GaAs-AlGaAs Multiple Quantum Dots.* J. Vac. Sci. Technol., B, 1986. **4**(1): p. 358-360.
2. Brus, L. *Electronic Wave-Functions in Semiconductor Clusters - Experiment and Theory.* J. Phys. Chem., 1986. **90**(12): p. 2555-2560.
3. Efros, A.L.; Efros, A.L. *Interband Absorption of Light in a Semiconductor Sphere.* Sov. Phys. Semicond., 1982. **16**(7): p. 772-775.
4. Kwon, S.G.; Hyeon, T. *Formation Mechanisms of Uniform Nanocrystals via Hot-Injection and Heat-Up Methods.* Small, 2011. **7**(19): p. 2685-2702.
5. Murray, C.B., et al. *Synthesis and Characterization of Nearly Monodisperse Cde (E = S, Se, Te) Semiconductor Nanocrystallites.* J. Am. Chem. Soc., 1993. **115**(19): p. 8706-8715.
6. Weidman, M.C., et al. *Monodisperse, Air-Stable PbS Nanocrystals via Precursor Stoichiometry Control.* ACS Nano, 2014. **8**(6): p. 6363-6371.
7. Hao, E.C., et al. *Synthesis and optical properties of CdSe and CdSe/CdS nanoparticles.* Chem. Mater., 1999. **11**(11): p. 3096-3102.
8. Bawendi, M.G., et al. *The Quantum-Mechanics of Larger Semiconductor Clusters (Quantum Dots).* Annu. Rev. Phys. Chem., 1990. **41**: p. 477-496.
9. Harris, R.D., et al. *Electronic Processes within Quantum Dot-Molecule Complexes.* Chem. Rev. 2016. **116**(21): p. 12865-12919.
10. Talapin, D.V., et al. *Prospects of Colloidal Nanocrystals for Electronic and Optoelectronic Applications.* Chem. Rev., 2010. **110**(1): p. 389-458.
11. Wang, K., et al. *Inverted organic photovoltaic cells.* Chem. Soc. Rev., 2016. **45**(10): p. 2937-2975.
12. National Renewable Energy Laboratory (NREL): "Photovoltaic Research", URL: https://www.nrel.gov/pv/, [08/22/2018].
13. Green, M.A., et al. *Solar cell efficiency tables (version 50).* Prog. Photovoltaics, 2017. **25**(7): p. 668-676.
14. Kim, J.Y., et al. *25th Anniversary Article: Colloidal Quantum Dot Materials and Devices: A Quarter-Century of Advances.* Adv. Mater., 2013. **25**(36): p. 4986-5010.
15. National Renewable Energy Laboratory (NREL): "An Analysis of the Cost and Performance of Photovoltaic Systems as a Function of Module Area", URL: https://www.nrel.gov/docs/fy17osti/67006.pdf, [08/22/2018].
16. Kusuma, J.; Balakrishna, R.G. *A review on electrical characterization techniques performed to study the device performance of quantum dot sensitized solar cells.* Sol. Energy, 2018. **159**: p. 682-696.
17. Meinardi, F., et al. *Highly efficient large-area colourless luminescent solar concentrators using heavy-metal-free colloidal quantum dots.* Nat. Nanotechnol., 2015. **10**(10): p. 878-885.
18. Debije, M.G.; Verbunt, P.P.C. *Thirty Years of Luminescent Solar Concentrator Research: Solar Energy for the Built Environment.* Adv. Energy Mater., 2012. **2**(1): p. 12-35.
19. Wang, Y., et al. *Switchable Materials for Smart Windows.* Annu. Rev. Chem. Biomol. Eng., Vol 7, 2016. **7**: p. 283-304.

20. Los Alamos National Laboratory (LANL): "Capture sunlight with your window", URL: https://www.lanl.gov/discover/news-release-archive/2015/August/08.24-capture-sunlight-with-window.php [08/22/2018].

21. Tachibana, Y., et al. *Artificial photosynthesis for solar water-splitting.* Nat. Photonics, 2012. **6**(8): p. 511-518.

22. Tuysuz, H.; Chan, C.K. *Preface: Solar Energy for Fuels.* Top. Curr. Chem., 2016. **371**: p. V-Vi.

23. Pietryga, J.M., et al. *Spectroscopic and Device Aspects of Nanocrystal Quantum Dots.* Chem. Rev., 2016. **116**(18): p. 10513-10622.

24. Liu, X., et al. *Size-Controlled Synthesis of Cu2-xE (E = S, Se) Nanocrystals with Strong Tunable Near-Infrared Localized Surface Plasmon Resonance and High Conductivity in Thin Films.* Adv. Funct. Mater., 2013. **23**(10): p. 1256-1264.

25. Ji, S.L., et al. *A Route to Phase Controllable Cu2ZnSn(S1-xSex)(4) Nanocrystals with Tunable Energy Bands.* Sci. Rep., 2013. **3**.

26. Bekenstein, Y., et al. *Charge Transport in Cu2S Nanocrystals Arrays: Effects of Crystallite Size and Ligand Length.* Z. Phys. Chem, 2015. **229**(1-2): p. 179-190.

27. Bekenstein, Y., et al. *Thermal Doping by Vacancy Formation in Copper Sulfide Nanocrystal Arrays.* Nano Lett., 2014. **14**(3): p. 1349-1353.

28. Panthani, M.G., et al. *High Efficiency Solution Processed Sintered CdTe Nanocrystal Solar Cells: The Role of Interfaces.* Nano Lett., 2014. **14**(2): p. 670-675.

29. Boles, M.A., et al. *The surface science of nanocrystals.* Nat. Mater., 2016. **15**(2): p. 141-153.

30. Scheele, M., et al. *Coupled organic-inorganic nanostructures (COIN).* Phys. Chem. Chem. Phys., 2015. **17**(1): p. 97-111.

31. Kittel, C. *Introduction to Solid State Physics.* John Wiley & Sons, Inc., 1971, ISBN: 0-471-41526-X.

32. Efros, A.L.; Rosen, M. *The electronic structure of semiconductor nanocrystals.* Annu. Rev. Mater. Sci., 2000. **30**: p. 475-521.

33. Pokutnii, S.I. *Exciton binding energy in semiconductor quantum dots.* Semiconductors, 2010. **44**(4): p. 488-493.

34. Singh, V.A., et al. *Semiconductor quantum dots: Theory and phenomenology.* Bull. Mater. Sci., 1999. **22**(3): p. 563-569.

35. Yoffe, A.D. *Semiconductor quantum dots and related systems: electronic, optical, luminescence and related properties of low dimensional systems.* Adv. Phys., 2001. **50**(1): p. 1-208.

36. Brus, L.E. *A Simple-Model for the Ionization-Potential, Electron-Affinity, and Aqueous Redox Potentials of Small Semiconductor Crystallites.* J. Chem. Phys., 1983. **79**(11): p. 5566-5571.

37. Ekimov, A.I.; Onushchenko, A.A. *Quantum Size Effect in 3-Dimensional Microscopic Semiconductor Crystals.* JETP Lett., 1981. **34**(6): p. 345-349.

38. Atkins, P.; Friedman, R. *Molecular Quantum Mechanics.* Oxford University Press, 2005, ISBN: 978-0-19-954142-3.

39. Pokutnyi, S.I. *Exciton states in semiconductor spherical nanostructures.* Semiconductors, 2005. **39**(9): p. 1066-1070.

40. Grigoryan, G.B., et al. *Confined Excitons and Biexcitons in Semiconductor Microcrystals Embedded in an Insulating Glass Matrix.* Fiz. Tverd. Tela, 1990. **32**(12): p. 3512-3521.

41. Fu, H.X.; Zunger, A. *InP quantum dots: Electronic structure, surface effects, and the redshifted emission.* Phys. Rev. B, 1997. **56**(3): p. 1496-1508.

42. Troparevsky, M.C., et al. *Optical properties of CdSe quantum dots.* J. Chem. Phys., 2003. **119**(4): p. 2284-2287.

43. Prezhdo, O.V. *Photoinduced Dynamics in Semiconductor Quantum Dots: Insights from Time-Domain ab Initio Studies.* Acc. Chem. Res., 2009. **42**(12): p. 2005-2016.

44. Klimov, V.I., et al. *Electron and hole relaxation pathways in semiconductor quantum dots.* Phys. Rev. B, 1999. **60**(19): p. 13740-13749.

45. André, A. *Struktur und Ladungstransport gekoppelter organischer-anorganischer Nanostrukturen.* Dissertation, University of Tübingen, 2017.

46. Talapin, D.V.; Murray, C.B. *PbSe nanocrystal solids for n- and p-channel thin film field-effect transistors.* Science, 2005. **310**(5745): p. 86-89.

47. Norris, D.J., et al. *Doped nanocrystals.* Science, 2008. **319**(5871): p. 1776-1779.

48. Yin, Y.; Alivisatos, A.P. *Colloidal nanocrystal synthesis and the organic-inorganic interface.* Nature, 2005. **437**(7059): p. 664-670.

49. Murray, C.B., et al. *Synthesis and characterization of monodisperse nanocrystals and close-packed nanocrystal assemblies.* Annu. Rev. Mater. Sci., 2000. **30**: p. 545-610.

50. Shevchenko, E.V., et al. *Study of nucleation and growth in the organometallic synthesis of magnetic alloy nanocrystals: The role of nucleation rate in size control of CoPt3 nanocrystals.* J. Am. Chem. Soc., 2003. **125**(30): p. 9090-9101.

51. Nag, A., et al. *Metal-free Inorganic Ligands for Colloidal Nanocrystals: S2-, HS-, Se2-, HSe-, Te2-, HTe-, TeS32-, OH-, and NH2- as Surface Ligands.* J. Am. Chem. Soc., 2011. **133**(27): p. 10612-10620.

52. Kovalenko, M.V., et al. *Colloidal Nanocrystals with Molecular Metal Chalcogenide Surface Ligands.* Science, 2009. **324**(5933): p. 1417-1420.

53. Pellegrino, T., et al. *Hydrophobic nanocrystals coated with an amphiphilic polymer shell: A general route to water soluble nanocrystals.* Nano Lett., 2004. **4**(4): p. 703-707.

54. Sluydts, M., et al. *Ligand Addition Energies and the Stoichiometry of Colloidal Nanocrystals.* ACS Nano, 2016. **10**(1): p. 1462-1474.

55. Anderson, N.C., et al. *Ligand Exchange and the Stoichiometry of Metal Chalcogenide Nanocrystals: Spectroscopic Observation of Facile Metal-Carboxylate Displacement and Binding.* J. Am. Chem. Soc., 2013. **135**(49): p. 18536-18548.

56. Aldeek, F., et al. *UV and Sunlight Driven Photoligation of Quantum Dots: Understanding the Photochemical Transformation of the Ligands.* J. Am. Chem. Soc., 2015. **137**(7): p. 2704-2714.

57. Wheeler, L.M., et al. *All-Inorganic Germanium Nanocrystal Films by Cationic Ligand Exchange.* Nano Lett., 2016. **16**(3): p. 1949-1954.

58. Soreni-Harari, M., et al. *Tuning energetic levels in nanocrystal quantum dots through surface manipulations.* Nano Lett., 2008. **8**(2): p. 678-684.

59. Timp, B.A.; Zhu, X.Y. *Electronic energy alignment at the PbSe quantum dots/ZnO(10(1)over-bar0) interface.* Surf. Sci., 2010. **604**(17-18): p. 1335-1341.

60. Jasieniak, J., et al. *Size-Dependent Valence and Conduction Band-Edge Energies of Semiconductor Nanocrystals.* ACS Nano, 2011. **5**(7): p. 5888-5902.

17 References

61. Ning, Z.J., et al. *Air-stable n-type colloidal quantum dot solids.* Nat. Mater., 2014. **13**(8): p. 822-828.

62. Guyot-Sionnest, P., et al. *Intraband relaxation in CdSe quantum dots.* Phys. Rev. B, 1999. **60**(4): p. R2181-R2184.

63. Wuister, S.F., et al. *Influence of thiol capping on the exciton luminescence and decay kinetics of CdTe and CdSe quantum.* J. Phys. Chem. B, 2004. **108**(45): p. 17393-17397.

64. Liu, Y., et al. *Dependence of Carrier Mobility on Nanocrystal Size and Ligand Length in PbSe Nanocrystal Solids.* Nano Lett., 2010. **10**(5): p. 1960-1969.

65. Vanmaekelbergh, D. ;Liljeroth, P. *Electron-conducting quantum dot solids: novel materials based on colloidal semiconductor nanocrystals.* Chem. Soc. Rev., 2005. **34**(4): p. 299-312.

66. Lazarenkova, O.L.; Balandin, A.A. *Miniband formation in a quantum dot crystal.* J. Appl. Phys., 2001. **89**(10): p. 5509-5515.

67. Luther, J.M., et al., *Structural, optical and electrical properties of self-assembled films of PbSe nanocrystals treated with 1,2-ethanedithiol.* ACS Nano, 2008. **2**(2): p. 271-280.

68. Andre, A., et al. *Structure, transport and photoconductance of PbS quantum dot monolayers functionalized with a copper phthalocyanine derivative.* Chem. Commun., 2017. **53**(10): p. 1700-1703.

69. Chuang, C.H.M. et al. *Improved performance and stability in quantum dot solar cells through band alignment engineering.* Nat. Mater., 2014. **13**(8): p. 796-801.

70. Balazs, D.M.; Loi, M.A. *Lead-Chalcogenide Colloidal-Quantum-Dot Solids: Novel Assembly Methods, Electronic Structure Control, and Application Prospects.* Adv. Mater., 2018. **30**(33).

71. Chen, O., et al. *Pure colors from core-shell quantum dots.* MRS Bull., 2013. **38**(9): p. 696-702.

72. Luther, J.M., et al. *Localized surface plasmon resonances arising from free carriers in doped quantum dots.* Nat. Mater., 2011. **10**(5): p. 361-366.

73. Hutter, E.; Fendler, J.H. *Exploitation of localized surface plasmon resonance.* Adv. Mater., 2004. **16**(19): p. 1685-1706.

74. Jain, P.K., et al. *Noble Metals on the Nanoscale: Optical and Photothermal Properties and Some Applications in Imaging, Sensing, Biology, and Medicine.* Acc. Chem. Res., 2008. **41**(12): p. 1578-1586.

75. Cassaignon, S., et al. *Copper Diffusion in Copper Sulfide: a Systematic Study.* Ionics, 1998. **4**(5-6): p. 364-371.

76. Kriegel, I., et al. *Plasmonic doped semiconductor nanocrystals: Properties, fabrication, applications and perspectives.* Phys. Rep., 2017. **674**: p. 1-52.

77. Mulder, B.J. *Optical Properties of Crystals of Cuprous Sulfides (Chalcosite, Djurleite, Cu1.9s, and Digenite).* Phys. Status Solidi, 1972. **13**(1): p. 79ff.

78. Xie, Y., et al. *Metallic-like Stoichiometric Copper Sulfide Nanocrystals: Phase- and Shape-Selective Synthesis, Near-Infrared Surface Plasmon Resonance Properties, and Their Modeling.* ACS Nano, 2013. **7**(8): p. 7352-7369.

79. Munro, A.M., et al. *Photoemission Spectroscopy of Tethered CdSe Nanocrystals: Shifts in Ionization Potential and Local Vacuum Level As a Function of Nanocrystal Capping Ligand.* ACS Appl. Mater. Interfaces, 2010. **2**(3): p. 863-869.

80. D'Andrade, B.W., et al. *Relationship between the ionization and oxidation potentials of molecular organic semiconductors.* Org. Electron., 2005. **6**(1): p. 11-20.

81. Gerischer, H. *Neglected Problems in the Ph-Dependence of the Flat-Band Potential of Semiconducting Oxides and Semiconductors Covered with Oxide Layers.* Electrochim. Acta, 1989. **34**(8): p. 1005-1009.

82. Nozik, A.J. *Photoelectrochemistry - Applications to Solar-Energy Conversion.* Annu. Rev. Phys. Chem, 1978. **29**: p. 189-222.

83. Beranek, R. *(Photo)electrochemical Methods for the Determination of the Band Edge Positions of TiO2-Based Nanomaterials (vol 2011, pg 20, 2011).* Adv. Phys. Chem., 2016.

84. Xu, Y.; Schoonen, M.A.A. *The absolute energy positions of conduction and valence bands of selected semiconducting minerals.* Am. Mineral., 2000. **85**(3-4): p. 543-556.

85. Amelia, M., et al. *Electrochemical properties of CdSe and CdTe quantum dots.* Chem. Soc. Rev., 2012. **41**(17): p. 5728-5743.

86. Bard, A.J., et al. *Electrochemistry and electrogenerated chemiluminescence of semiconductor nanocrystals in solutions and in films.* Struct. Bond., 2005. **118**: p. 1-57.

87. Guyot-Sionnest, P., et al. *Spectroelectrochemistry of semiconductor nanocrystals.* Abstr. Pap. Am. Chem. S., 2003. **225**: p. U468-U468.

88. van der Stam, W., et al. *Switching between Plasmonic and Fluorescent Copper Sulfide Nanocrystals.* J. Am. Chem. Soc., 2017. **139**(37): p. 13208-13217.

89. Noviandri, I., et al. *The decamethylferrocenium/decamethylferrocene redox couple: A superior redox standard to the ferrocenium/ferrocene redox couple for studying solvent effects on the thermodynamics of electron transfer.* J. Phys. Chem. B, 1999. **103**(32): p. 6713-6722.

90. Bard, A.J.; Faulkner, L.R. *Electrochemical Methods, Fundamentals and Applications.* John Wiley & Sons, Inc., 2001, ISBN 0-471-04372-9.

91. Hamann, C.H.; Vielstich, W. *Electrochemistry.* Wiley VCH, 2005, ISBN 978-3-527-31069-2.

92. Pommerehne, J., et al. *Efficient 2-Layer Leds on a Polymer Blend Basis.* Adv. Mater., 1995. **7**(6): p. 551-554.

93. Cardona, C.M., et al. *Electrochemical Considerations for Determining Absolute Frontier Orbital Energy Levels of Conjugated Polymers for Solar Cell Applications.* Adv. Mater., 2011. **23**(20): p. 2367-2371.

94. He, P.X.; Faulkner; L.R. *Intelligent, Automatic Compensation of Solution Resistance.* Anal. Chem., 1986. **58**(3): p. 517-523.

95. Scholz, F., et al. *Electrochemistry of Immobilized Particles and Droplets -Experiments with Three Phase Electrodes.* Springer International Publishing, 2015, ISBN 978-3-319-10842-1.

96. Oldham, K.B. *Voltammetry at a three-phase junction.* J. Solid State Electrochem., 1998. **2**(6): p. 367-377.

97. Boehme, S.C., et al. *Electrochemical Charging of CdSe Quantum Dot Films: Dependence on Void Size and Counterion Proximity.* ACS Nano, 2013. **7**(3): p. 2500-2508.

98. Roest, A.L., et al. *Long-range transport in an assembly of ZnO quantum dots: The effects of quantum confinement, coulomb repulsion and structural disorder.* Chem. Phys. Chem, 2003. **4**(9): p. 959-966.

99. Roest, A.L., et al. *Staircase in the electron mobility of a ZnO quantum dot assembly due to shell filling.* Phys. Rev. Lett., 2002. **89**(3).

100. Horowitz, P.; Hill, W. *The Art of Electronics.* Cambridge University Press, 1989, ISBN 978-0-521-8096-9.

17 References

101. Roest, A.L., et al. *Electron-conducting quantum-dot solids with ionic charge compensation.* Faraday Discuss., 2004. **125**: p. 55-62.

102. Houtepen, A. *Charge injection and transport in quantum confined and disordered systems.* Dissertation, University of Utrecht, 2007.

103. Meulenkamp, E.A. *Electron transport in nanoparticulate ZnO films.* J. Phys. Chem. B, 1999. **103**(37): p. 7831-7838.

104. Hickey, S.G., et al, *Photoelectrochemical studies of CdS nanoparticle modified electrodes: Absorption and photocurrent investigations.* J. Phys. Chem. B, 2000. **104**(32): p. 7623-7626.

105. Doherty, R.P., et al. *A study of CdS nanoparticle surface states by potential-modulated sub-bandgap spectroscopy.* J. Electroanal. Chem., 2004. **569**(2): p. 271-274.

106. Riley, D.J.; Tull, E.J. *Potential modulated absorbance spectroscopy: an investigation of the potential distribution at a CdS nanoparticle modified electrode.* J. Electroanal. Chem., 2001. **504**(1): p. 45-51.

107. Wehrenberg, B.L.; Guyot-Sionnest, P. *Electron and hole injection in PbSe quantum dot films.* J. Am. Chem. Soc., 2003. **125**(26): p. 7806-7807.

108. Poppe, J., et al. *Photoelectrochemical Investigations of Semiconductor Nanoparticles and Their Application to Solar Cells.* J. Phys. Chem. C, 2014. **118**(30): p. 17123-17141.

109. Spittel, D., et al. *Absolute Energy Level Positions in CdSe Nanostructures from Potential-Modulated Absorption Spectroscopy (EMAS).* ACS Nano, 2017. **11**(12): p. 12174-12184.

110. Boehme, S.C., et al. *In Situ Spectroelectrochemical Determination of Energy Levels and Energy Level Offsets in Quantum -Dot Heterojunctions.* J. Phys. Chem. C, 2016. **120**(9): p. 5164-5173.

111. Stanford Research: "About Lock-in Amplifiers", URL: https://www.thinksrs.com/downloads/pdfs/applicationnotes/AboutLIAs.pdf [08/20/2018].

112. Choi, J.H., et al. *Bandlike Transport in Strongly Coupled and Doped Quantum Dot Solids: A Route to High-Performance Thin-Film Electronics.* Nano Lett., 2012. **12**(5): p. 2631-2638.

113. Tour, J.M., et al. *Self-Assembled Monolayers and Multilayers of Conjugated Thiols, Alpha,Omega-Dithiols, and Thioacetyl-Containing Adsorbates - Understanding Attachments between Potential Molecular Wires and Gold Surfaces.* J. Am. Chem. Soc., 1995. **117**(37): p. 9529-9534.

114. Andre, A., et al. *Electron-Conducting PbS Nanocrystal Superlattices with Long-Range Order Enabled by Terthiophene Molecular Linkers.* ACS Appl. Mater. Interfaces, 2018. **10**(29): p. 24708-24714.

115. Jung, S.H., et al. *Syntheses and characterization of soluble phthalocyanine derivatives for organic electroluminescent devices.* Mat. Sci. Eng. B-Solid., 2001. **85**(2-3): p. 160-164.

116. Alzeer, J., et al. *An efficient two-step synthesis of metal-free phthalocyanines using a Zn(II) template.* Chem. Commun., 2009(15): p. 1970-1971.

117. Xie, Y., et al. *Copper Sulfide Nanocrystals with Tunable Composition by Reduction of Covellite Nanocrystals with Cu+ Ions.* J. Am. Chem. Soc., 2013. **135**(46): p. 17630-17637.

118. Wolf, A., et al. *Tuning the LSPR in copper chalcogenide nanoparticles by cation intercalation, cation exchange and metal growth.* Nanoscale, 2015. **7**(46): p. 19519-19527.

119. Dorfs, D., et al. *Reversible Tunability of the Near-Infrared Valence Band Plasmon Resonance in Cu2-xSe Nanocrystals.* J. Am. Chem. Soc., 2011. **133**(29): p. 11175-11180.

120. Wolf, A., et al. *Growth of Cu2-xSe-CuPt and Cu1.1S-Pt Hybrid Nanoparticles.* J. Phys. Chem. C, 2016. **120**(38): p. 21925-21931.

121. Moreels, I., et al. *Size-Dependent Optical Properties of Colloidal PbS Quantum Dots.* ACS Nano, 2009. **3**(10): p. 3023-3030.

122. Ibanez, M., et al. *Electron Doping in Bottom-Up Engineered Thermoelectric Nanomaterials through HCI-Mediated Ligand Displacement.* J. Am. Chem. Soc., 2015. **137**(12): p. 4046-4049.

123. Ibanez, M., et al. *High-performance thermoelectric nanocomposites from nanocrystal building blocks.* Nat. Commun., 2016. **7**.

124. Panda, S.K., et al. *Gradated alloyed CdZnSe nanocrystals with high luminescence quantum yields and stability for optoelectronic and biological applications.* J. Mat. Chem., 2011. **21**(31): p. 11550-11555.

125. Yu, W.W., et al. *Experimental determination of the extinction coefficient of CdTe, CdSe, and CdS nanocrystals.* Chem. Mater., 2003. **15**(14): p. 2854-2860.

126. Chen, O., et al. *Compact high-quality CdSe-CdS core-shell nanocrystals with narrow emission linewidths and suppressed blinking.* Nat. Mater., 2013. **12**(5): p. 445-451.

127. Chen, O., et al. *Synthesis of Metal-Selenide Nanocrystals Using Selenium Dioxide as the Selenium Precursor.* Angew. Chem. Int. Ed., 2008. **47**(45): p. 8638-8641.

128. Knauf, R.R., et al. *Quantifying Ligand Exchange Reactions at CdSe Nanocrystal Surfaces.* Chem. Mater., 2016. **28**(13): p. 4762-4770.

129. Pan, D.C., et al. *Observation of nucleation and growth of CdS nanocrystals in a two-phase system.* Chem. Mater., 2008. **20**(11): p. 3560-3566.

130. Zhao, Y.X., et al. *Plasmonic Cu2-xS Nanocrystals: Optical and Structural Properties of Copper-Deficient Copper(I) Sulfides.* J. Am. Chem. Soc., 2009. **131**(12): p. 4253-4261.

131. Willhammar, T., et al. *Structure and vacancy distribution in copper telluride nanoparticles influence plasmonic activity in the near-infrared.* Nat. Commun., 2017. **8**.

132. Roy, P.; Srivastava, S.K. *Nanostructured copper sulfides: synthesis, properties and applications.* Cryst. Eng. Comm., 2015. **17**(41): p. 7801-7815.

133. van der Stam, W., et al, *Prospects of Colloidal Copper Chalcogenide Nanocrystals.* Chem. Phys. Chem., 2016. **17**(5): p. 559-581.

134. Zhao, Y.X.; Burda, C. *Development of plasmonic semiconductor nanomaterials with copper chalcogenides for a future with sustainable energy materials.* Energy Environ. Sci., 2012. **5**(2): p. 5564-5576.

135. Comin, A.; Manna, L. *New materials for tunable plasmonic colloidal nanocrystals.* Chem. Soc. Rev., 2014. **43**(11): p. 3957-3975.

136. Mattox, T.M., et al. *Chemical Control of Plasmons in Metal Chalcogenide and Metal Oxide Nanostructures.* Adv. Mater., 2015. **27**(38): p. 5830-5837.

137. Liu, X.; Swihart, M.T. *Heavily-doped colloidal semiconductor and metal oxide nanocrystals: an emerging new class of plasmonic nanomaterials.* Chem. Soc. Rev., 2014. **43**(11): p. 3908-3920.

138. Faucheaux, J.A., et al. *Plasmon Resonances of Semiconductor Nanocrystals: Physical Principles and New Opportunities.* J. Phys. Chem. Lett., 2014. **5**(6): p. 976-985.

139. Kriegel, I., et al. *Tuning the Excitonic and Plasmonic Properties of Copper Chalcogenide Nanocrystals.* J. Am. Chem. Soc., 2012. **134**(3): p. 1583-1590.

140. Liao, M.S.; Scheiner, S. *Electronic structure and bonding in metal phthalocyanines, Metal=Fe, Co, Ni, Cu, Zn, Mg.* J. Chem. Phys., 2001. **114**(22): p. 9780-9791.

17 References

141. Llorente, V.B., et al. *Electrochemical Tuning of Localized Surface Plasmon Resonance in Copper Chalcogenide Nanocrystals.* J. Phys. Chem. C, 2017. **121**(33): p. 18244-18253.

142. Martinez, M.A., et al. *Electrochemical Stability of Indium Tin Oxide Thin-Films.* Electrochim. Acta, 1992. **37**(14): p. 2565-2571.

143. Monk, P.M.S.; Man, C.M. *Reductive ion insertion into thin-film indium tin oxide (ITO) in aqueous acidic solutions: the effect of leaching of indium from the ITO.* J. Mater. Sci. Mater. Electron., 1999. **10**(2): p. 101-107.

144. Matveeva, E. *Electrochemistry of the indium-tin oxide electrode in 1 M NaOH electrolyte.* J. Electrochem. Soc., 2005. **152**(9): p. H138-H145.

145. Vinokurov, K., et al. *Copper Sulfide Nanocrystal Level Structure and Electrochemical Functionality towards Sensing Applications.* Chem. Phys. Chem, 2016. **17**(5): p. 675-680.

146. Jain, P.K., et al. *Doped Nanocrystals as Plasmonic Probes of Redox Chemistry.* Angew. Chem. Int. Ed., 2013. **52**(51): p. 13671-13675.

147. Amelia, M., et al. *Redox properties of CdSe and CdSe-ZnS quantum dots in solution.* Pure Appl. Chem., 2011. **83**(1): p. 1-8.

148. Ma, X.D., et al. *Determination of Electronic Energy Levels in Type-II CdTe-Core/CdSe-Shell and CdSe-Core/CdTe-Shell Nanocrystals by Cyclic Voltammetry and Optical Spectroscopy.* J. Phys. Chem. C, 2013. **117**(32): p. 16698-16708.

149. Poppe, J., et al. *A versatile approach for coating oxidic surfaces with a range of nanoparticulate materials.* J. Mat. Chem. C, 2013. **1**(7): p. 1515-1524.

150. Carey, F.A.; Sundberg, R.J. *Organische Chemie - ein weiterführendes Lehrbuch,* Wiley VCH, 1995, 978-3-527-29217-2.

151. Lokesh, K.S.; Adriaens; A. *Synthesis and characterization of tetra-substituted palladium phthalocyanine complexes.* Dyes and Pigment., 2013. **96**(1): p. 269-277.

152. Murray, C., et al. *Infra-red and Raman spectroscopy of free-base and zinc phthalocyanines isolated in matrices.* Phys. Chem. Chem. Phys., 2010. **12**(35): p. 10406-10422.

153. Sivanesan, A.; John, S.A. *Amino group position dependent orientation of self-assembled monomolecular films of tetraaminophthalocyanatocobalt(II) on Au surfaces.* Langmuir, 2008. **24**(5): p. 2186-2190.

154. Wang, G.X., et al. *Synthesis and characterization of one-dimensional CdSe nanostructures.* Appl. Phys. Lett., 2006. **88**(19).

155. Yukselici, M.H., et al. *A detailed examination of the growth of CdSe thin films through structural and optical characterization.* Mater. Res. Bull., 2013. **48**(7): p. 2442-2449.

156. Poppe, J. *Spectroelectrochemical Investigations of Semiconductor Nanoparticles.* Dissertation, University of Dresden, 2015.

157. Norris, D.J., et al. *Measurement of the Size-Dependent Hole Spectrum in Cdse Quantum Dots.* Phys. Rev. Lett., 1994. **72**(16): p. 2612-2615.

158. Woggon, U., et al. *Optical transitions in CdSe quantum dots: From discrete levels to broad gain spectra.* J. Lumin., 1996. **70**: p. 269-280.

159. Park, S.H., et al. *Nonlinear Optical-Properties of Quantum-Confined Cdse Microcrystallites.* J. Opt. Soc. Am. B., 1990. **7**(10): p. 2097-2105.

160. Miller, D.A.B., et al. *Band-Edge Electroabsorption in Quantum Well Structures - the Quantum-Confined Stark-Effect.* Phys. Rev. Lett., 1984. **53**(22): p. 2173-2176.

161. Spoor, F.C.M., et al. *Hole Cooling Is Much Faster than Electron Cooling in PbSe Quantum Dots.* ACS Nano, 2016. **10**(1): p. 695-703.

162. Querner, C., et al. *Size and ligand effects on the electrochemical and spectroelectrochemical responses of CdSe nanocrystals.* Phys. Chem. Chem. Phys., 2005. **7**(17): p. 3204-3209.

163. Kolle, P., et al. *Deactivation pathways of thiophene and oligothiophenes: internal conversion versus intersystem crossing.* Phys. Chem. Chem. Phys., 2016. **18**(11): p. 7903-7915.

164. Hesse, M., et al. *Spektroskopische Methoden in der organischen Chemie",* Georg Thieme Verlag, 2011, ISBN 978-3-13-576109-1.

165. de Boer, B., et al. *Synthesis and characterization of conjugated mono- and dithiol oligomers and characterization of their self-assembled monolayers.* Langmuir, 2003. **19**(10): p. 4272-4284.

166. Bisri, S.Z., et al. *Determination of the Electronic Energy Levels of Colloidal Nanocrystals using Field-Effect Transistors and Ab-Initio Calculations.* Adv. Mater., 2014. **26**(32): p. 5639-+.